ANALYSIS OF THE PRECISE RANGE AND RANGE-RATE EQUIPMENT (PRARE) AND APPLICATION TO PRECISE ORBIT DETERMINATION

by

John J. Bordi

Center for Space Research

The University of Texas at Austin

May 1999

CSR-99-01

This research was supported by

National Aeronautics and Space Administration
Grant NAGW-2132/NAG5-6346

Principal Investigator:
Byron D. Tapley

ABSTRACT: The satellite tracking data provided by the Precise Range And Range-rate Equipment (PRARE) is analyzed and then applied to precise orbit determination. The tropospheric corrections provided with the data are improved and the data is edited using the Guier plane technique. Justification for the estimation of the required kinematic parameters is provided, along with the optimal frequency that the parameters should be estimated. ERS-2 orbits are computed with different combinations of tracking data to show the impact of the PRARE data and its effectiveness both as a stand alone tracking system and as a supplement to the laser tracking system. It is shown that the PRARE data improves the accuracy of the calculated orbits through the analysis of tracking residuals, orbit endpoint comparisons, and altimeter crossover analysis. The tracking data is also evaluated by analyzing the station solutions. The accuracy of the station solutions are determined by examining repeatability, survey ties, and external solutions. The station installed on an ice sheet in Antarctica is used to assess the ability of PRARE to track a moving target. Additionally, the PRARE data is used to tune the JGM-3 and TEG-3 gravity field models to improve the performance of these models for satellites in similar orbits to ERS-2. The tuned gravity fields are evaluated by comparing the accuracies of the computed orbits and the sea surface topographies generated from the satellite altimetry. It is shown that tuning the gravity models improves the accuracy of the orbits and that both tuned models perform similarly for ERS orbit determination.

Table of Contents

Chapter 1

Chapter 2

Chapter 3

Chapter 4

Chapter 5

Chapter 6

Appendix A

Appendix B

List of Figures

List of Tables

Chapter 1

Introduction

Orbit determination is the process of using imperfect observations of a satellite's position or velocity, where its motion is described by imperfect dynamic models, to find the best approximation of the satellite's position over time. Since the launch of the first satellites, the problem of orbit determination has been refined considerably with the advent of precise satellite tracking systems, better physical models, and the dramatic increase in computing power. The precise knowledge of the position of an altimeter satellite is particularly critical, since the usefulness of the altimeter height measurements can be limited more by the accuracy of the orbits than any other error source.

The requirement for a precise satellite ephemeris has led to numerous methods of making measurements of a satellite's position and velocity. Over the years these methods have developed into the satellite tracking systems that are in use today. The subject of this dissertation is the impact on orbit determination of the Precise Range And Range-rate Equipment (PRARE), a new satellite tracking system, fully operational for the first time on the second European Remote Sensing satellite (ERS-2).

1.1 THE EUROPEAN REMOTE SENSING SATELLITES

The first European Remote Sensing satellite (ERS-1) was launched in 1991. The satellite platform, illustrated in Figure 1.1, is based on the design used

for the French Spot Satellites. The satellite structure is large, measuring two meters by two meters by six meters. The solar array is 12 by 2.4 meters, while the SAR antenna measures ten meters in length and is aligned along the flight path direction. The main scientific instruments on board are [Francis et al., 1991]:

- The Active Microwave Instrument (AMI), which can operate as either Synthetic Aperture Radar (SAR) or as the Wind and Wave Scatterometer.
- The Radar Altimeter (RA), which measures the vertical height of the satellite above the oceans and ice, the significant wave height, and the sea surface wind speed.
- The Along-Track Scanning Radiometer (ATSR), which measures sea surface temperature and atmospheric water vapor content.

Of these instruments, the Radar Altimeter and SAR put the most stringent requirements on the knowledge of the satellite's position. The altimeter is capable of making vertical measurements from the satellite to the ocean surface with an accuracy of a few centimeters. To take full advantage of the information in the altimeter measurements, the radial position of the satellite needs to be known as accurately as possible. Current radial orbit accuracies for the TOPEX/Poseidon altimeter satellite are reported to be less than 2 cm RMS, with the stated goal of achieving 1 cm RMS orbits [Ries and Tapley, 1999]. For SAR applications, accurate knowledge of the three-dimensional position of the satellite is required to make full use of the information in the measurements. Although, these

requirements are difficult to meet, it shows the need to provide the most accurate orbits possible.

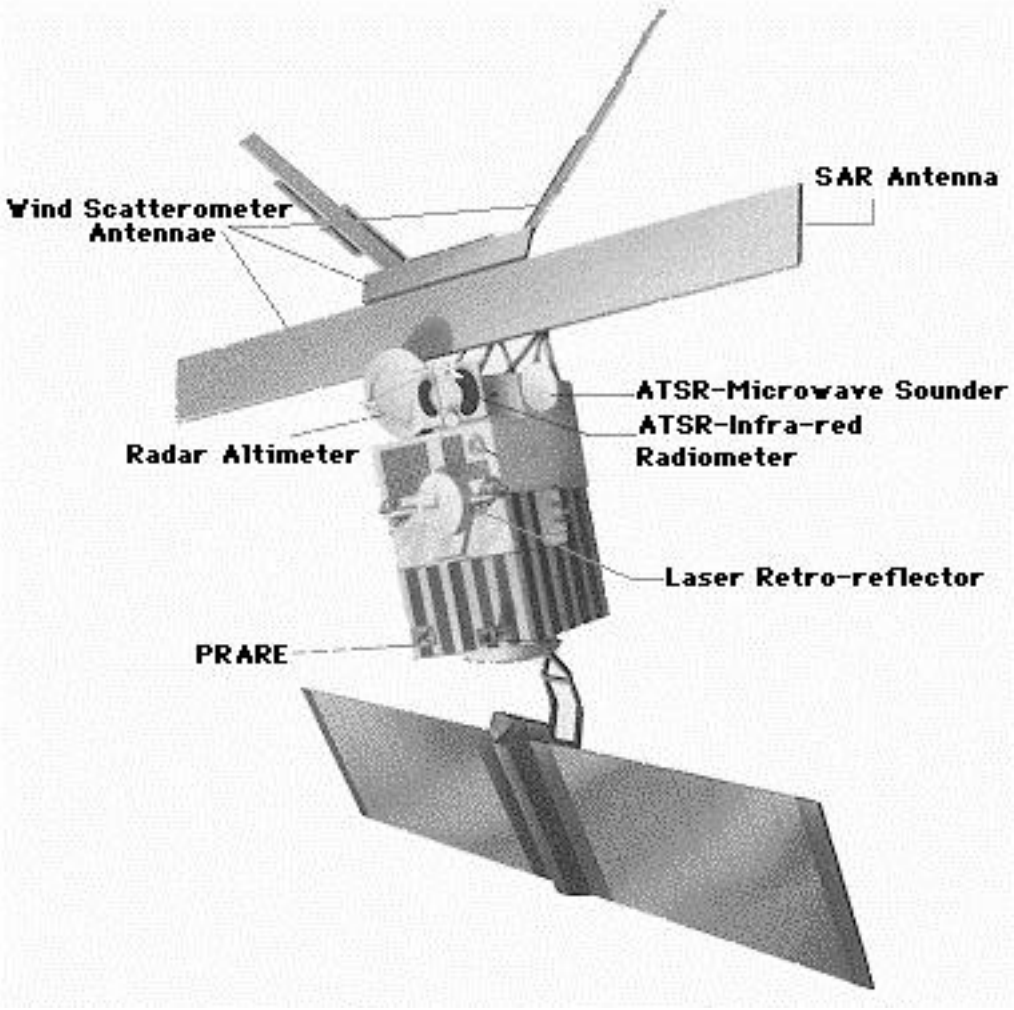

Figure 1.1: An Illustration of the ERS satellites

ERS-1 was launched on May 3, 1991. It was equipped with PRARE and a laser retro-reflector to provide satellite tracking, but the onboard PRARE system

failed shortly after launch. This meant that the only dedicated tracking available for ERS-1 was Satellite Laser Ranging (SLR). Since the amount of SLR tracking available was sparse, especially early in the mission, the altimeter data was used as a measurement type in the precise orbit determination (POD) process. Using altimetry as a measurement in the POD process is usually avoided, since it can lead to the aliasing of oceanic signals into the orbits. Not only can this degrade the orbit accuracy, but it may also prevent those very signals from being detected when the altimetry products are analyzed later.

ERS-2, which was launched on April 21, 1995, is very similar to ERS-1 [Francis et al., 1995]. The major difference is the addition of the Global Ozone Monitoring Experiment (GOME) [Hahne, et al., 1995], which is designed to measure the chemical composition of the atmosphere. Along with several other payload enhancements, ERS-2 carries a PRARE module that has several redesigned parts to make the unit more radiation resistant, since it was determined that the cause of the failure on ERS-1 was due to the high radiation environment [Schafer and Schumann, 1995]. Additionally, a second PRARE unit was installed on ERS-2, to serve as a backup.

ERS-1 and ERS-2 are in the same orbits, with the phasing between the satellites being such that ERS-2 passes over the ERS-1 ground track one day later. The satellites are in Sun-synchronous orbits at an altitude of approximately 780 km, with the descending node crossing the equator at 10:30 am local time. Being a Sun-synchronous satellite allows the solar panel to rotate about only one axis to maintain it's orientation towards the sun. Additionally, the constant illumination provided by a Sun-synchronous orbit, on descending passes, is advantageous for

some of the instruments onboard. The high inclination of 98.5 degrees gives the satellites coverage of almost the entire planet.

The ground track of the current orbit configuration has a 35 day repeat, meaning that every 35 days the satellite passes over nearly the same path on the Earth's surface. It takes 501 revolutions about the Earth to complete the 35 day repeat cycle. During each orbit, the satellite is in the sunlight for 66 minutes out of the approximately 100 minutes required for each revolution. The satellite's thrusters are used to maintain the constant ground track within certain bounds. The requirements are that the satellite ground track stay within ±1 km in the cross-track direction and the maximum latitude is kept within ±1 km of 81.5 degrees [McKay and Bosma, 1995]. Maintaining the cross-track within the prescribed limits requires orbit maintenance maneuvers, or burns, every two to four weeks, which overcome the orbit degradation caused by atmospheric drag. In general, as the solar flux increases the number of burns also increases. Early in the ERS-1 mission, during the last solar-maximum, burns were sometimes required every week. Keeping the maximum latitude of the ground track within ±1 km usually requires an out-of-plane maneuver twice per year.

1.2 RESEARCH OBJECTIVES

Current altimetric satellites use several different satellite tracking systems, including PRARE, SLR, GPS (Global Positioning System), and DORIS (Doppler Orbitography and Radio positioning Integrated by Satellite). The TOPEX/Poseidon satellite is tracked by SLR, GPS, and DORIS, and it is the

benchmark from which all other altimetric missions are compared. TOPEX is in a higher orbit than the ERS satellites, at an altitude of about 1330 km. This higher altitude, in combination with the copious amount of precise tracking, allows the orbits to be determined at the two centimeter level [Tapley et al., 1996]. For ERS-1, the orbits are routinely produced with an estimated radial accuracy of 5 cm [Ries et al., 1996; Scharoo and Visser, 1997]. For ERS-2, the addition of the PRARE data has enabled similar radial orbit accuracy to be achieved without the use of altimetry [Anderson et al., 1998; Bordi et al., 1997; Massmann et al., 1997; Visser et al., 1997]. Although the TOPEX level of accuracy will not be achieved for ERS-2 with the additional PRARE tracking, improving the ERS-2 accuracy to the sub-five centimeter level is plausible.

The primary objectives of this dissertation are to evaluate the performance of the PRARE tracking system and to use the PRARE data to maximize the ERS-2 orbit accuracy. The goal is to show the full potential of the PRARE system by optimizing the procedures and models used in processing the data. The quality of the data is examined on a station by station basis, to understand the characteristics of the data type and how to best employ it to capitalize on its strengths and overcome its weaknesses. The value of the PRARE data is assessed in terms of both orbit determination and station positioning. ERS-2, with it's two dedicated types of tracking data along with the altimeter, provides several gauges from which the orbit performance can be judged. Additionally, the possibility of improving current gravity field models with the addition of PRARE data is explored. The impact of these tuning efforts is examined for ERS-2 and satellites with different orbit characteristics.

Chapter 2

PRARE Measurements and Editing

As the name suggests, the PRARE system provides two types of measurements, range and Doppler. The measurements are made relative to the PRARE tracking stations which are located strategically around the globe in an attempt to provide geographically balanced coverage. The network is shown in Figure 2.1, along with the visibility regions for the ERS-2 satellite. This chapter explains how the measurements are made and describes the corrections that are applied. During the data preprocessing, some of the corrections provided with the PRARE data are improved. The last part of the chapter includes a discussion on the data editing techniques used for both the range and Doppler measurements. This will provide more insight into the characteristics of the PRARE data on a pass by pass basis, as well as the performance of individual tracking stations and the system as a whole.

2.1 THE PRARE MEASUREMENTS

The PRARE space segment, onboard ERS-2, transmits two microwave signals towards the ground. One signal is in the X-band (8.489 GHz), while the other is in the S-band (2.048 GHz). Both signals are modulated with the same Pseudo-random Noise (PN) codes; these signals have clock rates of 1 and 10 MHz for the S-band and X-band, respectively. Upon receipt, the ground station demodulates the two signals and correlates the two reconstructed PN-codes to

determine the time delay of the S-band versus the X-band. This time delay is a measure, to the first order, of the one-way ionosphere delay. This topic will be discussed further in Section 2.2.3.

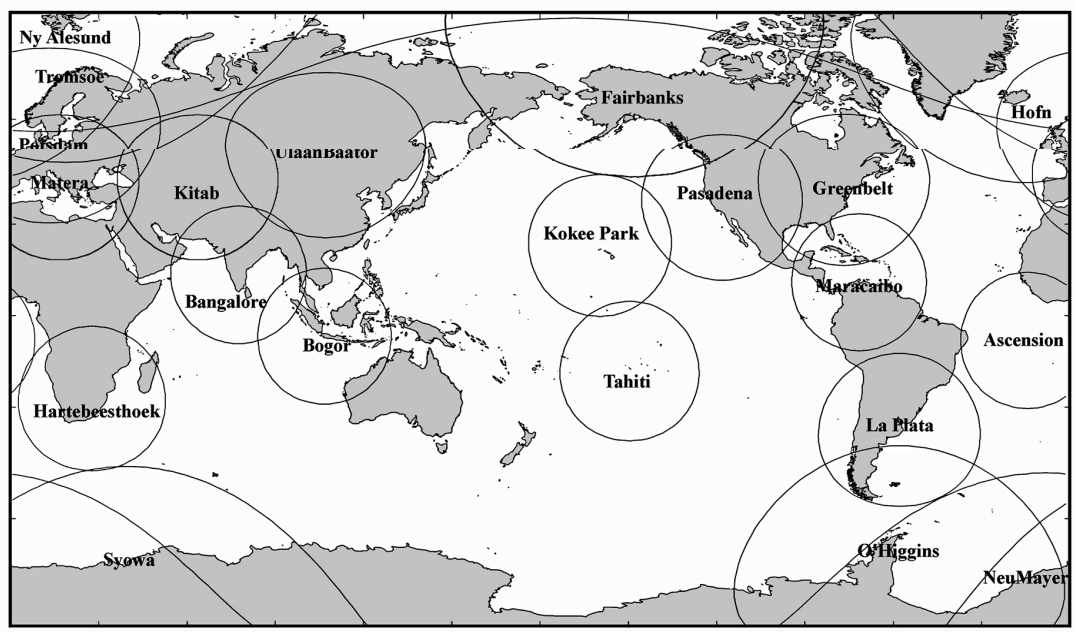

Figure 2.1: PRARE ground station network (with 5 degree elevation visibility masks for ERS-2)

In addition to the PN-codes, the carrier signals are modulated with a navigation message. This low-rate data includes time information which is used to synchronize the tracking station's clock and predicted ephemeris information which is used by the station to acquire and track the satellite during future passes. The pointing accuracy of the ground stations is 0.5 degrees, which means the predicted ephemeris must be accurate to roughly 0.5 km. This low-rate data also

includes measurement information that the space segment has processed from that particular station.

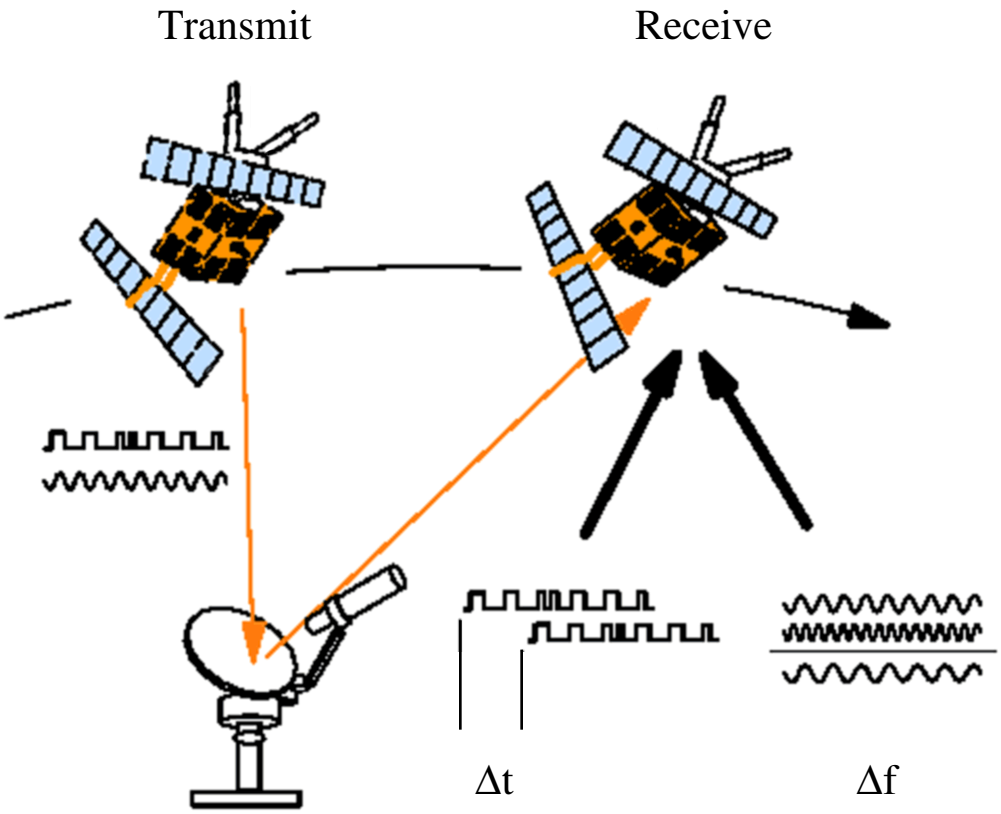

Figure 2.2: Illustration of the PRARE system on ERS-2

The X-band carrier is then coherently transposed, or multiplied by a constant factor (749/880), at the ground station to a frequency of 7.225 GHz. After this, the reconstructed PN-code is modulated onto the carrier signal and transmitted back up to the satellite. The reconstructed PN-code is also modulated with low-rate data. This data includes several measurements that are made at the

ground station. This information is used during ground processing to determine the appropriate corrections to the observations for that particular pass. For more details on the PRARE hardware and it's design specifications see the PRARE training course notes [Nortel DASA, 1995].

2.1.1 The PRARE range measurement

The PRARE space segment demodulates the PN-code from the carrier frequency upon receipt from the ground station. The reconstructed PN-code is correlated with the on-board PN-code, so that the length of time required for the signal to travel from the satellite to the ground station and back to the satellite is determined (see Figure 2.2). The two-way signal travel time is converted to range using:

$$Range = \frac{1}{2} \cdot c \cdot (\Delta t + \Delta t_{corr}) - \Delta\rho_{trop} - \Delta\rho_{iono} + \varepsilon, \tag{2.1}$$

where c is the speed of light, Δt is the measured time from transmission to reception of signal, and ε is the error in the observation. The $\Delta\rho$ terms are the range corrections due to the troposphere and ionosphere delays; these values are discussed in Section 2.2. The Δt_{corr} term in Equation 2.1 represents the rest of the corrections applied to the range measurements. This includes the internal delay of the PRARE stations (discussed in Section 2.2), the onboard PRARE antenna phase center correction, the ground station mechanical correction, and the external calibration correction. A total of 91 range measurements are made per second;

these 91 measurements are compressed into once per second measurements by the space segment. The once per second raw range measurements are compressed further into 15 second normal points, before being made available by GeoForschungs Zentrum, Potsdam (GFZ). Appendix A.1 shows how the PRARE range measurements are converted into CSR format during preprocessing.

The Range in Equation 2.1 is not an instantaneous range, rather it is an average of the up-link and down-link ranges as given by Equation 2.2. In this equation, t_1 represents the time the signal is transmitted, t_2 is the time the signal is received by the ground station, and t_3 is the time that the signal returns to the satellite. Equation 2.2 represents the computed range measurement, which is used to model the range measurement as given in Equation 2.1. The received time (t_3) is supplied with each of the observations, the other times are solved for by computing a light-time solution. First, the ground station received time (t_2) is estimated by using the computed instantaneous range to solve for the up-link time (t_3-t_2). The range is then recomputed using the estimate for the ground station received time (t_2), which is then used to make a new estimate for the up-link time. This iterative procedure is continued until convergence. The final value for the station received time (t_2) is similarly used to iteratively compute the down-link range and the satellite transmit time (t_1).

$$Range = \frac{1}{2} \cdot \left| \left[R_s(t_3) - R_g(t_2) \right] + \left[R_s(t_1) - R_g(t_2) \right] \right|, \tag{2.2}$$

where:

$R_s(t) =$ *position vector of satellite at time t*

$R_g(t) =$ *position vector of ground station at time t.*

2.1.2 The PRARE range-rate measurement

The range-rate measurement is based upon the Doppler frequency shift in the carrier frequency during both the down-link and the up-link [Wilmes et al., 1987]. The frequency of the carrier when the signal is received at the ground station is a function of the relative velocity of the satellite with respect to the ground station as given by:

$$f_{r_g} = f_{t_s} - \frac{\dot{\rho}_d}{\lambda} = f_{t_s}\left(1 - \frac{\dot{\rho}_d}{c}\right), \tag{2.3}$$

where:

f_{r_g} = *The frequency of the signal recieved by the ground station*

f_{t_s} = *The frequency of the signal transmitted by the satellite*

$\dot{\rho}$ = *The range - rate of the satellite with respect to the ground station*

λ = *The wavelength of the carrier signal*

c = *The speed of light*.

Similarly, the frequency of the carrier when the satellite receives the signal can be expressed as:

$$f_{r_s} = f_{t_g}\left(1 - \frac{\dot{\rho}_u}{c}\right) = K \cdot f_{t_s}\left(1 - \frac{\dot{\rho}_d}{c}\right) \cdot \left(1 - \frac{\dot{\rho}_u}{c}\right), \tag{2.4}$$

where:

f_{r_s} = *The frequency of the signal recieved by the satellite*

f_{t_g} = *The frequency of the signal transmitted by the ground station*

K = *The constant factor of frequency transposure* $(749/880)$.

The Doppler frequency shift is measured by counting the number of cycles in the difference between the received carrier frequency and the transposed onboard carrier frequency, $K \cdot f_{t_s}$, over an integration interval. This cycle count is related to the difference between the two frequencies by the simple relation:

$$\int_{t_1}^{t_2} \left(f_{ref} - f_{r_s} \right) dt = N + N_{corr} + \varepsilon, \tag{2.5}$$

where:

$$f_{ref} = K \cdot f_{t_s} = K \cdot \left(f_{t_{s_o}} + f_o \right)$$

$f_{t_{s_o}}$ = *Nominal transmitted frequency (8.489 GHz)*

f_o = *Constant frequency offset*

N = *The Doppler cycle count.*

For the PRARE measurements, the standard Doppler count interval (t_2 - t_1), is 30 seconds, although a measurement is taken every second. Converting the second integral from received time to transmitted time and recognizing that the total number of cycles transmitted equals the number of cycles received, the left side of Equation 2.5 can be rewritten as:

$$\begin{aligned} \int_{t_1}^{t_2} f_{ref} dt - \int_{t_1}^{t_2} f_{r_s} dt = \\ \int_{t_1}^{t_2} f_{ref} dt - \int_{t_1 - \delta t_1}^{t_2 - \delta t_2} K \cdot f_{t_s} dt = \\ \int_{t_1}^{t_2} f_{ref} dt - \int_{t_1 - \delta t_1}^{t_2 - \delta t_2} f_{ref} dt = N + N_{corr} + \varepsilon. \end{aligned} \tag{2.6}$$

Where δt_1 and δt_2 represent the two-way travel times, at both the start and end of the integration interval. Assuming that the transmitted frequency is constant over the integration interval, Equation 2.6 can be integrated as follows:

$$f_{ref}\left(\delta t_2 - \delta t_1\right) = N + N_{corr} + \varepsilon. \tag{2.7}$$

This can also be written as:

$$f_{ref}\left(\frac{2\rho_2}{c} - \frac{2\rho_1}{c}\right) = N + N_{corr} + \varepsilon, \tag{2.8}$$

where the ρ terms are the ranges at the start and end of the integration interval, as defined in Equation 2.2. This is then converted into an equation for the "average range-rate" over the Doppler count interval ($\Delta t = t_2 - t_1$), as given by:

$$\begin{aligned} \frac{\rho_2 - \rho_1}{\Delta t} &= \frac{1}{2}\left(\frac{N + N_{corr}}{\Delta t}\right)\frac{c}{f_{ref}} + \varepsilon \\ &= \frac{1}{2}\left(\frac{N}{\Delta t}\right)\frac{c}{f_{ref}} - \frac{\Delta\rho_{trop}}{\Delta t} + \frac{\Delta\rho_{iono}}{\Delta t} + \frac{\Delta\rho_{corr}}{\Delta t} + \varepsilon \end{aligned} \tag{2.9}$$

The $\frac{\Delta\rho}{\Delta t}$ terms in Equation 2.9 are the range-rate corrections for troposphere, ionosphere, and the remaining corrections respectively. Similar to the range measurements, the once per second Doppler measurements are compressed into 15 second normal points before the PRARE data is distributed. The left side of Equation 2.9 is the computed Doppler measurement, which is calculated during

the orbit determination process. Appendix A.2 shows how the PRARE range-rate measurements are converted into CSR format during preprocessing.

2.2 THE MEASUREMENT CORRECTIONS

Several corrections are made to both the range and Doppler measurements. These corrections are: the internal delay of the ground station, the two-way troposphere and ionosphere delays, the phase center offset for both the ground station and satellite antennas, the center of mass offset for the satellite antenna, and the 91 value correction. The methods used to determine some of these values are discussed in the following sections.

2.2.1 The Ground Station Internal Delay

Before acquisition of the satellite's signal for each pass, the ground station performs an initial internal delay measurement using a built in test transponder. The internal delay is the time required for the station to process the incoming signal and retransmit it. An average value for this time is about 400 nanoseconds, which can represent about 120 meters in range. During the pass, the ground station makes corrections to this initial internal delay measurement every few seconds. The corrections are made by monitoring the voltage and noise levels in the receivers, the Doppler frequency, and the temperatures of different parts of the station. These values are then plugged into correction tables which are generated during station calibration, before delivery of the station, to determine the corresponding internal delay correction. These calculated internal delays are then

used to correct the range measurements and are included in the Δt_{corr} term of Equation 2.1.

The errors in the calculated internal delay can be significant and variable over time. The result of these errors is a bias in the range measurements, which will vary from station to station over time, and usually have values between ±30 cm. This bias must be accounted for in the orbit determination procedure. Since the bias is unknown a priori, it must be estimated periodically. In order to determine the best way to handle these biases, their stability needs to be examined. If the biases are relatively stable, they can be estimated infrequently. On the other hand, if the biases show little consistency, it may be required to estimate them for every pass of the satellite. It is desirable to estimate the biases only as frequently as required since the strength of the range measurements will diminish as the number of estimated parameters increases.

2.2.2 The Troposphere Delay

The delay experienced by radio waves propagating through the electrically neutral atmosphere is referred to as the troposphere delay. The troposphere delay is generally broken into two components, called the hydrostatic (or dry) and the wet delays. Both of these components can be represented as a product of the zenith delay and a mapping function, which projects the zenith delay to the correct elevation [Mendes and Langley, 1994]. The delay varies significantly depending on the station height above sea level, the station to satellite elevation angle, and the atmospheric conditions along the signal path. In order to determine the value of the delay, empirical formulas are used which relate these variables to

the overall delay. To this end, the ground stations monitor the local temperature, atmospheric pressure, and humidity continuously. These meteorological values are then encoded onto the carrier signal which is transmitted back to the satellite.

The PRARE Troposphere Zenith Delay

The model used to determine the zenith delay due to the troposphere for the PRARE data is a modified version of the Saastamoinen model [Saastamoinen, 1972]. The dry, or hydrostatic, delay in this model is given by:

$$\Delta\rho_{z_{dry}}(m) = 0.002277\frac{P_o}{f(\varphi, H_s)}$$
$$f(\varphi, H_s) = 1 - 0.00266\cos 2\varphi - 0.00000028H_s, \tag{2.10}$$

where: φ is the geodetic latitude of the station, H_s is the height of the station above the reference ellipsoid (in meters), and P_o is the surface pressure at the station (in millibars). The wet part of the troposphere delay is given as:

$$\Delta\rho_{z_{wet}}(m) = 0.002277e_o\left(\frac{1255}{T_o} + 0.053\right), \tag{2.11}$$

where: e_o is the partial pressure of the water vapor at the station and T_o is the surface temperature in Kelvin. The errors in the wet part of the calculated zenith delay are highly variable, due to spatial and temporal changes in the amount of water vapor in the atmosphere which are not accounted for when just the surface meteorological measurements are used to compute the delay.

The Davis troposphere mapping function

The calculated zenith delay is mapped to the appropriate elevation by using a troposphere mapping function, of which there are several available [Estefan and Stovers, 1994]. These mapping functions account for the signal having to travel through more of the troposphere as the elevation of the observation decreases, as well as the bending of the signal path which increases as the elevation angle decreases. The mapping function provided with the PRARE data is the Davis model, known as the CfA-2.2 mapping function [Davis et al., 1985]. In general, most mapping functions supply mapping factors for both the wet and dry portions of the zenith troposphere delay so the total troposphere delay is written as:

$$\Delta\rho_{trop}(E) = \Delta\rho_{z_{dry}} M_{dry}(E) + \Delta\rho_{z_{wet}} M_{wet}(E) \tag{2.12}$$

In Equation 2.12, M_{dry} and M_{wet} are the mapping factors, and E is the unrefracted elevation angle of the observation. The $\Delta\rho$ terms are the zenith delays as given in Equations 2.10 and 2.11. For the Davis mapping function, M_{dry} and M_{wet} are the same, since the mapping function was developed specifically for mapping the dry component of the delay. The model utilizes the same surface meteorological measurements required for the zenith delay (local pressure, temperature, and humidity). The Davis mapping factor is expressed as:

$$M_{CfA-2.2}(E) = \frac{1}{\sin E + \dfrac{a}{\tan E + \dfrac{b}{\sin E + c}}} \tag{2.13}$$

where:

$$a = 0.001185\left[\begin{array}{c} 1 + 0.6071\times10^{-4}\left(P_o - 1000\right) + 0.003072\left(T_o - 293.15\right) \\ - 0.1471\times10^{-3} e_o \end{array}\right]$$

$$b = 0.001144\left[\begin{array}{c} 1 + 0.1164\times10^{-4}\left(P_o - 1000\right) + 0.003109\left(T_o - 293.15\right) \\ + 0.0001144 e_o \end{array}\right]$$

$$c = -0.009$$

The continued fraction in Equation 2.13 is fairly common in most of the troposphere mapping functions [Estefan and Stovers, 1994].

The Niell troposphere mapping function

In Chapters 3 and 4, an alternative mapping function will be tested in an effort to improve the accuracy of the troposphere delay corrections. The Niell function [Niell, 1996] will be used, since both Estefan and Stovers [1994] and Stovers and Lanyi [1994] have shown that the Niell mapping function (NMF) is one of the most accurate of the current models available. The Niell function differs significantly from the Davis function in that it has separate mapping factors for the wet and dry components of the troposphere delay. Also, it does not rely on local atmospheric conditions as inputs, rather it uses the location of the station and the day of year. A summary of the mapping factors (M_{dry} and M_{wet}) for the Niell troposphere mapping function is provided in Appendix B.

Analysis of the Meteorological Data

Equations 2.10, 2.11, and 2.13 all indicate that determination of the troposphere delay for radiometric measurements is dependent on the atmospheric measurements taken at each of the tracking stations. Unfortunately, these meteorological measurements are not always available. In fact, during 1996 and 1997 the meteorological measurements were not provided about 40% of the time. When no measurements are made, the values supplied in the PRARE records in place of the meteorological measurements are gridded monthly means from the European Center for Medium-range Weather Forecasting (ECMWF) model. By comparing the monthly mean values to the full-rate ECMWF values, we can assess how well the monthly mean model is performing. At the same time, we can also compare the measured values with the full-rate ECMWF values. This will provide a comparison for evaluating the performance of the PRARE station's meteorological measurements. The pressure values in the full-rate ECMWF model have been found to be accurate to the 3 mbar level. See Chapter 3 of Kruizinga [1997] for a complete discussion on the validation of the ECMWF model.

All three meteorological measurements from the PRARE data records (both the measured values and the monthly mean model) are compared to the ECMWF model. Figures 2.3 through 2.6 show the pressure comparisons for four different ground stations. In each of these figures the top panels show the pressure values supplied on the PRARE data, where the red marks indicate measured values, and the blue marks indicate the monthly mean model. The second panel shows corresponding full-rate ECMWF pressures, and the bottom panels are the

differences between the two upper panels. In general, 1 mbar of pressure equates to about 2 mm of troposphere correction.

After analyzing these comparisons, it was decided that the monthly mean model was not providing an acceptable approximation of the actual atmospheric conditions at the station. Consequently, for the analysis described here, all of the modeled meteorological values are replaced with the full-rate ECMWF values. This includes not only the pressure, but also the temperature and humidity values as well.

Figure 2.3 shows how a nominal station should perform. This station, on Ascension Island, shows consistent pressure measurements for the two year duration. For the first part of 1996, there seems to be a slight bias of about 2 mbars between the measurements and the ECMWF pressure values. But overall, the agreement is within the expected accuracy of the ECMWF model. Figure 2.4 shows how large the variances between the monthly mean model and the full-rate model can be. This meteorological station at O'Higgins, Antarctica only provided data for a short period near the end of 1996, represented by the red marks in the top panel. The bottom panel shows that these few measurements agree quite well with the full-rate ECMWF model. However, the monthly mean model provided with the PRARE data differs significantly from the full-rate ECMWF model. The differences reach up to 50 mbars, which represents an error in the zenith troposphere delay of about 10 cm.

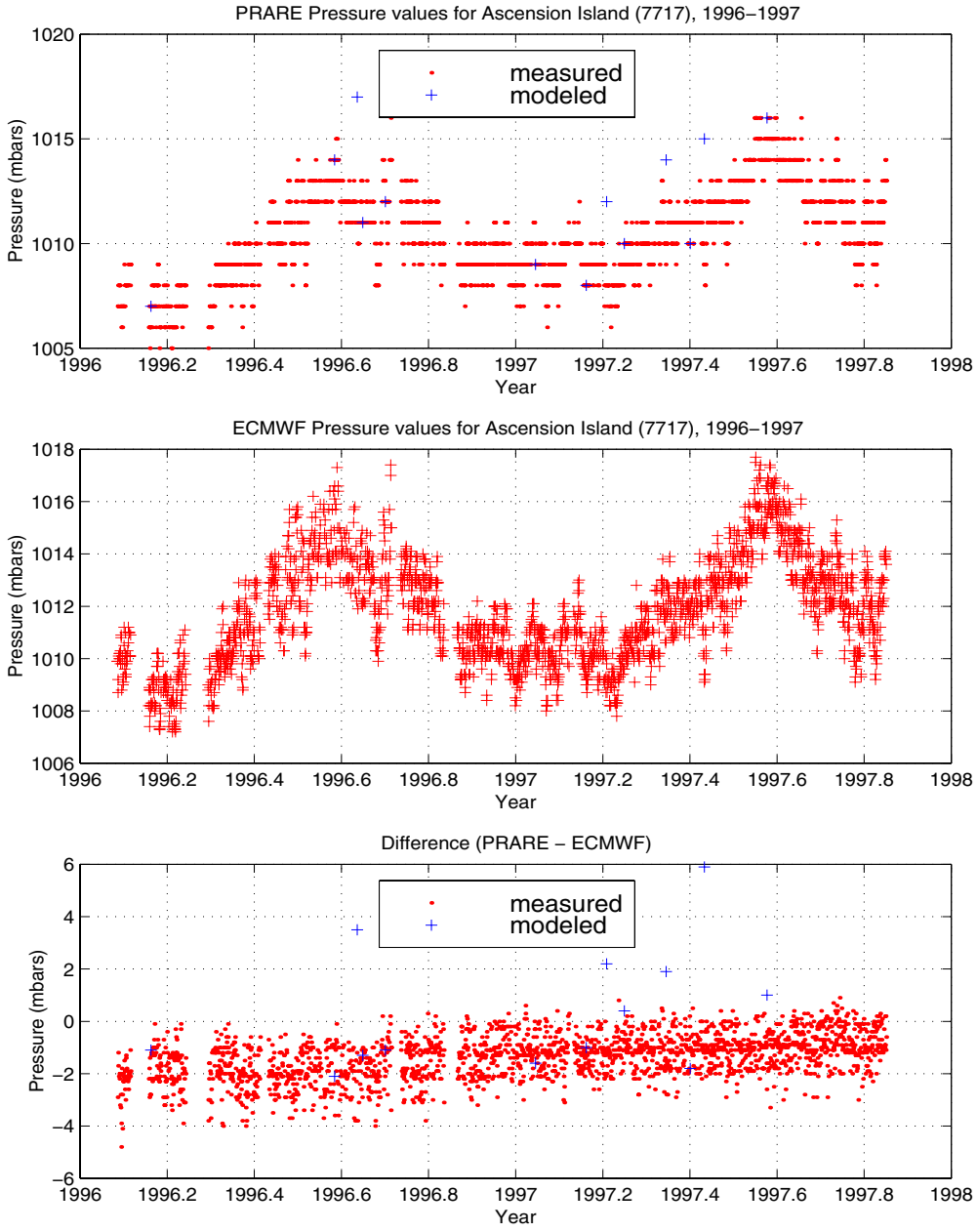

Figure 2.3: Ascension Island: comparison of pressure values from ECMWF and pressure stored on the PRARE data records

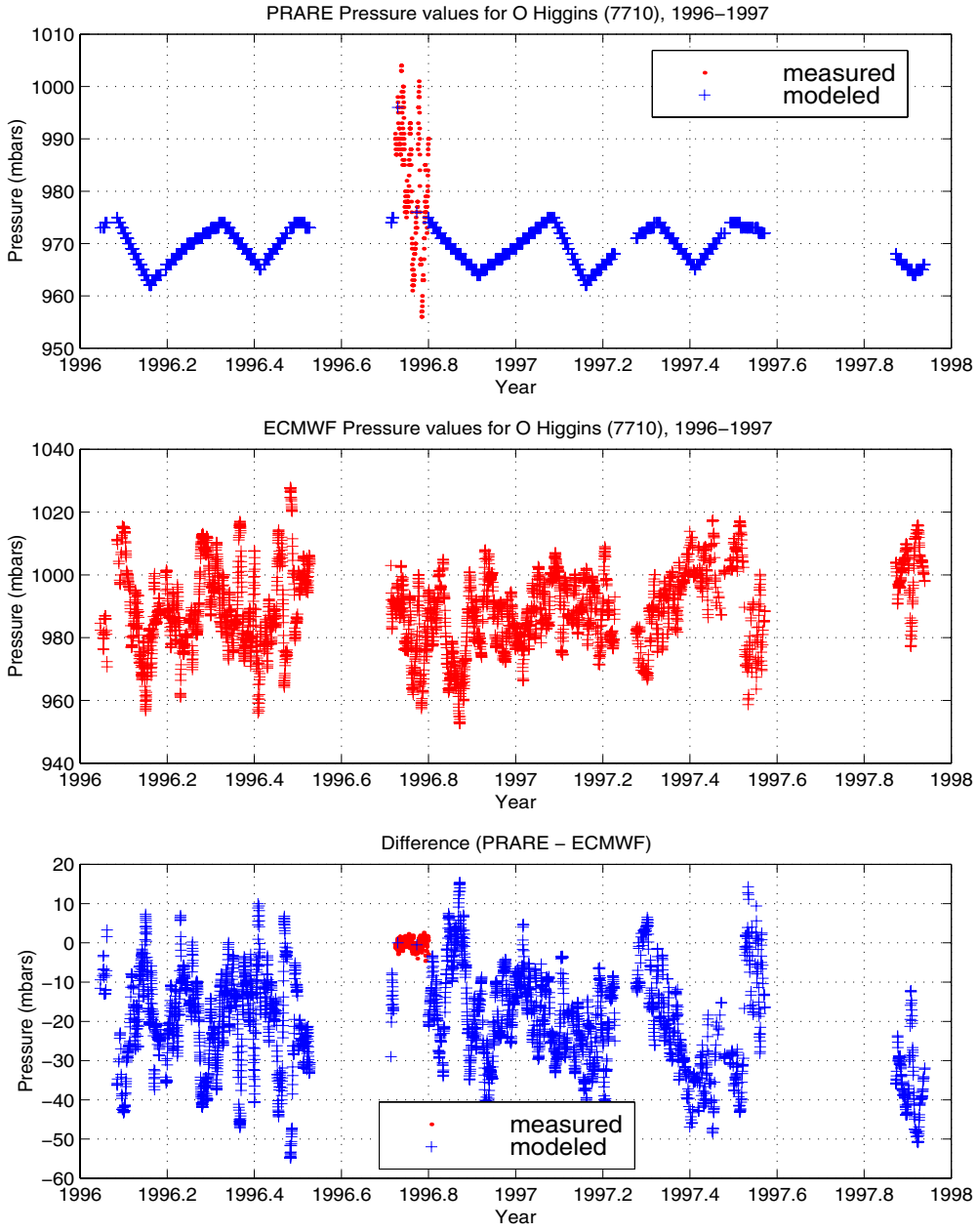

Figure 2.4: O'Higgins, Antarctica: comparison of pressure values from ECMWF and pressure stored on the PRARE data records

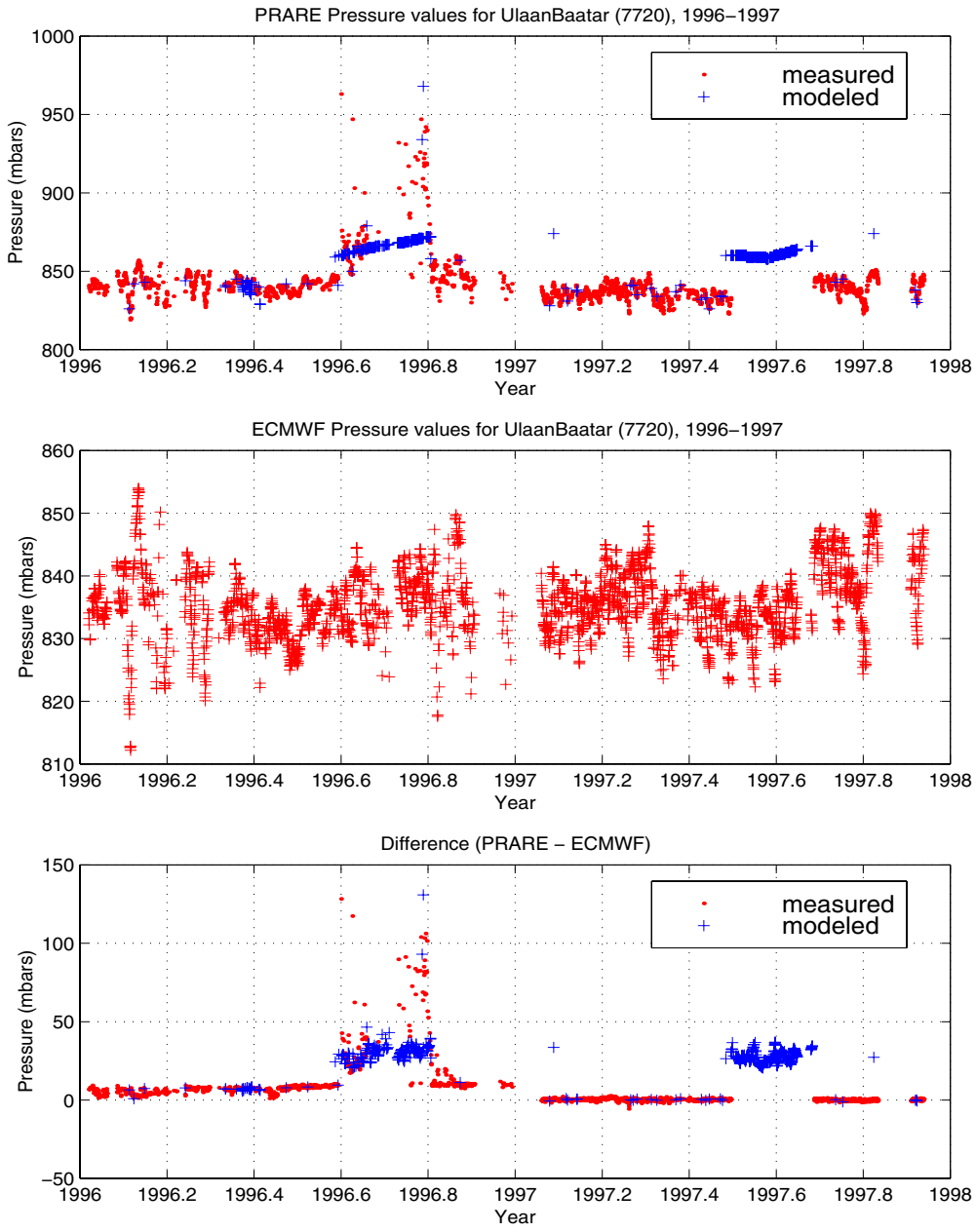

Figure 2.5: UlaanBataar, Mongolia: comparison of pressure values from ECMWF and pressure stored on the PRARE data records

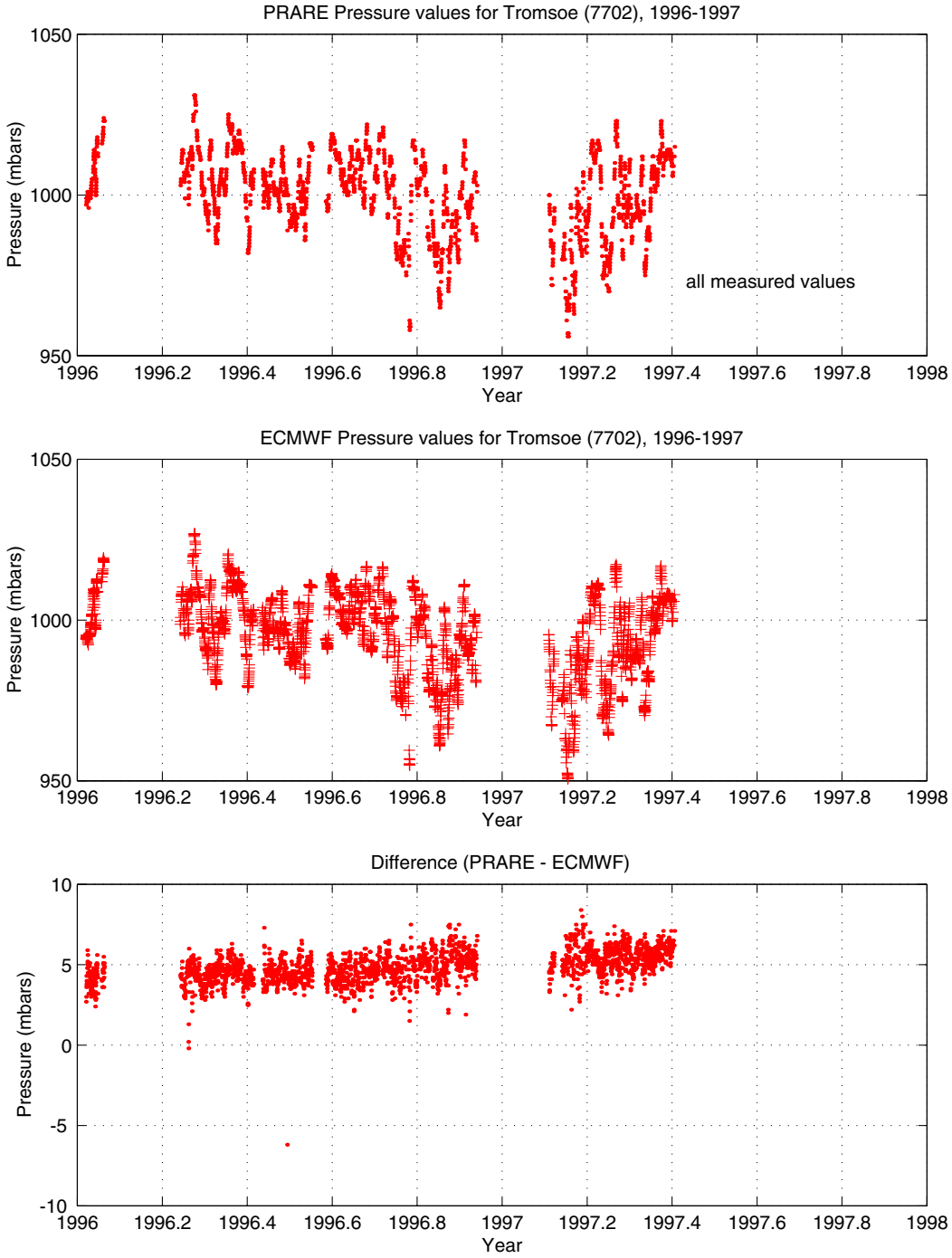

Figure 2.6: Tromsoe, Norway: comparison of pressure values from ECMWF and pressure stored on the PRARE data records

Large discrepancies are seen occasionally between the measured meteorological data and the full-rate ECMWF values. Each of these discrepancies is examined on a case by case basis, and when deemed appropriate the measurements are replaced with the full-rate ECMWF model, especially when there are indications that the PRARE meteorological station may not be operating correctly. For example, if a PRARE meteorological station appears to be fluctuating between operating properly and not providing data, the measurements are replaced with the full-rate ECMWF values when large differences are observed between the two. As an illustration of this, Figure 2.5 shows the pressure comparisons for the station in UlaanBataar, Mongolia. Between 1996.6 and 1996.8, the meteorological measurements are only provided sporadically. The measurements that are provided show large discrepancies with the ECMWF model, while outside this time frame the measurements compare favorably. During such periods, the pressure measurements are replaced with the values from the full-rate ECMWF model.

At times, consistent biases are seen between the measured pressures and the full-rate ECMWF values. Often, these biases are applied to the measured pressure values, since it is not known how well the PRARE meteorological stations are calibrated, or for that matter how stable the pressure sensors are. This is the situation at Tromsoe, Norway as depicted in the last of the pressure comparison plots (Figure 2.6). The bottom panel shows a consistent bias in the pressure measurements of 5 mbars, so the pressure measurements are corrected by this amount.

Improving the Zenith Wet Troposphere delay

One of the main weaknesses in the accuracy of the computed troposphere delay is in the zenith wet troposphere delay (Equation 2.11). One of the problems is that this equation relies entirely on the atmospheric conditions at the station, while the delay is actually dependent on the atmospheric conditions from the station elevation all the way up to the top of the troposphere. Once again, the full-rate ECMWF model is used to provide this additional information. The ECMWF model stores temperature and humidity at 15 different constant pressure levels. By integrating from the station position upward to the top of the troposphere, through the 15 different levels of pressure, a better estimate of the zenith wet troposphere delay can be made. The wet zenith delay calculated from the ECMWF model in this manner is estimated to have an accuracy of one to four cm [Kruizinga, 1997 and Stum, 1994]. This compares to the estimated accuracy of about 8 mm for the dry part of the zenith delay.

As part of the PRARE pre-processing for the data analyzed here, the zenith wet troposphere delay is calculated from the ECMWF model for each observation, and is then used in Equation 2.12 as the $\Delta\rho_{z_{wet}}$ term. It should be noted that both the zenith dry troposphere delay and the Davis troposphere mapping function still rely on the surface atmospheric values at the tracking station's position.

Evaluation of the Troposphere Improvements

The results of replacing and/or adjusting some of the meteorological measurements and computing the zenith wet troposphere delay with the ECMWF

model can be seen by examining the consistency of the troposphere scale factors. These scale factors are estimated for every pass of combined PRARE range and Doppler data. Table 2.1 compares the statistics of the scale factors for each station over a three cycle (105 day) test period in 1996. Not only are the new values more consistent, but they are also more closely centered around unity. This indicates that the changes made have improved the accuracy of the calculated troposphere delays.

Table 2.1: Troposphere scale factor statistics before and after replacing and adjusting the meteorological data and using the ECMWF model to calculate the zenith wet delay.

		Scale factor (Before)		Scale factor (After)	
Station	% Adjusted	Average	RMS	Average	RMS
Tromsoe	100	0.989	0.027	1.001	0.017
Matera	0	0.983	0.012	1.008	0.012
Tahiti	0	0.989	0.015	1.006	0.008
O'Higgins	52	0.985	0.009	1.000	0.008
Hartebeesthoek	100	0.989	0.012	1.004	0.009
La Plata	0	0.992	0.018	1.000	0.011
Maracaibo	100	1.000	0.014	1.001	0.013
Ascension	30	0.978	0.010	1.005	0.009
UlaanBataar	100	0.985	0.014	0.994	0.011
Greenbelt	100	1.002	0.020	1.009	0.017
Bangalore	100	1.007	0.018	1.007	0.012
NyAlesund	0	0.987	0.012	0.998	0.011
Shanghai	100	0.989	0.024	1.004	0.014
Oberpfaffenhofen	99	0.987	0.012	1.002	0.007
Neumayer	100	0.988	0.015	1.002	0.015

2.2.3 The Ionosphere delay

The ionosphere refraction of microwave radio signals is dependent on the frequency of the signal as well as the Total Electron Content (TEC) along the signal's path. Ignoring higher order terms, the one-way time delay caused by the ionosphere is given by [Wilmes and Reigber, 1987]:

$$\tau = \frac{1}{c} \cdot \frac{40.31}{f^2} \cdot TEC, \tag{2.14}$$

where f is the frequency of the transmitted signal. By measuring the time difference between the reception of the X-band and S-band signals sent from the spacecraft to the ground station ($\Delta\tau$), the TEC can be inferred. Subtracting Equation 2.14 for the X-band frequency from Equation 2.14 for the S-band frequency and solving for the TEC gives:

$$TEC = \frac{c \cdot \Delta\tau}{40.31}\left(\frac{f_x^2}{f_x^2 / f_s^2 - 1}\right). \tag{2.15}$$

If we plug the solution for the TEC back into Equation 2.14, we get the one-way down link time delay for the X-band frequency.

$$\tau_{xd} = \frac{\Delta\tau}{f_x^2 / f_s^2 - 1} \tag{2.16}$$

The uplink time delay can also be estimated, assuming that the TEC along the uplink signal path is the same as the downlink. Since the uplink frequency is multiplied by K, the constant factor of frequency transposure (Equation 2.4), the time delay for the uplink is given as:

$$\begin{aligned}\tau_{xu} &= \frac{1}{c}\cdot\frac{40.31}{\left(K\cdot f_x\right)^2}\cdot TEC \\ &= \frac{1}{K^2}\cdot\left(\frac{\Delta\tau}{f_x^2/f_s^2-1}\right)=1.38\cdot\left(\frac{\Delta\tau}{f_x^2/f_s^2-1}\right)\end{aligned} \tag{2.17}$$

In terms of range, the ionosphere correction can be written as the sum of Equations 2.16 and 2.17 as follows:

$$\begin{aligned}\Delta\rho_{iono} &= \frac{1}{2}\cdot c\left(\tau_{xd}+\tau_{xu}\right) \\ &= 1.19\cdot c\left(\frac{\Delta\tau_{xs}}{f_x^2/f_s^2-1}\right)\end{aligned} \tag{2.18}$$

For the Doppler correction, the difference of Equation 2.18, calculated at both the start and end of the integration interval, is divided by the integration interval.

The Differenced Range Versus Integrated Doppler Method

Another, more accurate way to determine the ionosphere delay has been developed, known as the Differenced Range Versus Integrated Doppler (DRVID) method [Flechtner et al., 1997]. This method takes advantage of the fact that the ionosphere delays for the range and Doppler measurements have opposite signs. This is because the propagation speed for the range signal is the group velocity,

while the Doppler signal propagation speed is the phase velocity. In other words; the ionosphere delay lengthens the range time measurement (Equation 2.1), and decreases the Doppler count (Equation 2.9).

The principle proposed is to subtract two adjacent once per second range measurements, with all other corrections applied. Then, the integrated range measurement is calculated from a Doppler measurement at the same time. Since all the other corrections have the same sign, when the differenced range and integrated range measurements are subtracted these delays cancel out. The remaining value is equal to the two way ionospheric Doppler measurement correction. To get the range correction the result is simply integrated over the one second time interval. There are problems associated with this procedure that result in biased values for the troposphere corrections [Flechtner, 1998].

2.3 DATA EDITING

The raw PRARE data which is downloaded from the GFZ ftp server has already been edited to some extent. Further editing of the data is required, since eliminating bad measurements strengthens the quality of the orbits. Additionally, those measurements which are very weak and contribute virtually nothing to the orbits are edited, thus reducing the computing time required to process the data.

2.3.1 The Guier Editing Technique

When editing the PRARE observations, the first step is to take the PRARE residuals (observation minus computed value of range or range-rate), and

eliminate systematic errors from each pass of data. Guier's Theorem [Wells, 1977] is used as the basis for removing the systematic errors from each pass of PRARE data. The plane which contains both the velocity vector of the satellite and the range vector from the tracking station to the satellite, at the time of the satellite's closest approach to the station, is defined as the Guier plane [Davis et al., 1997]. By adjusting the station coordinates in the Guier plane for every pass of satellite tracking data, the Guier theorem maintains that both the orbit and station position errors can be eliminated from the residuals. The station coordinates are adjusted every pass in the direction from the station to the satellite's closest approach and also in the direction of the satellites velocity at the satellite's closest approach. These directions are referred to as the slant range and tangential directions throughout the remainder of this section.

In addition to the Guier parameters, a range bias and a troposphere scale factor are estimated for every pass of PRARE data. The Navigation Solution editing software (NAVSOL) [Smith, 1988] was modified to process the PRARE range and Doppler measurements simultaneously for each pass. The observation equations in NAVSOL for both the range and Doppler measurements are:

$$\begin{aligned} y_{range} &= Residual_{range} - G_{range} \\ G_{range} &= \frac{\rho_{slant}}{\rho} \cdot \Delta slant + \frac{\rho_{tangent}}{\rho} \cdot \Delta tangent + Bias + \alpha \cdot \Delta\rho_{trop} + \varepsilon, \end{aligned} \tag{2.19}$$

and:

$$\begin{aligned} y_{Doppler} &= Residual_{Doppler} - G_{Doppler} \\ G_{Doppler} &= \frac{\left(G_{range}\right)_2 - \left(G_{range}\right)_1}{\Delta t} + \varepsilon. \end{aligned} \tag{2.20}$$

For each pass, the best estimate of the four parameters ($\Delta slant$, $\Delta tangent$, $Bias$, α) is made using a least squares solution. For a validation of the Guier editing technique see Smith [1988].

2.3.2 Edit Criteria

By processing the range and Doppler data together, the strength of the estimated parameters is increased. Using just the range data, the range bias and the slant range error can have very high correlations. The Doppler data does not contribute to the range bias, so it provides separation between the estimated range bias and the slant range error. Likewise, the troposphere scale factors are better determined when the two data types are used simultaneously [Enninghorst, 1997]. This is a reasonable approach for editing, since both data types will be used in the orbit determination process. Even though combining the data types reduces some of the correlations, some passes still exhibit very high correlations between the slant range errors, the range biases, and the troposphere scale factors. The amount of correlation depends on the pass geometry, the density of the observations within the pass, and the balance of the observations over the duration of the pass. In the modified NAVSOL, the range observations are assigned an a priori standard deviation of 10 cm, while the Doppler observations are assigned a value of 1 mm/sec.

The RMS of the residuals after the removal of the estimated parameters, i.e. the RMS of y in Equations 2.19 and 2.20, is called the Guier RMS. This number gives a good indication of the data noise, since it reflects the remaining residual after systematic errors are removed from each pass of tracking. Table 2.2

lists the editing criteria used in processing the PRARE data. The top of the table lists criteria for single observations, while the bottom portion of the table lists the criteria that apply to whole passes.

Table 2.2: PRARE editing criteria

Observations are edited when:
• The elevation angle is less than 5 degrees. • The raw residuals are greater than: 5 cm/s for Doppler measurements 5 m for range measurements • The residuals after application of Guier parameters are greater than 2.5 times the RMS of the entire pass, with minimum edit values of: 0.6 mm/s for Doppler measurements 6 cm for range measurements
Passes are edited when:
• Either one of the data types (range or Doppler) are not available. • The maximum elevation is less than 10 degrees. • The pass duration is less then 1 minute. • A gap of more than 7 minutes exists in the tracking data. • There are less than 10 total observations. • The pass is too unbalanced; less than 5% of the tracking data is before or after the maximum elevation of the pass. • More than 25% of the observations in any pass are edited for other reasons (an indication of anomalous behavior). • the Guier RMS of the pass is greater than: 1 mm/s for the Doppler data 10 cm for the range data • When the estimated pass parameters have values and/or associated standard deviations greater than: Slant range: estimate = ±130 cm, sigma = 100 cm Tangential: estimate = ±50 cm, sigma = 30 cm Range bias: estimate = ±150 cm, sigma = 140 cm Trop. sc. fact.: estimate = ±0.10, sigma = 0.08

The criteria outlined in Table 2.2 result in 14% of the data in 1996 and 16% of the 1997 data being edited. The minimum elevation, duration, and pass

balance requirements are chosen to eliminate those passes where separation of the estimated parameters is not adequate. The editing criteria involving the RMS of the residuals, before and after application of the Guier parameters, eliminates those passes or observations which have higher than normal noise levels. The editing criteria based on the size of the four estimated parameters eliminates passes that appear to have abnormally large biases. This data, if used, can not only hurt the orbits, but also degrades the station position solutions.

2.3.3 Editing Results

The results of the Guier method, outlined above, can be seen by examining the variation of the residuals during individual passes. Figures 2.7 through 2.10 show the residuals before, and after, the Guier parameters are estimated for typical passes of range and Doppler data from four different stations. The plots show that some systematic errors remain in the residuals even after the Guier parameters are removed. Remaining signals are particularly evident in the Doppler data from the Tahiti (Figure 2.7: bottom), Hartebeesthoek (Figure 2.8: bottom), and Ascension Island (Figure 2.9: bottom) passes, and in the range data from Ascension Island (Figure 2.9: top) and UlaanBataar (Figure 2.10: top) passes. These signals, however, have a higher frequency than what could be caused by orbit error or station position error. The signals must be due to the PRARE measurements themselves. Similar, high frequency signals are frequently observed in many of the passes. These signals are presumably the result of various instrument or propagation effects, including oscillator stability, electronics variations, and short period variations in the wet troposphere or ionosphere.

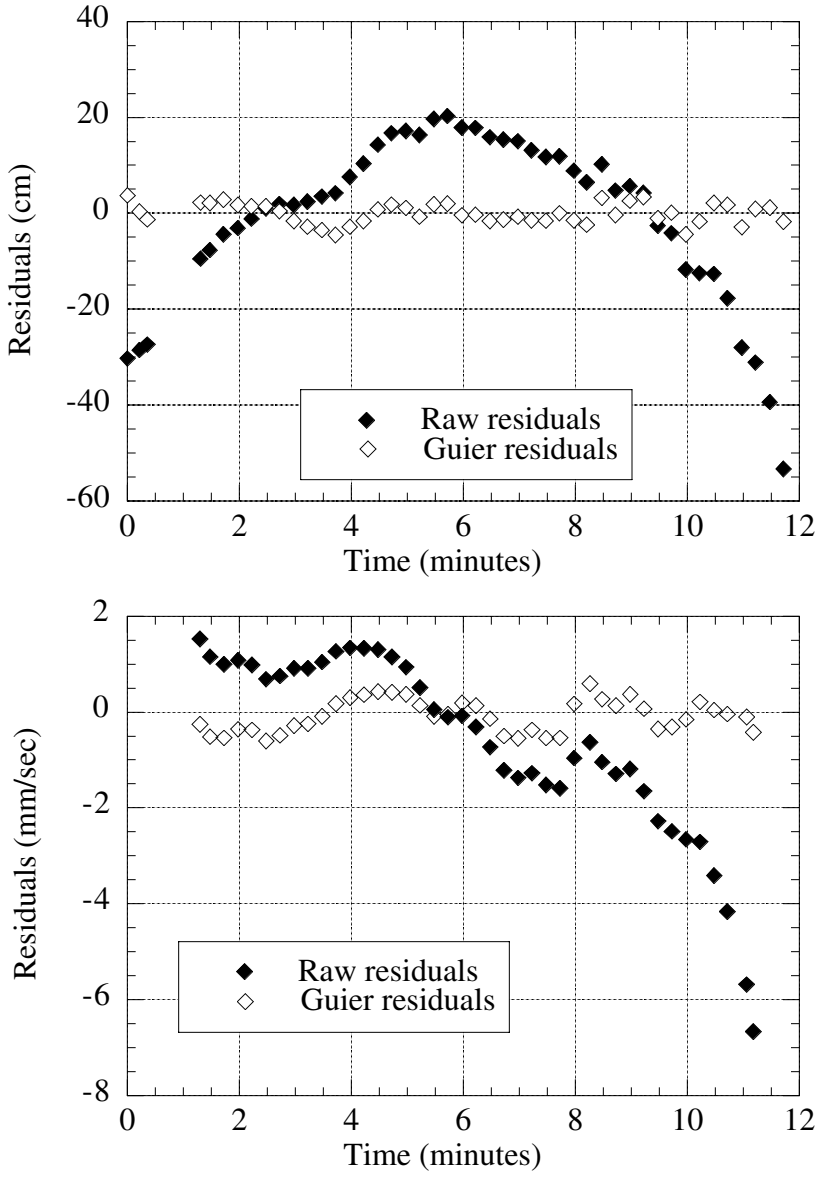

Figure 2.7: Residuals before and after removal of systematic errors for one satellite pass from the Tahiti station. Top: Range residuals, Bottom: Doppler residuals.

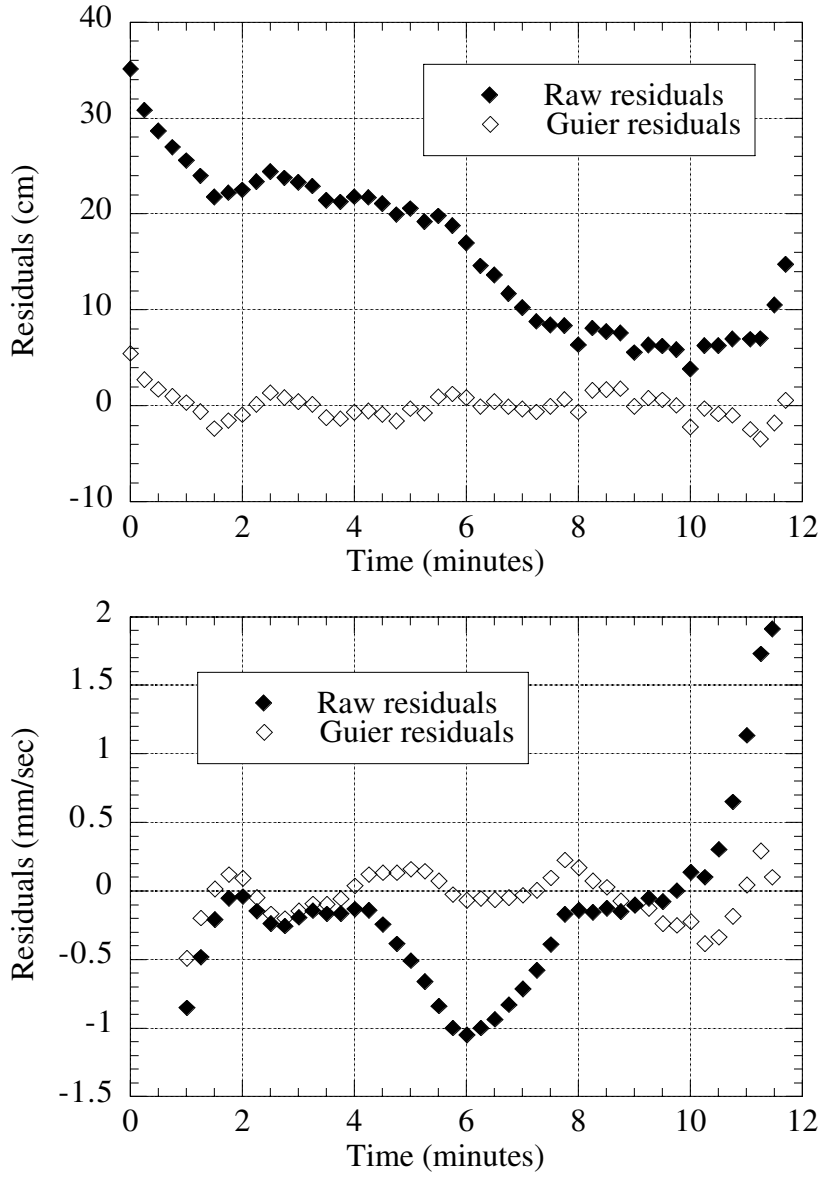

Figure 2.8: Residuals before and after removal of systematic errors for one satellite pass from the Hartebeesthoek station. Top: Range residuals, Bottom: Doppler residuals.

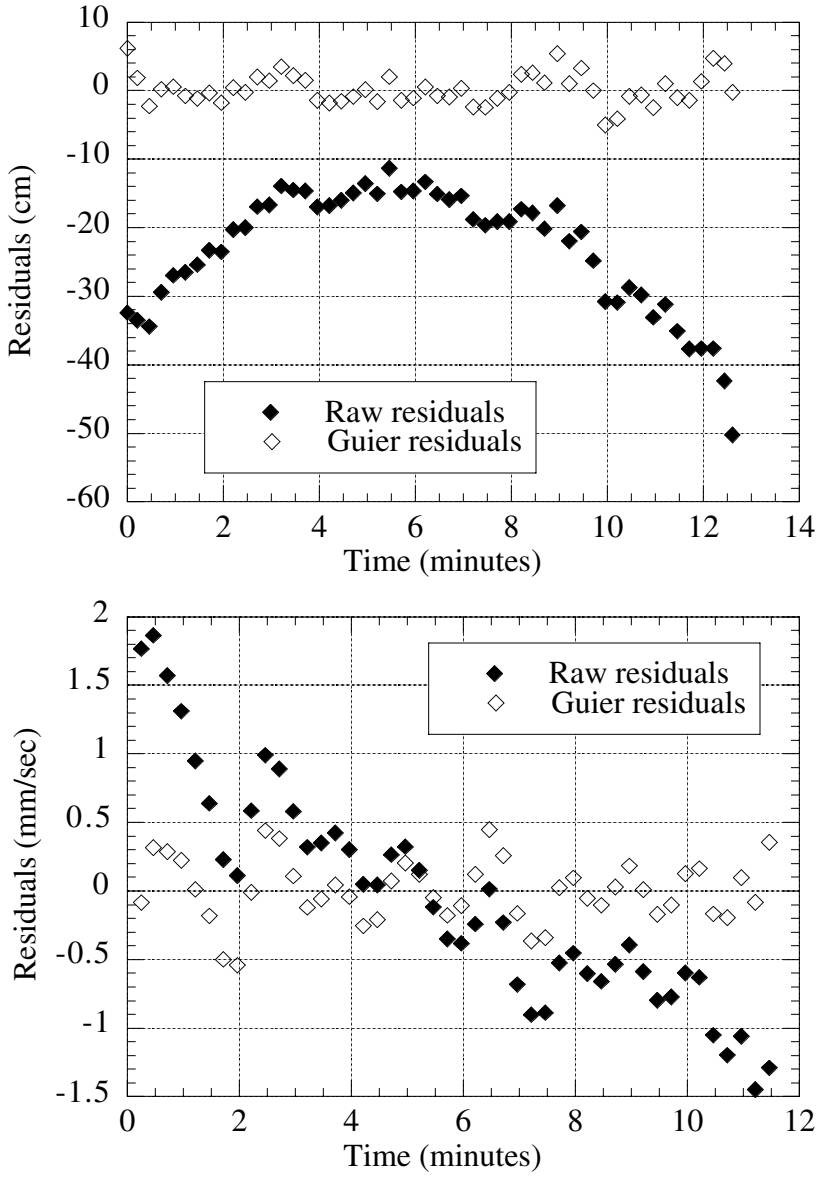

Figure 2.9: Residuals before and after removal of systematic errors for one satellite pass from the Ascension Island station. Top: Range residuals, Bottom: Doppler residuals.

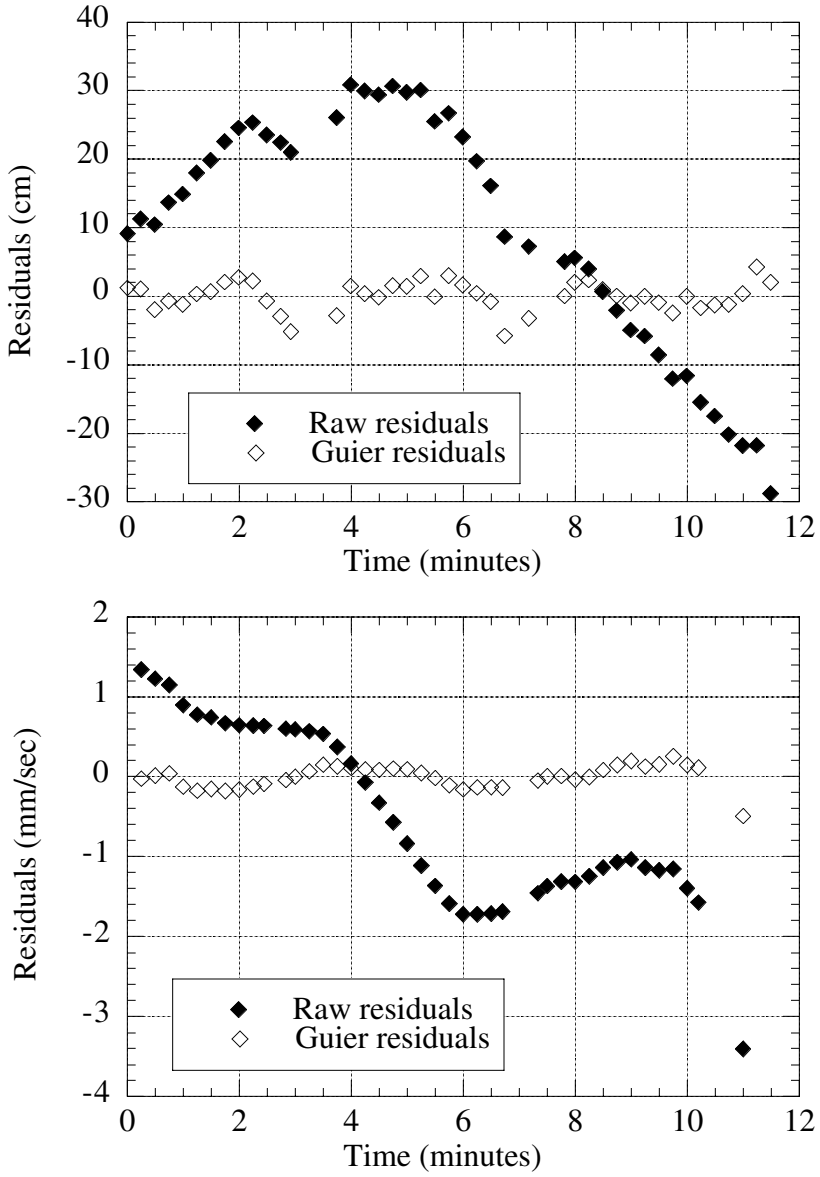

Figure 2.10: Residuals before and after removal of systematic errors for one satellite pass from the UlaanBataar station. Top: Range residuals, Bottom: Doppler residuals.

Table 2.3 gives the statistics for these four particular passes, including the values of the estimated Guier parameters, their uncertainties, and their

correlations. As fairly typical passes, the correlations between the range biases, troposphere scale factors, and slant errors indicate the problem of separating the parameters. This emphasizes the need to estimate the range biases only as infrequently as possible, especially when the station positions are being adjusted. The parameterization for the orbits is discussed further in Chapter 3, while the station positioning strategy is covered in Chapter 4.

Table 2.3: Single pass statistics of passes plotted in Figures 2.7 through 2.10

Pass Characteristics	Fig. 2.7	Fig. 2.8	Fig. 2.9	Fig. 2.10
Date	3/23/96	1/9/96	2/3/96	1/9/96
Time of Day	22:17	9:54	10:36	21:11
# of Range obs.	46	48	49	42
# of Doppler obs.	41	43	46	41
Pass direction	Ascending	Descending	Descending	Ascending
Rise Elevation	7˚	7˚	4˚	8˚
Maximum Elevation	57˚	66˚	54˚	47˚
Set Elevation	4˚	5˚	3˚	4˚
Residual Statistics				
Raw Range RMS (cm)	15.6	18.0	23.3	19.5
Guier Range RMS (cm)	2.1	1.5	2.0	2.1
Raw Dopp. RMS (mm/s)	2.03	0.63	0.80	1.22
Guier Dopp. RMS (mm/s)	0.34	0.17	0.22	0.14
Parameter / Uncertainty				
Slant Error (cm)	13.8 / 3.3	9.8 / 3.0	7.2 / 3.5	23.6 / 3.9
Tangential Error (cm)	0.9 / 1.5	-12.1 / 1.4	-3.3 / 1.3	-18.4 / 1.6
Range Bias (cm)	12.5 / 3.0	4.1 / 2.7	-18.2 / 3.1	3.4 / 3.7
Trop. Scale factor	0.974 / .001	1.009 / .001	0.991 / .001	0.987 / .002
Correlations				
Slant Error - Range Bias	0.83	-0.79	-0.85	-0.87
Tang. Error - Range Bias	0.36	0.36	0.06	0.40
Trop. Scale - Range Bias	0.70	-0.68	-0.76	-0.76

Table 2.4 shows the editing statistics for each of the PRARE stations. The Guier RMS shown for each of the stations gives a feel for how each of the stations are performing relative to the norm. The average Guier RMS, which is interpreted as the observation noise level, is 0.25 mm/s for the Doppler data and 2.5 cm for the range data. It is recognized that this noise level is not Gaussian noise, but does reflect the error level of the data that the orbit fits cannot get below. In comparison, the noise level for DORIS Doppler measurements is about 0.50 mm/s [Davis et al., 1993]. For the SLR tracking stations, the noise levels are between the 0.3 and 3.0 cm levels, depending on the quality of the station [Eanes, 1995].

Table 2.4: Station by station editing results (1997)

Station	Passes remaining	Guier RMS for Doppler (mm/s)	Guier RMS for range (cm)
Tromsoe	431	0.23	2.7
Matera	695	0.22	2.5
Hofn	939	0.27	2.8
Fairbanks	171	0.19	2.4
Tahiti	839	0.31	2.2
O'Higgins	658	0.39	5.8
Syowa	1328	0.20	2.6
Hartebeesthoek	923	0.21	2.0
LaPlata	641	0.20	1.7
Maracaibo	787	0.25	1.8
Ascension	789	0.38	2.7
Bogor	77	0.31	2.3
UlaanBataar	891	0.21	2.2
Kitab	913	0.19	2.3
Greenbelt	1026	0.20	1.9
Kokee Park	869	0.30	2.7
Bangalore	602	0.26	2.3
NyAlesund	1867	0.26	2.8
Potsdam	784	0.24	2.5
Oberpfaffenhofen	9	0.17	2.0
Neumayer	2914	0.23	2.8
Pasadena	533	0.20	1.8

Chapter 3

ERS-2 Precise Orbit Determination

The first and most important function of the PRARE tracking system is to provide the observations used to calculate precise orbits. The goal of this chapter is to evaluate the performance of PRARE data in ERS-2 orbit determination. The strengths and weaknesses of the PRARE data will be discussed, along with how to combine it with the SLR data to provide the best orbits.

The first part of the chapter will give a broad overview of the orbit determination problem, including a description of the nominal models used. Then, procedures for finding the optimal parameterization and data weighting will be discussed. After this, characteristics of the estimated PRARE dependent parameters will be examined. The various methods used to evaluate the orbit accuracy will then be presented. This includes not only examination of the PRARE data fits, but also residual analysis of both SLR and altimeter crossovers, orbit comparisons, and orbit endpoint analysis.

3.1 Description of the Precise Orbit Determination Problem

The orbits for ERS-2 are calculated using the University of Texas Orbit Processor (UTOPIA), which has been modified to process the PRARE observations. This program solves for the satellite state vector (position, velocity, and any other estimated parameters) using a batch processor. The minimum-variance technique is used for the solution of the linearized orbit determination

problem [Tapley, 1973]. This section is intended to give insight into the relationships between the estimated state vector, the dynamic models, and the observation equations. For a more complete description of linear estimation theory applied to orbit determination, see Tapley [1973] or Tapley et al. [1994].

To apply linear estimation techniques, the orbit determination problem is linearized about a reference trajectory where the reference trajectory should be close to the true trajectory. The batch filter maps the observations, using the state transition matrix (which is formed from the differential equations used to describe the motion of the satellite), to some specified epoch. The observations over a certain time span, referred to as the arc length, are mapped back to the arc epoch and are processed to provide the best estimate of the state at the initial epoch. The state estimate at the initial time, using the batch filter with a priori information is represented as:

$$\hat{x} = \left(H^T R^{-1} H + \overline{P}^{-1}\right)^{-1}\left(H^T R^{-1} y + \overline{P}^{-1}\overline{x}\right). \tag{3.1}$$

The set of linearized observations is expressed as:

$$y = H\overline{x} + \varepsilon\,. \tag{3.2}$$

Where:

- $\overline{x}$ is the a priori estimate of the state vector (which includes various force and measurement model parameters in addition to the initial state).
- $\hat{x}$ is the best linear unbiased minimum variance estimate of the deviation of the state vector with respect to the reference trajectory.
- H is the observation-state mapping matrix (observation partials with respect to the state).

R is the specified covariance of the observation error, which here is considered equal to the inverse of the observation weighting matrix.

$\overline{P}$ is the a priori covariance matrix associated with the a priori state, $\bar{x}$.

y is the linearized observation vector (measured minus computed).

ε is the observation error vector, assumed to be random with zero mean and covariance R.

The quality of the orbits is dependent on the accuracy, quantity, and distribution of the observations, the accuracy of the dynamic models used to describe the satellite's motion, the models of the observations, and the parameterization of the state vector. The subsequent sections will describe each of these factors, which have been chosen so as to provide the most accurate ERS-2 orbits.

3.1.1 Distribution and Quality of ERS-2 Observations

The PRARE data is provided from the global network depicted in Figure 1.1. However, the figure gives a somewhat optimistic view, since the stations shown have not operated continuously from the start of 1996 to the start of 1998, which is the time span analyzed in this dissertation. In a typical week, PRARE data is available from 12 to 20 stations. Figure 3.1 shows the PRARE range tracking during one 6-day arc in 1997 (May 18-24), during which 16 stations were operating. Each point plotted in the figure represents one range measurement. The tracking is denser if the Doppler data is also included, although the actual

coverage would not change since the Doppler measurements coincide with the range measurements.

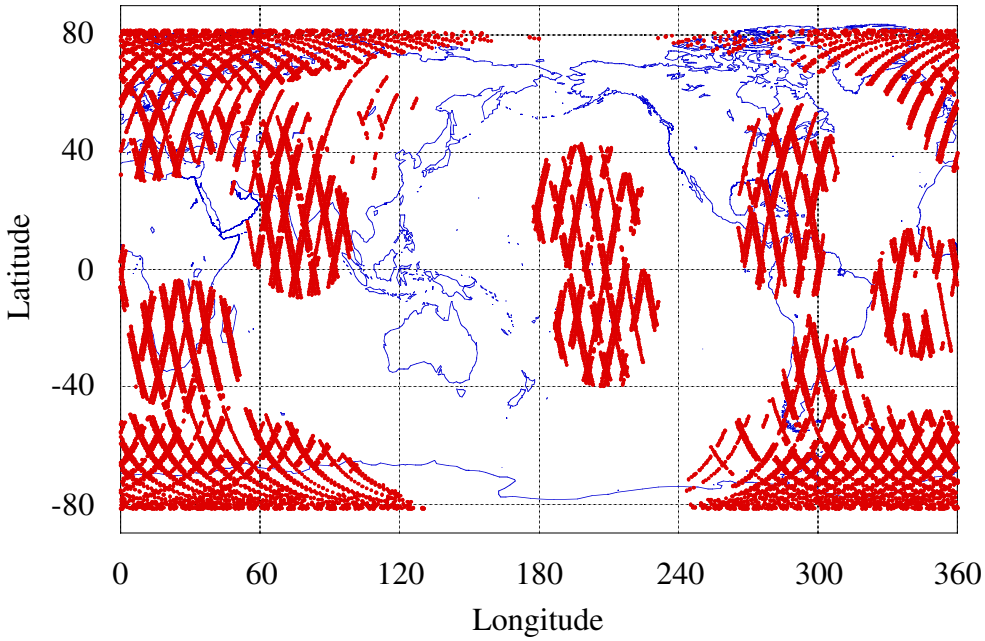

Figure 3.1: PRARE range tracking during a 6-day arc (May 18-24, 1997).

The SLR tracking available during the same 6-day period is shown in Figure 3.2. This represents a fairly typical amount of SLR tracking, with 21 stations tracking. These two figures demonstrate one of the major strengths of the PRARE system relative to the SLR system; the PRARE system provides better coverage, both temporally and spatially. Also, the SLR system is not distributed as well, and unlike PRARE, the laser observations are not made for every pass of ERS-2. The three factors which contribute to the limited number of passes tracked by SLR stations are that many of the SLR stations do not track 24 hours a day,

there is competition between the available targets, and laser ranging cannot be conducted under poor weather conditions.

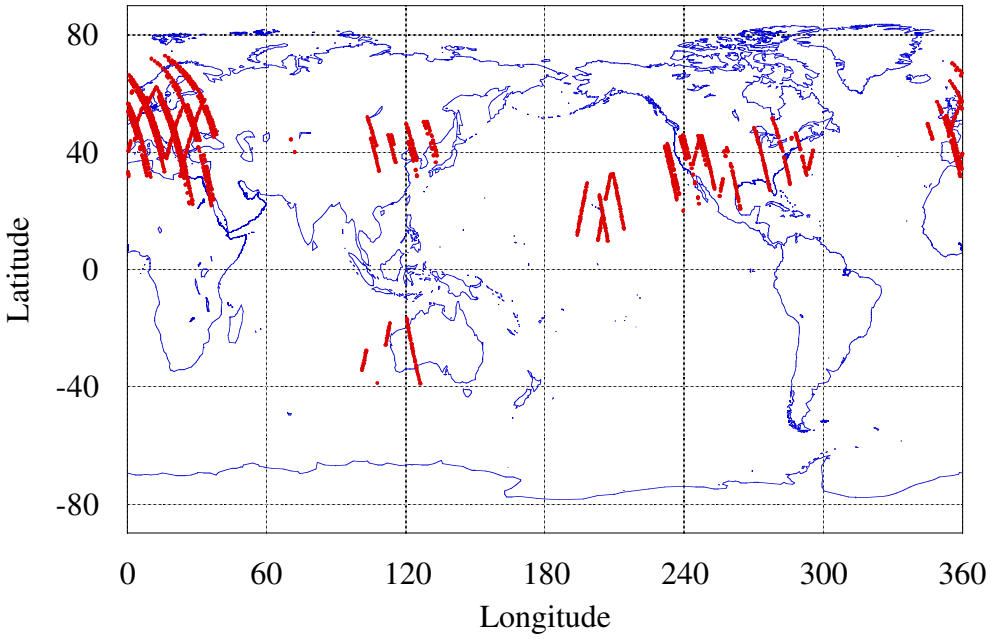

Figure 3.2: SLR range tracking during a 6-day arc (May 18-24, 1997).

Another critical factor in producing accurate orbits is the quality of the observations. As shown in Section 2.3.3, the observation noise level of the PRARE range data is approximately 2.5 cm. For SLR, the observations from the better stations have noise levels approaching 0.3 cm. Additionally, there are other factors that make the SLR measurements stronger than the PRARE data. First, the higher frequency of the laser signal reduces contribution of the wet part of the troposphere delay in comparison to the delay for radiometric measurements. This is significant, since the wet troposphere delay is one of the more ill-determined

corrections applied to the PRARE data. Second, the range biases for the SLR stations are much more stable and better determined than they are for the PRARE stations. Third, the SLR station positions are determined much better than the PRARE stations due to their long history of tracking to satellites with very accurately determined orbits, such as LAGEOS. The end result is that the absolute accuracy of the better SLR normal point measurements is estimated to be about 1.0 cm [Eanes, 1995], which is well below the accuracy of the PRARE range measurements.

The PRARE Doppler measurements have a noise level of 0.25 mm/s, as shown in Section 2.3.3. For comparison purposes, the noise level of the DORIS system, which provides one-way radiometric Doppler measurements for TOPEX/Poseidon, is about 0.5 mm/sec. The older TRANET system, which provided Doppler measurements for GEOSAT, has a measurement noise level of 5.0 mm/sec [Smith, 1988]. These numbers support the fact that the PRARE measurements are of higher quality than those provided by other recent Doppler satellite tracking systems.

3.1.2 The Force Models

The forces that act on the satellite are modeled as precisely as possible in order to accurately describe the motion of the satellite. The more accurate the models, the less necessary it is to adjust dynamic parameters, in order to remove orbit error induced by mismodeling of the forces. This section will describe these force models as they are used in the orbit determination for ERS-2. The force

models can be divided into two distinct types, gravitational forces and non-gravitational forces, which will be described in the following sub-sections.

Gravitational Forces

The non-spherical shape and the nonhomogenious mass distribution of the Earth make it necessary to model the Earth's gravity field as more than just a point mass. The gravitational forces are also known as conservative forces, since these forces can be calculated as the gradient of a potential function. The Earth's potential function is expressed in terms of spherical harmonics and is referred to as the geopotential. The non-spherical part of the geopotential is usually expressed as a spherical harmonic expansion with respect to a body fixed reference frame [Kaula, 1966]:

$$U(r,\phi,\lambda) = \frac{GM}{r}\sum_{l=1}^{\infty}\sum_{m=0}^{l}\left(\frac{a_e}{r}\right)^l \overline{P}_{lm}(\sin\phi)\left[\overline{C}_{lm}\cos m\lambda + \overline{S}_{lm}\sin m\lambda\right] \qquad (3.3)$$

where r,ϕ,λ are the radial distance, latitude and longitude, GM is the gravitational constant of the Earth, a_e is the mean equatorial radius of the Earth, $\overline{P}_{lm}$ are the normalized associated Legendre functions of degree l and order m, and $\overline{C}_{lm}$ and $\overline{S}_{lm}$ are the normalized spherical harmonic coefficients. The first degree spherical harmonic coefficients are equal to zero when the origin of the body fixed reference frame is defined as the geocenter. The perturbations in the motion of a satellite due to the non-spherical geopotential are determined by taking the gradient of Equation 3.3.

For this research, the University of Texas Earth Gravitational model (TEG-3) is used [Tapley et al., 1997], which is complete up to degree and order 70. This is the same gravity model used to produce the most recent UT/CSR ERS-1 ephemeris. It includes a significant amount of SLR tracking data and altimetry from both Stella and ERS-1, which are in orbits with similar inclinations and altitudes to ERS-2. The presence of this data in the TEG-3 gravity model results in the model being somewhat tuned for ERS-2 POD. Further discussion of the gravity field models is presented in Chapter 5.

The geopotential is altered by the gravitational pull of the Sun and the Moon. The elastic deformation of the solid Earth results in variations of the geopotential which are referred to as solid Earth tides. Additionally, the gravitational forces of the Sun and Moon cause ocean tides, which also induce time varying effects to the geopotential. The resulting variations in the geopotential, are expressed as time varying changes in the standard normalized geopotential coefficients [Eanes et al., 1983].

The Earth's potential is also effected by the variation in the rotation rate and axis of rotation of the Earth, known as polar motion. The effect of these variations on the geopotential is called rotational deformation or pole tide. Again, the pole tide is accounted for by modeling the effect as variations to a few of the standard normalized geopotential coefficients [Lambeck, 1980].

The Sun, Moon, and planets all cause N-body perturbations to the satellite's orbit around the Earth. These perturbing bodies are all modeled as point masses in determining the gravitational force applied to the satellite, where the planet positions are determined using JPL DE-2000 ephemerides [Standish 1982].

The last of the gravitational forces to be accounted for in orbit determination is effects of the acceleration of a near-Earth satellite due to general relativity [Ries, 1989].

Non-gravitational Forces

The non-gravitational forces are non-conservative in nature and are applied directly to the surface of the spacecraft. Thus these forces are often called surface forces. A more detailed description of these forces for precise orbit determination is given by Ries et al. [1993]. One of the main surface forces for a satellite at the ERS-2 altitude is atmospheric drag. The drag acts in the opposite direction of the velocity of the spacecraft relative to the surrounding atmosphere. To calculate the drag for ERS-2, the spacecraft bus is modeled as a box, while the solar panel is modeled as a rectangular wing. The drag is then computed by determining the cross-sectional area of the box-wing model perpendicular to the relative wind velocity. Another factor in the calculation of drag is the model used to determine the density of the atmosphere. The model used in this research is the Density and Temperature Model (DTM) [Barlier et al., 1978]. The atmospheric drag is easily mismodeled, since determination of the cross-sectional area and the atmospheric density are both imprecise.

The other dominant surface force is Solar radiation pressure, which is caused by the momentum transfer of photons from the Sun hitting the satellite. This force acts in the Sun-to-satellite direction, and is dependent on the solar flux and the reflectivity coefficient of the satellite. A similar force is the Earth radiation pressure, which is caused by the combination of solar radiation reflected from the Earth and long-wavelength radiation (heat) emitted from the Earth. Both

of these surface forces can also be easily mismodeled, since the Earth flux, cross-sectional area, and reflectivity coefficient of the satellite are imprecise.

3.1.3 Orbit Parameterization and Data Weighting

As described in the previous sections, and in the first part of Chapter 2, both the force and measurement models used to generate the orbits can have errors which will manifest themselves in the orbit if they are not accounted for properly. The arc length used can be a critical factor in the accuracy of the orbits. In general, longer arc lengths are preferred, since they allow the accumulation of more satellite tracking. On the other hand, if the orbital arc is too long, the effects of the mismodeled forces build up in the orbits. An arc length of around six days has been adopted for both ERS-1 and ERS-2 as a sort of standard for producing orbits for these satellites. This arc length provides adequate tracking data while preventing the buildup of orbit errors due to mismodeled forces. The other factor which goes into determining the arc length is the large number of orbital maneuvers that ERS-2 performs to maintain the constraints imposed on its orbit ground track and attitude. In general, maneuvers are performed once or twice a month. The frequency of these maneuvers is high because the combination of low altitude and large, complex cross-sectional area induces large surface forces on ERS-2. Additionally, the low altitude orbit makes it more sensitive to the gravity perturbations. The thrusts associated with the maneuvers can cause rapid changes in the position and velocity of the satellite which are hard to model accurately. The safest way to handle the maneuvers is to mandate arc breaks at each of the burns. In effect, the thrust intervals create discontinuities in the orbit. In summary,

the arc lengths are chosen to be close to six days long, with arc breaks automatically designated at the maneuvers.

To prevent the measurement and force model errors from degrading the orbit, these errors must be accommodated in some way. A large part of the gravitational and radiation pressure errors exhibit a one-cycle-per-revolution (1-cpr) frequency, where revolution refers to the orbital period of the satellite [Ries et al., 1993]. The acceleration caused by these forces is conveniently expressed in the satellite-fixed radial, transverse, and normal directions. For both ERS-1 and ERS-2, empirical 1-cpr accelerations in both the transverse and normal directions are added to the state vector. These parameters are very effective in absorbing large portions of dynamic model errors, provided there is sufficient tracking data. The frequency that these parameters are estimated is a function of both the amount of tracking available and the amount of variability in the dynamic model errors which are manifested as 1-cpr orbit errors.

The other dynamic parameters which are estimated in the state vector are drag coefficients (Cd's). The Cd's absorb the errors made in mismodeling the atmospheric drag force. As stated earlier, the drag forces on ERS-2 can be large, so errors in the model for these forces will result in large orbit errors unless they are accounted for.

The increased amount of tracking for ERS-2, due to the addition of PRARE data, allows the dynamic parameters to be estimated more frequently than for ERS-1. For ERS-1, the orbits are computed by estimating the 1-cpr accelerations once every 72 hours and the Cd's once every 6 hours. The optimal frequency for ERS-2 is determined by performing a sensitivity study over a

typical 105 day period in 1997, as shown in Table 3.1. The estimate of the radial orbit accuracy compared in the table is obtained from analysis of the SLR residuals, which is discussed later in this chapter (Section 3.3.3). The time spans considered for the 1-cpr accelerations are 24 hours, 32 hours, and 48 hours and for the Cd's are 6 hours, 8 hours, and 12 hours. From the table, it is apparent that the best performance is obtained when the 1-cpr accelerations are estimated every 32 hours and the Cd's are estimated every 8 hours. Estimating the dynamic parameters with this frequency is conservative enough so that both the 1-cpr accelerations and the Cd's remain stable, even when there is somewhat less tracking than normal. This is important, since it makes the orbits less susceptible to orbit run-off that may occur during times with less than the nominal amount of tracking data.

Table 3.1: Dynamic parameter frequency impact on estimated radial orbit errors (cm)

	Frequency of 1-cpr parameter estimation		
	24 hours	32 hours	48 hours
6 hour Cd's	3.2	3.2	3.2
8 hour Cd's	3.1	3.0	3.2
12 hour Cd's	3.3	3.2	3.3

The weights given to each of the tracking data types in the orbit solution are based on the accuracies of the measurements and also on consideration of the various modeling errors. The accuracy of the SLR normal points is around 1 cm for the best SLR stations, although for some of the older and less reliable stations

the accuracy levels are lower. The weight given to the SLR data is a function of the quality of the tracking station, following the algorithm outlined in Tapley et al. [1993]. The a priori standard deviations of the SLR data are given values ranging from 10 to 100 cm, depending on the quality of the station. The measurement noise of the PRARE data is estimated to be 2.5 cm and 0.25 mm/sec for the range and Doppler data, respectively. But, the true uncertainty of these measurements is significantly greater due to uncertainties in the atmospheric delay corrections, the internal station delay measurements, and the time tags.

The inclusion of the PRARE data, with the proper weight in ERS-2 POD, should not have an excessive effect on the fits of the orbits to the SLR data. Because the PRARE system provides roughly 15 times the data as SLR, the PRARE data must be given a lower weight than the precision of the measurements indicates. An a priori standard deviation of 20 cm for the range data and 2 mm/sec for the Doppler data gives the PRARE data enough weight to contribute to the orbits, while not overpowering the SLR data. This also tends to provide reasonable standard deviations for the estimated parameters.

The orbits are not overly sensitive to the relative weight assigned to the PRARE data with respect to the SLR data. For example, when the a priori uncertainties of the PRARE data are changed by ± 5 cm (and 0.5 mm/sec for Doppler) the orbits change by less than 2 mm in the radial direction, in an RMS sense. Additionally, a closer look at the relative weight between the PRARE range observations and the PRARE Doppler observations reveals that the orbits do not change significantly when the a priori uncertainty of the Doppler data is changed. The a priori standard deviation of the Doppler measurements was reduced from

20 cm to 10 cm resulting in a radial orbit difference of 2 mm, in an RMS sense. Likewise, when the Doppler data is down-weighted so that the a priori uncertainty is 30 cm, the RMS of the radial differences between orbits is only 1 mm. In both cases, the SLR and altimeter crossover fits change very little. Therefore, the relative a priori uncertainty between the range and Doppler measurements is kept at 20 cm to 2 mm/sec, respectively.

The satellite altimetry is given negligible weight in the ERS-2 orbit solution, unless noted otherwise. For information on the use of altimeter crossovers in precise orbit determination for ERS-1, see Kozel [1995] and Shum et al. [1990].

3.1.4 Reference Coordinate Frame and Station Coordinates

The terrestrial reference frame used for the station coordinates is defined by the SLR station solution (SLR95L01) made from observing the Lageos satellites [Tapley et al., 1993]. The Lageos solution provides a reference system which accounts for polar motion, precession and nutation, and tectonic plate velocities. The estimation of the PRARE coordinates (CSR98P01) used in this chapter is discussed in Chapter 4. The PRARE site velocities are taken from the SLR solution for those stations which are in close proximity to SLR stations. The International Terrestrial Reference Frame (ITRF96) [Boucher et al., 1998] is used to supply the velocities for as many of the remaining stations as possible. For the rest of the stations, the NNR-NUVEL plate motion model by DeMets et al. [1994] is used to compute station velocities. Table 3.2 gives the velocities for each of the

PRARE stations. Table 3.3 summarizes all the models, orbit parameters, and tracking data weights used for the ERS-2 orbits as presented in this section.

Table 3.2: Station velocities (mm/year)

Station	ID	Source	X-dot	Y-dot	Z-dot
Tromsoe	7702	ITRF96	-18.19	7.35	4.72
Matera	7704	ITRF96	-18.91	19.19	13.62
Hofn	7707	ITRF96	-9.53	13.64	7.50
Fairbanks	7708	ITRF96	-21.51	-4.25	-9.69
Tahiti	7709	Plate	-41.75	51.63	31.46
O'Higgins	7710	ITRF96	17.89	0.65	2.50
Syowa	7711	ITRF96	14.96	-2.29	1.57
Harteb'sthoek	7714	ITRF96	0.73	19.18	16.41
LaPlata	7715	ITRF96	3.43	-6.06	8.03
Maracaibo	7716	Plate	5.58	3.43	7.99
Ascension	7717	Plate	-0.05	-6.43	11.22
Bogor	7719	Plate	-17.87	-6.63	-10.63
UlaanBataar	7720	Plate	-25.30	0.70	-7.40
Kitab	7721	ITRF96	-27.83	10.67	4.32
Greenbelt	7722	CSR95L01	-18.25	1.80	6.24
Kokee Park	7724	ITRF96	-8.14	61.85	30.18
Bangalore	7725	Plate	-43.00	-0.40	42.30
NyAlesund	7728	ITRF96	-16.85	7.62	0.93
Potsdam	7730	Plate	-15.23	17.42	8.46
Shanghai	7734	ITRF96	-30.95	-11.70	-11.98
Oberpf'hofen	7736	ITRF96	-14.15	19.02	11.19
Greenbelt	7755	CSR95L01	-18.25	1.80	6.24
Pasadena	7758	CSR95L01	-24.25	19.32	6.98

Table 3.3: Summary of force models, orbit parameters, and tracking data weighting.

Force	Model
Geopotential	TEG-3
Ocean Tides and EOP	CSR3.0
Solid Earth Tides	Applied
Solar Radiation Pressure	Box-wing
Earth Radiation Pressure	Box-wing
Atmospheric Drag Model	Box-wing
Atmospheric Density Model	DTM
Relativity	one body
Estimated Parameters	Frequency
Satellite state	6 days
Cd	8 hours
Transverse & Normal 1-cpr accelerations	32 hours
PRARE range biases	6 days (*)
Wet zenith troposphere delay scale	every pass of PRARE data (*)
time bias	every 6 days for PRARE data (*)
Tracking data	A priori standard deviation
SLR	10 cm - 100 cm
PRARE range	20 cm
PRARE Doppler	2.0 mm/sec
Crossovers	---
Station Coordinates	System
SLR	CSR95L01
PRARE	CSR98P01
	* Discussed in Section 3.2

3.2 THE PRARE DEPENDENT PARAMETERS

There are several kinematic parameters that need to be estimated in order to remove measurement errors in the PRARE data. These parameters are range biases, zenith wet troposphere delay scale factors, and PRARE system time

biases. The calculated range observations, used to determine *y* in Equation 3.1, are made using:

$$\rho_{calc} = \frac{1}{2}\left\|\left[R_s(t_3) - R_g(t_2)\right] + \left[R_s(t_1) - R_g(t_2)\right]\right\| + \rho_{bias} + \Delta\rho_{z_{dry}} M_{dry} + \alpha\Delta\rho_{z_{wet}} M_{wet}, \tag{3.4}$$

from Equations 2.2 and 2.12. The ρ_{bias} and α terms are the range biases and troposphere zenith wet delay scale factors, respectively. The corresponding equation for the Doppler observations is:

$$\left(\frac{\Delta\rho}{\Delta t}\right)_{calc} = \left(\rho_{calc_{end}} - \rho_{calc_{start}}\right) \Big/ \Delta t_{count}\,, \tag{3.5}$$

where ρ_{calc} is obtained from Equation 3.4. As expected, the range bias cancels out for the Doppler measurements, while the troposphere scale factor remains.

3.2.1 The PRARE Range Bias

The estimation of range biases can weaken the tracking data significantly as the frequency of the estimates increases. In the limiting case, when the range biases are estimated for every pass, the range data is really no more than integrated Doppler or biased range. Therefore, it is desirable to estimate the range biases only as often as required. The first step in determining how often to estimate the biases is to examine the stability of the biases for each station. Figures 3.3 through 3.10 show range biases plotted for the stations that operated most frequently over the two year span being investigated. Each plot shows the biases for two cases, where the biases are estimated every pass and where the passes are estimated once every arc (6 days).

The arc range biases shown in these plots illustrate that they can not be considered constant over periods longer than 6 days. The question is whether or not the biases need to be estimated every pass. If the difference between the pass and arc biases is minimal, they can be accounted for by the weakness of the pass bias solutions. The pass dependent bias estimates are weaker not only because they are based on less data, but also because of the correlation with the pass-dependent troposphere scale factors.

For most of the stations the pass-dependent biases differ from the arc biases on the order of 10 cm or less. These kinds of differences may be accounted for as errors or weakness in the estimates, and not necessarily actual variations in the station performance. This indicates that estimating the biases every arc is sufficient for most cases.

For Tromsoe during a large part of 1996 (top of Figure 3.3), the biases estimated every pass show large discrepancies from the biases estimated every arc. In fact, many of the differences are larger than 50 cm. Differences of this magnitude indicate that the arc dependent biases are not frequent enough to account for the actual instability of the station. It is also interesting that the range biases for Tromsoe show much better agreement in early 1996, just before the station stopped providing data for a couple of months. After the RF cable for the Tromsoe station was replaced in early 1997, the pass biases became more stable. Similarly, the pass biases from the O'Higgins station (bottom of Figure 3.4) show very large discrepancies from the arc biases towards the end of 1996. Again, the magnitude of the differences was reduced when the RF cable was replaced at the end of 1997.

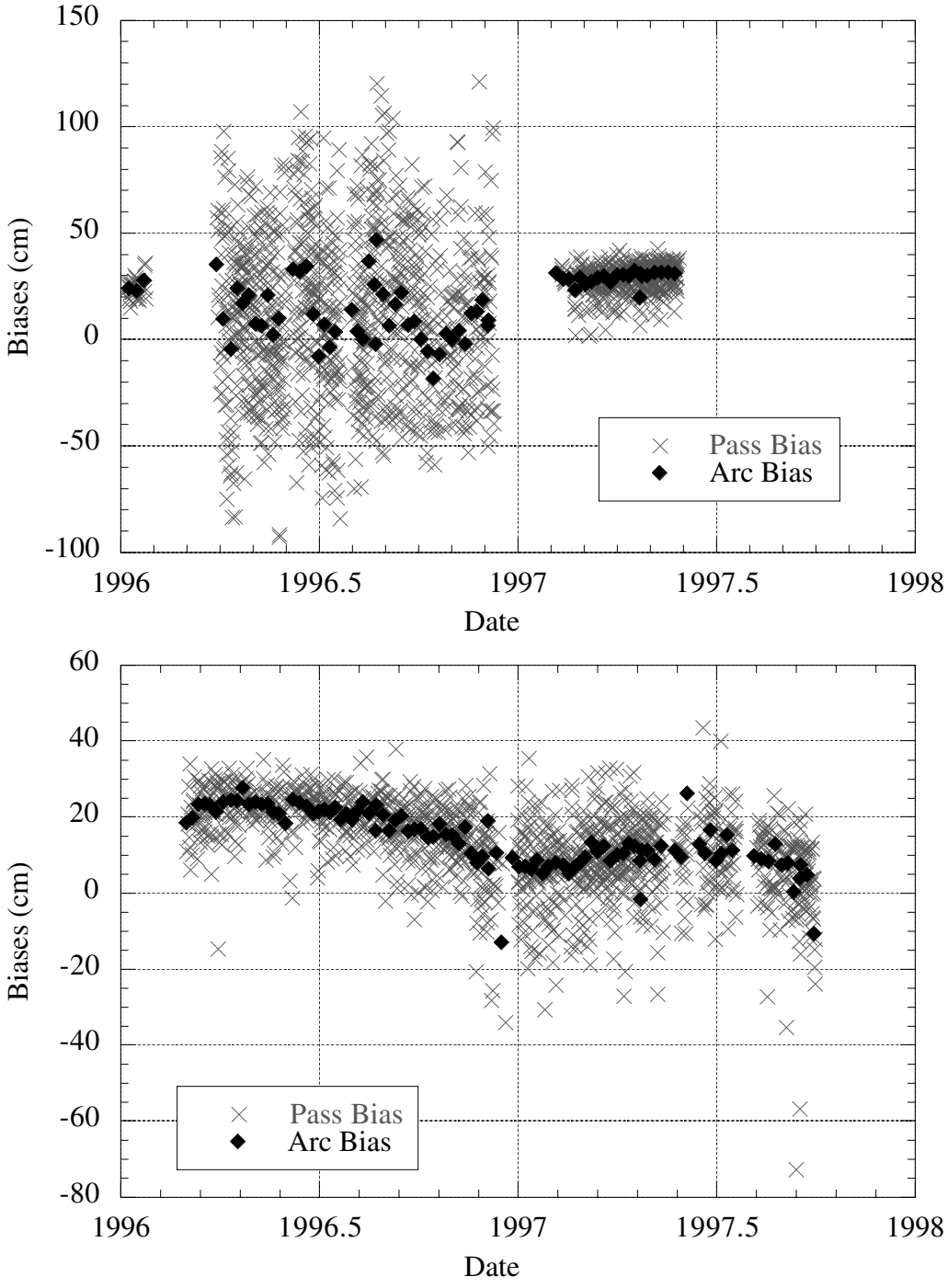

Figure 3.3: Range biases - Top: Tromsoe, Norway - Bottom: Matera, Italy.

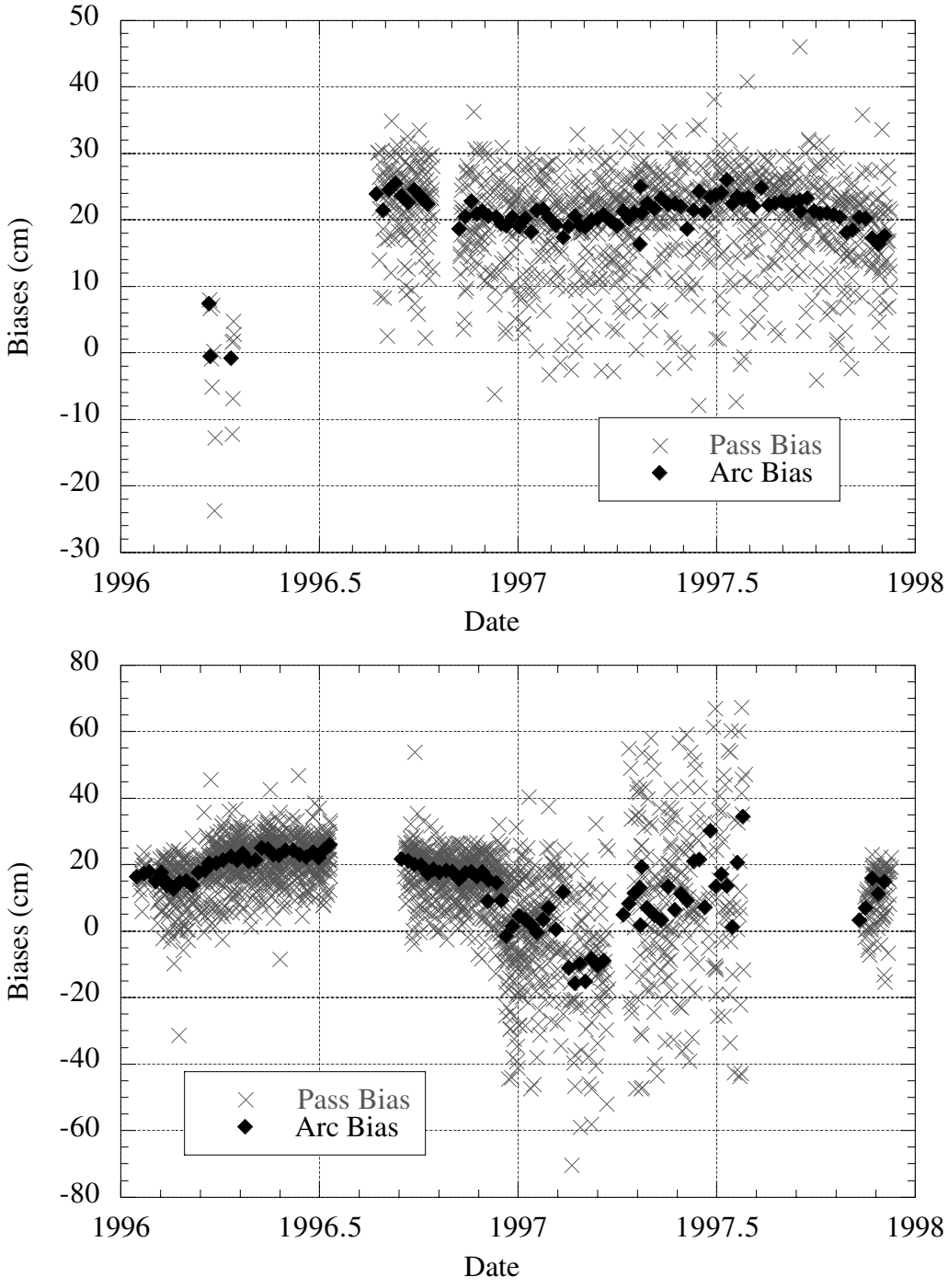

Figure 3.4: Range biases - Top: Tahiti - Bottom: O'Higgins, Antarctica.

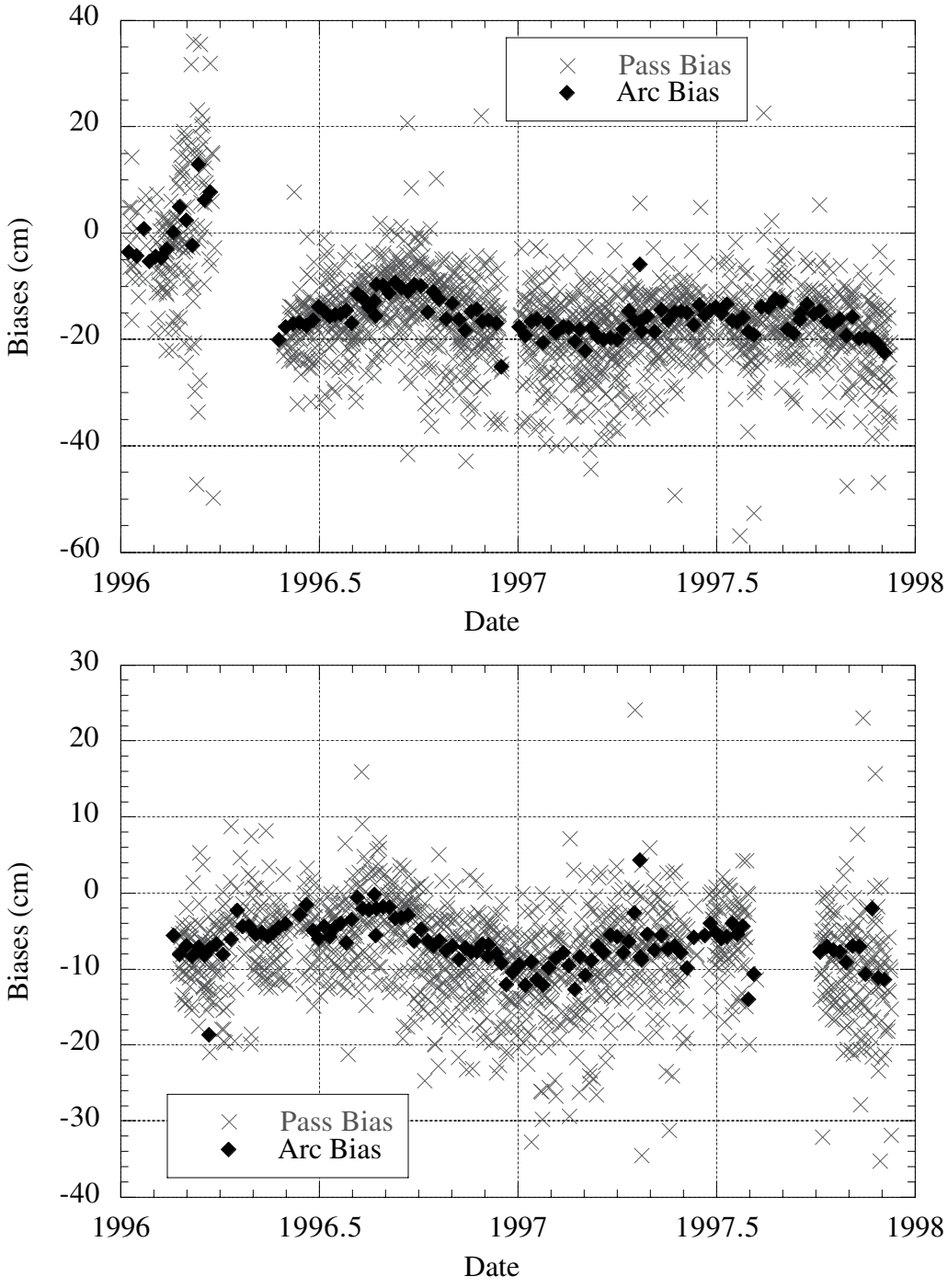

Figure 3.5: Range biases - Top: Hartebeesthoek, South Africa - Bottom: La Plata, Argentina.

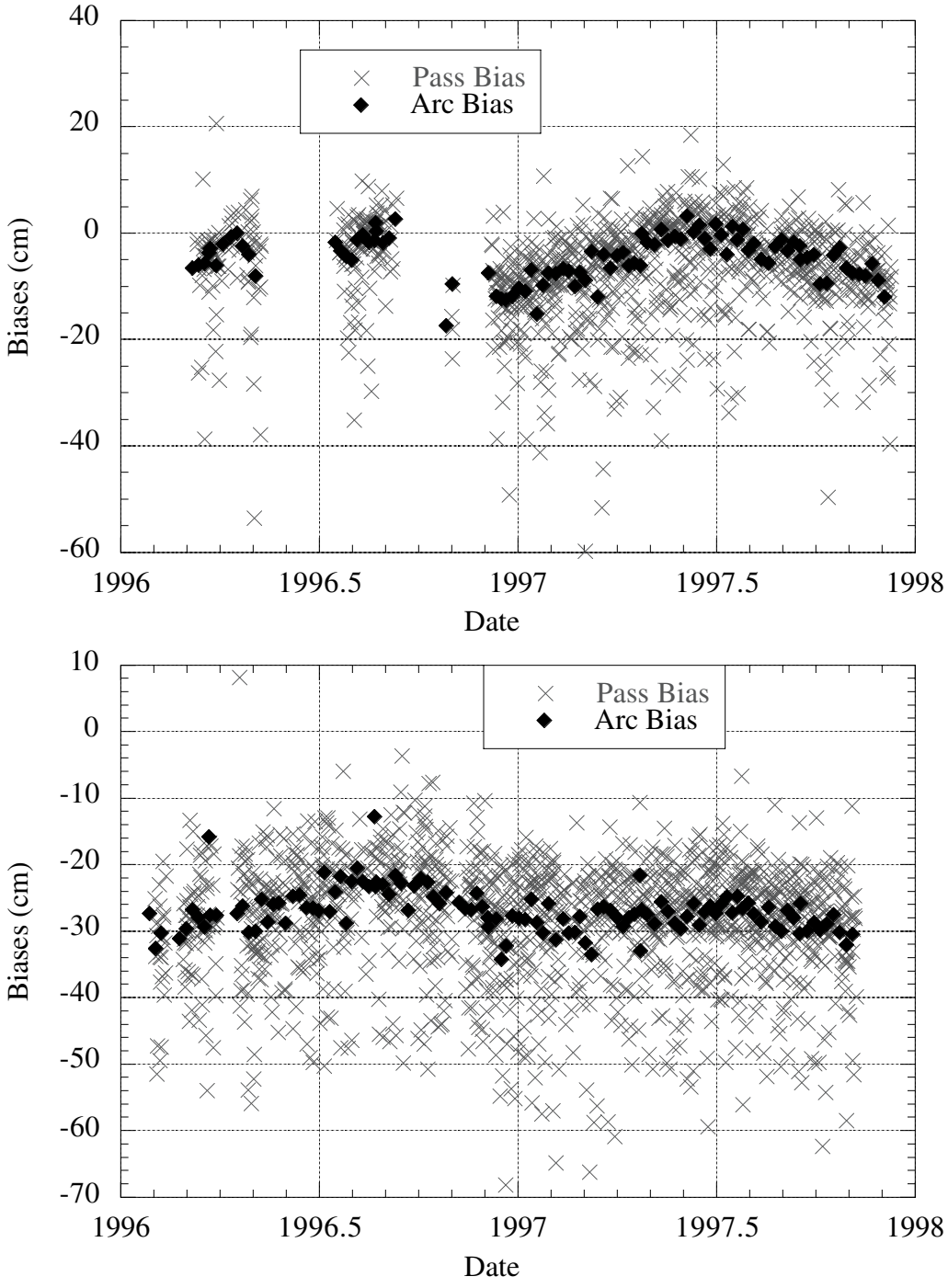

Figure 3.6: Range biases - Top: Maracaibo, Venezuela - Bottom: Ascension Island.

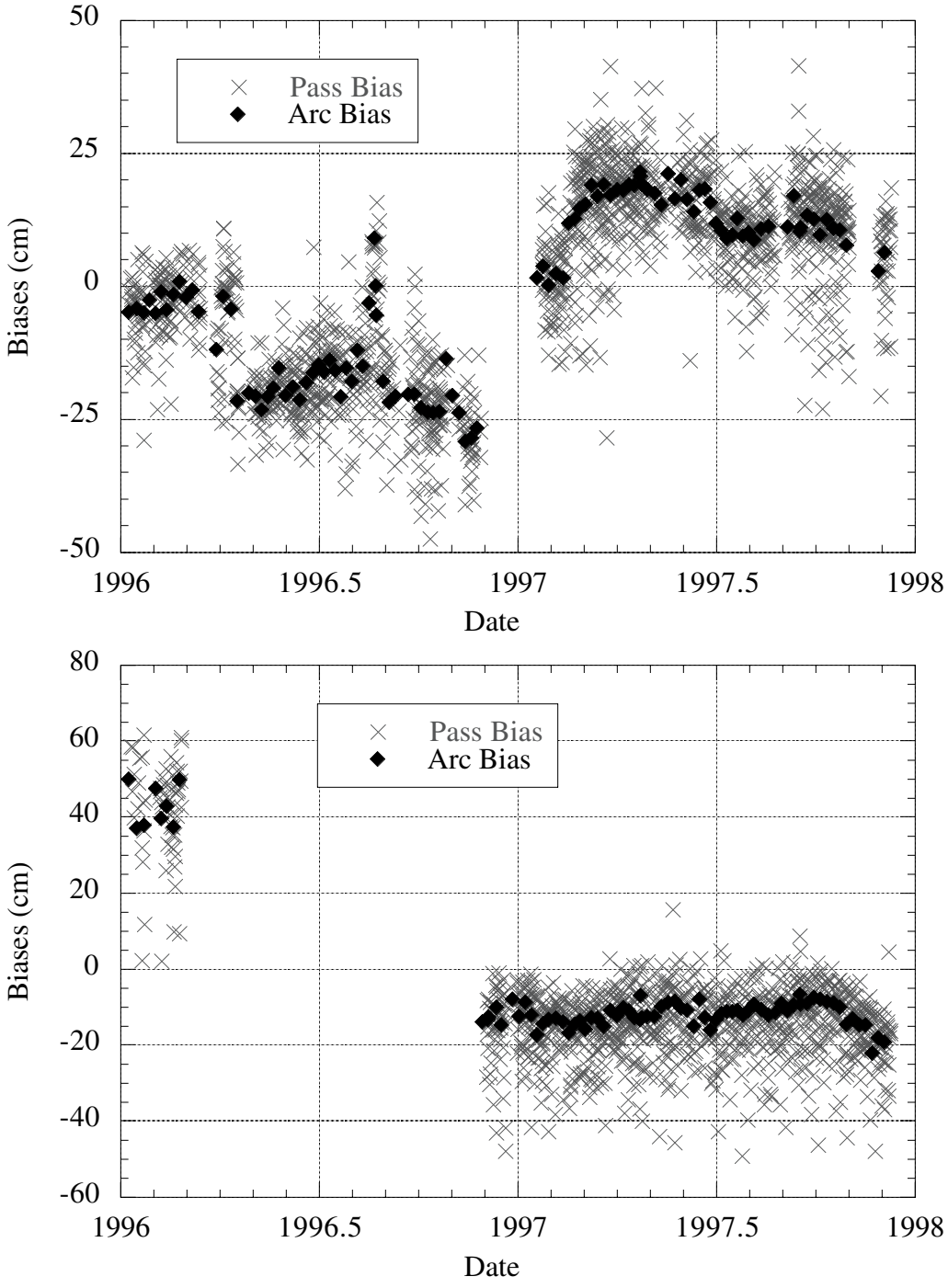

Figure 3.7: Range biases - Top: UlaanBataar, Mongolia - Bottom: Kitab, Uzbekistan.

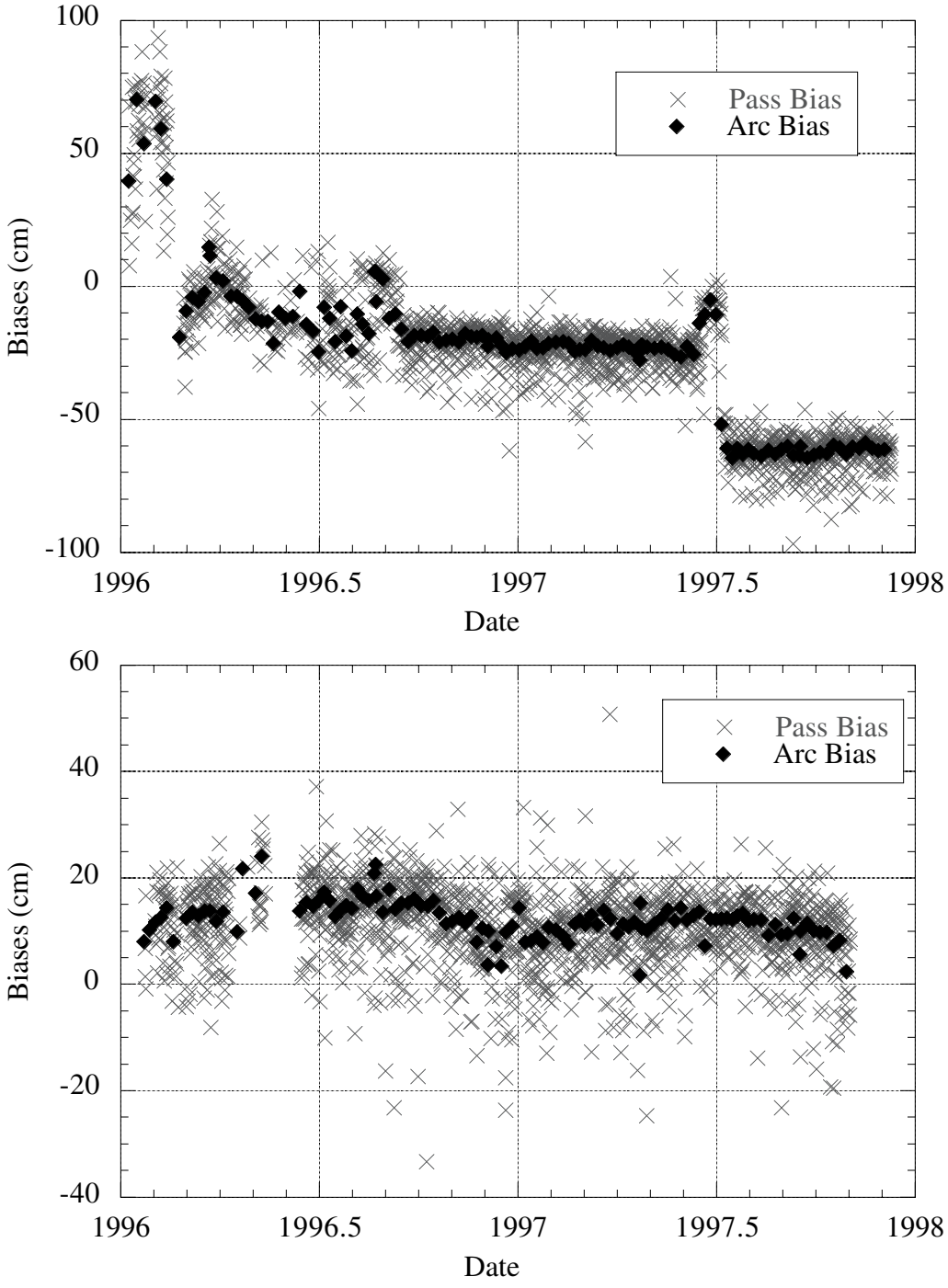

Figure 3.8: Range biases - Top: Greenbelt, Maryland - Bottom: Kokee Park, Hawaii.

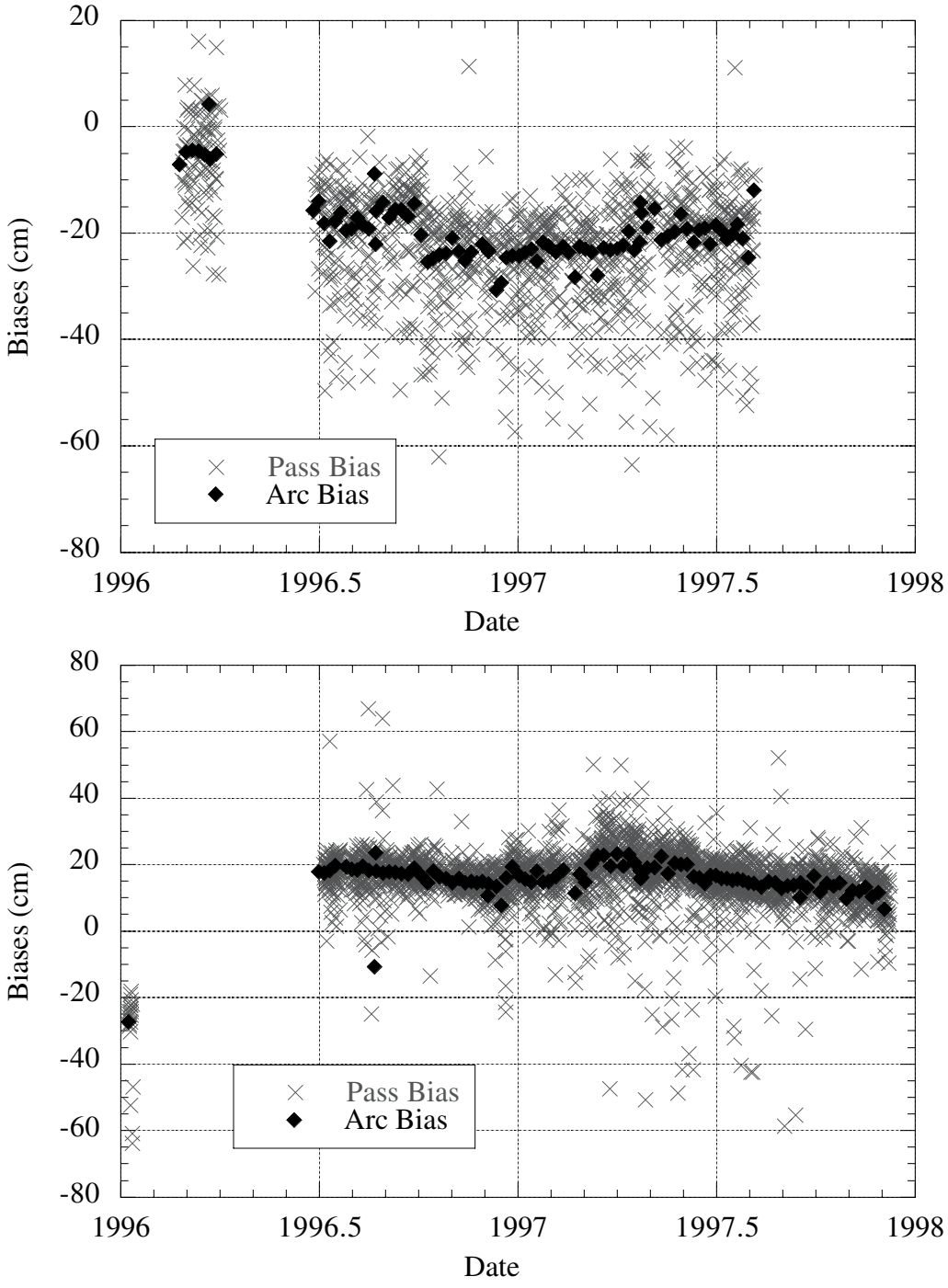

Figure 3.9: Range biases - Top: Bangalore, India - Bottom: NyAlesund, Spitzbergn.

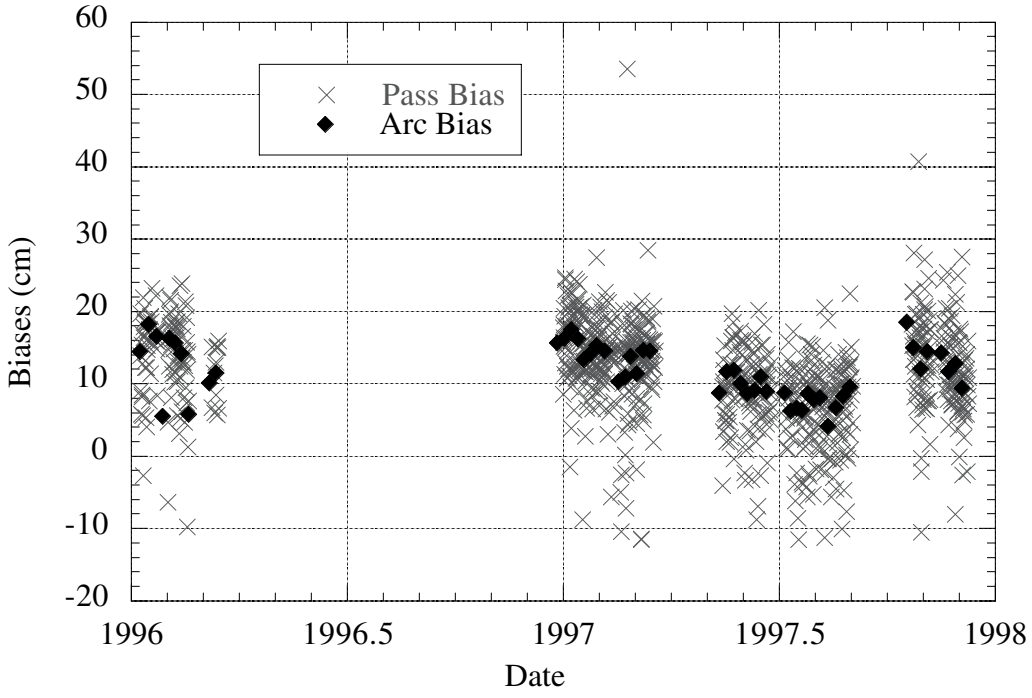

Figure 3.10: Range biases - Potsdam, Germany.

In summary, most of the stations exhibit enough stability in their biases to warrant estimating the biases every arc. The RMS of the differences between arc and pass biases for each station is presented in Table 3.4. From this analysis, pass-dependent biases are estimated for Tromsoe in 1996, O'Higgins in 1997, and Neumayer for both years. The Neumayer station is a special situation and will be addressed in detail in the second half of Chapter 4.

Care needs to be taken in this matter, since a station could become unstable at any time, thus making it necessary to start estimating the biases every pass. The easier, and safer, solution is to estimate the biases every pass for all the stations. However, this would unnecessarily weaken the majority of the range

measurements and degrade the accuracy of the computed orbits. Since the objective of this research is to determine how the PRARE data can be used to determine the most accurate ERS-2 orbits, for the remainder of this dissertation the biases will be estimated once per arc for all stations except as noted above.

Table 3.4: RMS of the differences between arc and pass biases (cm)

Station	ID	1996	1997
Ascension Island	7717	8.9	8.9
Bangalore	7725	9.4	10.1
Fairbanks	7708	*	5.9
Greenbelt	7722	9.8	6.6
Greenbelt	7755	6.9	*
Hartebeesthoek	7714	8.7	7.2
Hofn	7707	--	7.1
Kitab	7721	12.0	9.0
Kokee Park	7724	7.4	7.0
La Plata	7715	5.4	6.5
Maracaibo	7716	8.7	8.6
Matera	7704	7.2	10.7
Neumayer	7754	28.9	30.4
NyAlesund	7728	6.4	8.7
Oberpfaffenhofen	7736	5.4	3.9
O'Higgins	7710	7.3	19.3
Pasadena	7758	--	4.8
Potsdam	7730	5.7	6.0
Shanghai	7734	10.6	--
Syowa	7711	--	11.1
Tahiti	7709	6.8	7.4
Tromsoe	7702	36.7	6.3
UlaanBataar	7720	7.0	8.1

* The Greenbelt station (7755) was moved to Fairbanks (7708) in 1997.

3.2.2 Zenith wet troposphere delay scale factors

The wet troposphere delay, as described in Chapter 2, is not very well determined due to the lack of accurate knowledge of the atmospheric conditions along the signal path. To prevent the errors in the calculated wet delay from being absorbed into the orbits, a scale factor for the computed zenith wet delay is estimated for every pass of PRARE tracking (α in Equation 3.4). Both the range and Doppler measurements contribute to this scale factor.

By examining the values of the estimated troposphere scale factors, we can evaluate the performance of the calculated zenith wet delays. Table 3.5 shows the mean and RMS about the mean of the scale factors for each of the stations during 1996. The mean values for most of the stations are close to one, which indicates that the computed zenith wet troposphere delay is relatively unbiased. There are a few stations, however, where there does seem to be a significant bias that the scale factor is trying to accommodate. It is unclear whether this bias is caused by an offset in the wet troposphere delay calculation, or if the scale factor is compensating for some consistent error in the range bias estimate, the actual station measurements, the vertical station position, or an error in the applied ionosphere correction.

Even after the special attention given to the meteorological data used for determining the troposphere delay, the RMS of the estimates in Table 3.5 show how poorly the wet troposphere delay is determined. The variability of the scale factors for each station ranges from 10 to over 60 percent. However, since this scale factor is only for the zenith wet delay which ranges from 1 to 30 cm, these results are not as bad as they may sound. For reference, the dry zenith troposphere

delay usually varies from 2.0 to 2.3 meters, so even a large error in the wet delay is only a small fraction of the total tropospheric delay. However, the error in the dry delay is much less than the error in the wet delay since the dry delay is much easier to model. Another point is that most of the stations with highly variable scale factor estimates are those that have the smaller wet delays, i.e., those stations in the higher latitude bands or at high altitudes. For example, the NyAlesund station has an RMS of almost 80 percent, while the average zenith wet delay is only 3 cm. Thus the 80 percent RMS of the scale factors indicates an uncertainty of about 2.5 cm. Meanwhile, the station on Ascension Island has an average zenith wet delay of about 18 cm, which means that the 12 percent RMS of the scale factors indicates an uncertainty of about 2.2 cm. So, the wide range in the variability of the scale factors estimates does not necessarily translate into large differences in the magnitudes of the uncertainties in the zenith wet troposphere delays.

Table 3.5: Zenith wet troposphere delay scale factor statistics for 1996

Station	Mean	RMS
Ascension Island	1.07	0.12
Bangalore	1.15	0.18
Greenbelt - 0	1.16	0.68
Greenbelt - 1	0.95	0.53
Hartebeesthoek	1.11	0.25
Kitab	0.68	0.46
Kokee Park	1.10	0.24
LaPlata	1.01	0.25
Maracaibo	1.10	0.13
Matera	1.14	0.27
Neumayer	0.98	1.60
NyAlesund	0.82	0.77
Oberpfaffenhofen	1.01	0.19
O'Higgins	0.93	0.28
Potsdam	0.90	0.66
Shanghai	1.06	0.11
Tahiti	1.07	0.10
Tromsoe	1.10	0.37
UlaanBataar	0.54	0.96

3.2.3 PRARE system time biases

The PRARE system time bias is the same for all the stations, since the measurements are collected and time tagged by the space segment. Errors in the space segment clock will, however, contribute to a PRARE system time bias. To account for this, a time bias is estimated every arc (6 days). This is only possible when the SLR data is simultaneously processed, since the bias is estimated relative to the SLR time. Figure 3.7 shows a plot of the time biases over the two years being investigated; the mean is 4.7 μsec and the standard deviation is 6.5 μsec. The biases become more stable after the first few arcs in 1996, when not as

many stations were operating. The upward jump in early 1997 corresponds to the period when the PRARE unit was switched off from February 14 through February 15 due to an ERS-2 platform anomaly [Flechtner and Teubel, 1997]. When the system was switched on, the PRARE clock had to be resynchronized. This may be the reason for the slightly larger than normal time biases for the following weeks. For the next release of the PRARE data (Version 6), the time biases will be removed.

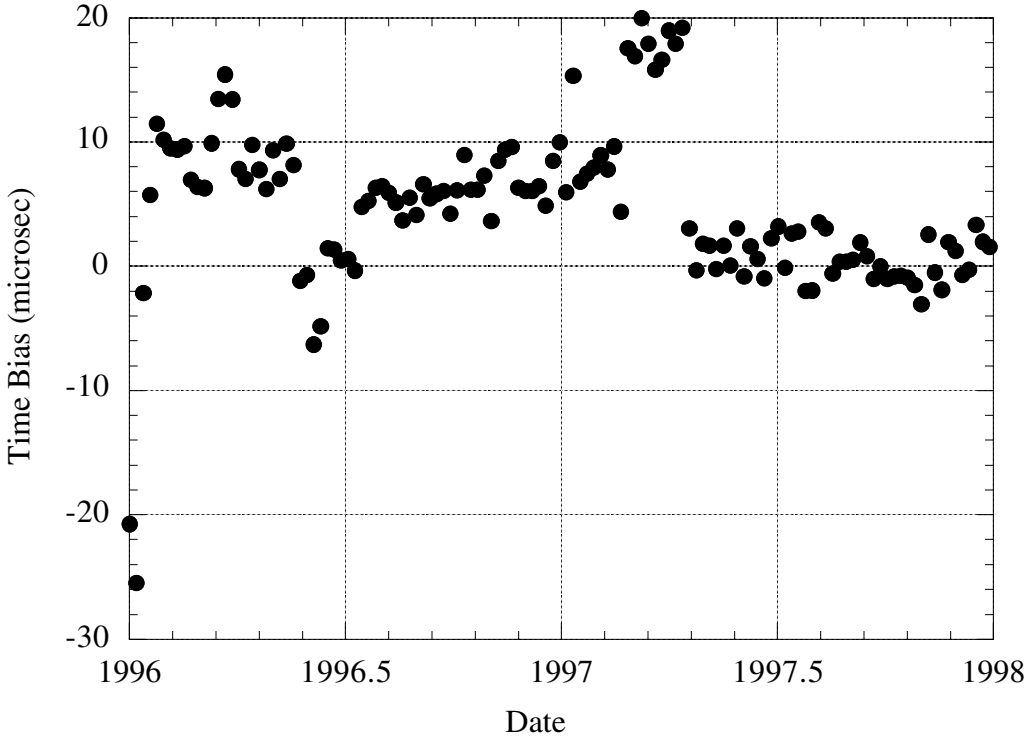

Figure 3.11: PRARE time biases versus time

3.3 ORBIT EVALUATION

It is difficult to evaluate the absolute accuracy of the orbits, since the best measurements of the satellite's position are normally used in the orbit determination process. The use of these measurements to determine the accuracy of the orbits then becomes problematic for two reasons. First, the orbits will tend to fit the data by design, which means that the fits may only be an indication of the level of parameterization of the orbits. In other words, a good fit to inaccurate data does not indicate a good orbit. Second, even when the orbits are parameterized properly, the orbits tend to be most accurate at those times when the satellite is being tracked, while the orbits are more likely to have greater errors when the satellite is over geographical areas without tracking data. Hence, by using the tracking data to evaluate the orbital accuracy, only the most accurate parts of the orbits are being sampled.

In the following sections, orbits computed with different combinations of tracking data are evaluated in several ways. The comparisons between the different orbits shed light on the contributions of the PRARE data and its effectiveness in satellite orbit determination. The 1997 data and orbits are used for the remaining analysis in this chapter, unless specified otherwise.

3.3.1 Tracking data fits

The first way to compare orbit performance is by examining the tracking data fits. Table 3.6 shows the RMS of the residuals (observation minus computed values using the best estimate of the orbit) for six different orbits. The orbits are

computed using different combinations of the available tracking data; the bold type numbers indicate that the data type is given weight in the solution. The top three cases in the table represent the three possible PRARE-only combinations; Doppler-only, range-only, and the combined PRARE range and Doppler case. In general, the residuals which offer the most insight into the accuracy of a particular orbit are the data types which are withheld from that particular solution. For the three PRARE-only cases, the SLR residuals provide an excellent measure of the orbits performance. Similarly, the crossover residuals provide an independent measure of the radial orbit accuracy. The fact that the crossover residuals are all equal to 7.6 cm for the PRARE-only cases indicates that, radially, the orbits are all at about the same level of accuracy. On the other hand, the SLR residuals indicate that, in a three-dimensional sense, the combined PRARE range and Doppler case performs marginally better than either of the individual cases.

Table 3.6: Tracking Data Fits

Data type used in orbit determination	SLR cm	Range cm	Doppler mm/s	Crossovers cm
PRARE range	5.7	**6.0**	---	7.6
PRARE Doppler	5.6	---	**0.39**	7.6
PRARE (both)	5.5	**6.1**	**0.46**	7.6
SLR	**2.7**	12.7	0.80	8.3
SLR + PRARE	**3.7**	**6.2**	**0.46**	7.6
SLR + Crossovers	**3.0**	12.0	0.78	**7.3**

The next case in the table is for the orbits computed using just SLR data. As expected, the SLR residuals decrease, although the PRARE range and Doppler

residuals show a considerable increase. The crossovers also jump from 7.6 to 8.3 cm, which implies an increase of 3.3 cm in the radial orbit error (11.1 cm^2 in variance). This indicates that the PRARE data provides better orbits than those obtained using SLR data alone. This is not due the quality of the SLR data, but rather the quantity, as illustrated in Figures 3.1 and 3.2.

The fifth case is the combined PRARE and SLR case, which represents the orbits that are expected to be the most accurate. The fits for all three data types used in the orbit determination (SLR, PRARE range, and PRARE Doppler) are close to the minimum levels attained when using that specific data type alone. It is noteworthy that the crossovers show no improvement for this case over the PRARE-only cases. This indicates that either the orbits are very similar over the oceans or the crossover RMS is being limited by other signals, such as ocean variability, ocean tide errors, and altimeter measurement errors. This is supported by the last case, where the orbits are computed using both the SLR data and the altimeter crossovers, which are given an a priori uncertainty of 15 cm, as is routine for ERS-1 POD. It is the only one of the orbits in Table 3.6 which gives any weight to the crossovers in the orbit solution. Even with a high weight, the crossover residuals show only a marginal improvement over any of the orbits calculated using the PRARE data. This implies that the crossover fits are getting down to their noise level, and that further reduction of these residuals is unlikely even if the orbits are improved radially. The last case also shows that even when the crossovers are given weight in the solution, the PRARE fits do not show very much improvement over the SLR-only case. This suggests that the addition of the

crossover data does little to improve the orbits, at least over the areas covered by PRARE tracking stations.

3.3.2 Orbit Comparisons

The orbits can be analyzed by comparing orbits directly. This provides insight into the characteristics of the different orbits, although it does not provide information on the absolute accuracy of the orbits. The comparisons are made by differencing the satellite's position in the radial, transverse, and normal directions at every time step that the satellite ephemeris is written. The RMS about the mean of the differences in each of the directions indicate the level of agreement between the two orbits in question. The results are most meaningful if the quality of one of the orbits is known a priori, or at least, which of the orbits is the more accurate.

Considering the orbits in Table 3.6, the most accurate orbit is the SLR and PRARE combined orbit (case 5). This is expected since all of the satellite tracking data goes into the orbit determination. Table 3.7 compares three of the orbits outlined in Table 3.6, the PRARE-only orbit (case 3), the SLR-only orbit (case 4), and the combined SLR and PRARE orbit (case 5).

Table 3.7: RMS of the differences between orbits (cm)

	Radial	Transverse	Normal	3-D
PRARE vs. SLR	2.5	10.8	4.9	12.1
PRARE vs. PRARE + SLR	0.4	5.5	1.7	5.7
SLR vs. PRARE + SLR	2.2	9.2	3.8	10.2

From the top line in Table 3.7, the SLR-only and PRARE-only orbits agree quite well in the radial and cross-track directions. However, in the transverse direction the RMS of the differences is quite a bit larger, at almost 11 cm. The last two rows compare the individual orbits with the combined SLR and PRARE orbits. These two comparisons show that the PRARE data contributes much more in the transverse direction than the SLR data. This implies that the 11 cm transverse difference between the PRARE-only and SLR-only orbits is due mainly to weakness in the SLR-only orbit. Once again, this is really just a function of the superior quantity and distribution of the PRARE data over the SLR data.

Davis Versus Niell troposphere mapping functions

Orbits computed with both the Davis and Niell mapping functions are compared to assess the impact of changing the models. The RMS of the differences in orbits calculated with both PRARE and SLR are 1 mm in the radial, 3 mm in the transverse, and 3 mm in the cross-track directions. As these differences indicate, the troposphere mapping function makes very little difference in the orbits. By estimating pass dependent scale factors, the orbits are insensitive to any differences caused by changing the mapping function.

3.3.3 Orbit Endpoint Analysis

Each of the different cases are also compared internally, by examining the orbit arc endpoints. The differences between orbit arc endpoints provide a reliable

means to assess orbital accuracy. Comparisons at arc endpoints show the consistency of the orbits quite well since the two orbits, computed on either side of the endpoints, do not share any common tracking data. The results from these comparisons are even considered to be a little pessimistic, since generally the orbits are weakest at the endpoints. On the other hand, errors which are common to the two endpoints (such as much of the geographically correlated orbit errors) will cancel, leading to a somewhat optimistic error assessment. As a consequence, these two factors largely compensate for each other and the endpoint tests tend to be reliable indicators of the overall level of orbit error.

Table 3.8: RMS of the differences between orbit arc endpoints (cm)

	Radial	Transverse	Normal
PRARE range	3.4	20.3	8.0
PRARE Doppler	3.4	17.5	9.6
PRARE (both)	3.3	19.5	7.5
SLR	5.2	55.1	10.7
SLR + PRARE	2.7	16.8	5.7
SLR + Crossovers	3.3	49.4	9.7

For this analysis, endpoints between arcs which are separated by burns have been eliminated, since the discontinuities between arcs with orbital maneuvers can be quite large and do not reflect on the overall orbit accuracy. Table 3.8 shows the RMS of the endpoint differences for the 49 arc breaks during 1997 which do not coincide with burns, for the same six cases compared in Table 3.6. From the PRARE-only orbits, both the range and Doppler data seem to

provide about equal strength in the radial direction, but the Doppler data provides more information in the along-track direction and the range data is stronger in the cross-track direction. This comparison again shows the weakness of the SLR-only orbit in the transverse direction. The addition of the crossovers improves the SLR-only orbits significantly in the radial direction, but as expected, does very little in the transverse and normal directions. The combined PRARE and SLR orbit performs the best in all three directions, although the improvements are slight over the PRARE-only orbit.

3.3.4 PRARE-only orbit analysis using high elevation SLR data

For the PRARE-only orbits, a reliable method of determining the radial orbit accuracy is to analyze the SLR residuals from only those passes which attain a maximum elevation of at least 70 degrees. The RMS of the range biases estimated for these high elevation SLR passes gives a good indication of the radial orbit error. This is especially true when the SLR data is withheld from the orbit solution. For the PRARE-only orbit, this analysis indicates that the radial orbit accuracy is approximately 3.0 cm. This result may be a little optimistic, even though the orbits were computed without the SLR data. The majority of the SLR stations are concentrated in Europe and North America, areas which are also covered by some of the PRARE stations. Consequently, the orbit sample evaluated using the SLR residuals is probably a little better than the regions of the orbit which are not covered by any PRARE ground stations.

3.3.5 Crossover Analysis

Radial orbit accuracy can also be estimated by analyzing the altimeter crossover residuals. By constructing an error budget for the crossover residuals, an estimate for the radial orbit error can be resolved. The magnitude of the crossover residuals can be modeled as the root sum square (RSS) of the uncertainties in the constituent error sources.

$$\begin{aligned} xover_{rms}^2 &= \sigma_{non-orbit}^2 + \sigma_{orbit}^2 \\ &= \left(\sigma_{ocean}^2 + \sigma_{tide}^2 + \sigma_{meas}^2\right) + \sigma_{orbit}^2 \end{aligned} \tag{3.6}$$

As shown in the first line, both orbit errors and non-orbit errors contribute to the crossover residual RMS. The gravity model contribution to the orbit term (σ_{orbit}) includes twice the variable part of the geographically correlated radial orbit error, since the variable part has the opposite sign for ascending and descending passes [Rosborough, 1986]. On the other hand, the crossovers contain no mean geographically correlated radial orbit error. Since the amplitude of the mean and variable parts of the orbit error due to gravity model error tend to be roughly equal in magnitude, the orbit error contained in the crossover residuals is approximately equal to the total radial orbit error. In the second line of Equation 3.6 the non-orbit term is further broken down, where σ_{ocean} is the uncertainty due to the ocean variability over the time tag difference between the two altimeter measurements used for each crossover. The σ_{tide} term is the uncertainty due to errors in the ocean tide model, while the σ_{meas} term is the uncertainty caused by

the measurement noise of the crossovers. These are errors that are not static and hence do not cancel out in the crossover.

TOPEX/Poseidon is used to obtain reasonable values for the uncertainties in Equation 3.6. The TOPEX orbits are computed using the same ocean tide model (CSR3.0) as used in this research. The uncertainty in the ocean tide model for TOPEX is estimated to be approximately 2.0 cm [Richard Eanes, personal communication]. Meanwhile, the measurement noise for a crossover is equal to the RSS of the errors in two direct altimeter measurements. The uncertainty of a TOPEX direct altimeter measurement is determined as the RSS of errors due to the instrument noise, EM bias, skewness, troposphere corrections, and ionosphere corrections to be 2.2 cm [Kozel, 1995], resulting in a crossover measurement error of 3.1 cm. Finally, the radial orbit error for TOPEX is estimated to be at the 2.0 cm level. Using these three uncertainties along with the average TOPEX crossover residual RMS of 6.0 cm in Equation 3.6, the ocean variability uncertainty (σ_{ocean}) is deduced to be approximately 4.3 cm.

For ERS-2, the uncertainty in the ocean tides is a little higher because the CSR3.0 ocean tide model is based largely upon TOPEX altimetry. Since TOPEX has an inclination of 66 degrees, the ocean tides for latitudes between ±66 and ±81.5 degrees are not as well determined. Therefore, the estimate of 2.0 cm for the uncertainty in the CSR3.0 ocean tide model for ERS-2 is probably a little optimistic. The crossover measurement noise is also higher for ERS-2, caused in large part, by errors in the ionosphere delay corrections. These larger errors are due to the fact that the ERS-2 altimeter is a single frequency instrument, while the TOPEX altimeter has dual frequencies. Thus, the uncertainty of an ERS-2 direct

altimeter measurement is estimated to be no better than 2.9 cm [Kozel, 1995], making the crossover measurement noise approximately equal to 4.1 cm. Plugging in these uncertainties, along with the σ_{ocean} term obtained from the TOPEX analysis (4.3 cm) and the average RMS of the ERS-2 crossover residuals (7.6 cm), the solution for the radial orbit error (using Equation 3.6) is approximately 4.3 cm. The values used in this computation, for both TOPEX and ERS-2, are summarized in Table 3.9.

The combination of the crossover analysis and the high elevation SLR analysis indicate that the global radial orbit accuracy is at the 3.5 to 4.5 cm level. Chapter 5 will investigate improving this orbit accuracy further through gravity model tuning.

Table 3.9: Crossover Error budget for ERS-2 and TOPEX

TOPEX/Poseidon	Uncertainty (cm)
Ocean variability	4.3
Ocean tides	2.0
Measurement noise	3.1
Radial orbit error	2.0
Average crossover residual RMS	6.0
ERS-2	
Ocean variability	4.3
Ocean tides	2.0
Measurement noise	4.1
Radial orbit error	4.3
Average crossover residual RMS	7.6

Chapter 4

PRARE Station Positioning

The focus of this chapter is the estimation of precise coordinates for the PRARE ground stations. The accuracy of the station solutions is another tool to evaluate the accuracy of the orbits and the quality of the PRARE tracking system. The quality of the station positions rely on the accuracy of the reference orbit used in the solution, while to a lesser degree, the quality of the orbits depends on the accuracy of the station solutions. Unlike SLR stations, the use of ranging to dedicated geodetic satellites (i.e., Lageos-1 and Lageos-2) in order to solve for the station positions is not an option. Because of their size, mass and orbital characteristics these satellites are ideally suited for determining geodetic parameters [Tapley et al., 1993], including station positions. To reduce the effects of hard to model surface forces, these satellites tend to have small area-to-mass ratios and simple, symmetric shapes. Additionally, these satellites are often put in high altitude orbits to lessen the effects of the short wavelength geopotential perturbations and the magnitude of drag forces. Since ERS-2 is large, has a complex shape, and is in a fairly low altitude orbit, the orbits can not be determined as well, which in turn lessens the amount of precise geodetic information that can be obtained from the tracking data. Nevertheless, the PRARE data is used to obtain the best station positions possible.

The first part of the chapter explains the solution procedure used to compute the coordinates. Next, the resulting station coordinates are evaluated by

examining the consistency of the solutions and comparing the results with both externally computed coordinates and survey ties to geodetic markers. The last part of the chapter deals with the treatment of the station located in Neumayer, Antarctica. This station presents a unique opportunity to asses the ability of the PRARE data to observe a moving target. The station is mounted on an ice sheet, which moves with an average velocity of 40 cm per day as the ice flows northward, towards the ocean.

4.1 STATION SOLUTION PROCEDURE

The reference orbits used in the station position solutions are estimated as described in Chapter 3. These orbits are used to generate the observation residuals (observed minus computed) for both the PRARE and SLR data using the UTOPIA software package. The residuals are written without the range biases, time biases, and troposphere scale factors applied to the PRARE data. This is done so that all these parameters can be estimated simultaneously with the station coordinates. The residual files contain the partials of the measurements with respect to the satellite orbit elements, position, and velocity. The ELPSOL software package uses the residual file to solve for the orbit element deviations which provide the best least squares fit to the observations. The resulting orbit element time series can provide information on the types of errors in the force models most responsible for the orbit errors [Watkins, 1990]. This technique allows the identified force model parameters to be added to the list of estimated parameters in an effort to reduce orbit errors. This procedure has proven to be

effective for the Lageos satellites. For ERS-2, the orbit element time series do not show any systematic signals that can be interpreted to indicate weaknesses in the force models. This is partly due to the accuracy of the force models used in the orbit determination procedure. Additionally, the lower altitude ERS-2 orbit is susceptible to higher frequency gravity errors and larger surface forces than the Lageos satellites, making the separation of error sources more difficult. To overcome this, many more dynamic parameters are included in the state vector, which removes some of the signals that this technique is trying to observe.

The ELPSOL software also allows the orbit arc length definition used to compute the reference orbits in UTOPIA to be adjusted. This option provides an easy way to take advantage of the fact that, in general, shorter arc lengths have been found to provide the best station positioning results [Watkins, et al., 1993]. The shorter arcs lessen the effects of long-period and resonant gravity errors, while also preventing the nonconservative surface force model errors from building up. To ensure that the redefined orbit arcs do not span any of the orbit maneuvers, all arcs generated by ELPSOL which contain a burn are automatically rejected from further use.

The station coordinates are estimated using the University of Texas Consider Analysis program (CONAN), which is described in the CONAN users manual introduction [CSR, 1987]. This software package uses the orbit element partials from ELPSOL to estimate corrections to various dynamic, kinematic, and geophysical parameters via a partitioned least squares solution utilizing orthogonal transformations. The program allows the estimated variables to be partitioned into four different subsets, each of which can be estimated at different

frequencies. From least to most frequent, the variables are split into either common, super-arc, arc, or sub-arc categories. To process the PRARE data, CONAN is modified to allow estimation of pass-dependent sub-arc parameters. This option is necessary for the PRARE troposphere scale factors and allows estimation of the sub-arc parameters either on a fixed interval or every pass over a tracking station. The satellite's orbit elements are estimated every arc, and most of the PRARE station range biases are included in the super-arc list. The station coordinates themselves are normally specified as common parameters, so that they are estimated just once over the entire data span being processed. The advantages of using the ELPSOL/CONAN package to estimate the coordinates are that all of the parameters of interest can be adjusted simultaneously and each of the variables can be given an a priori uncertainty about the initial value. Additionally, the necessary computation time required is less than an equivalent UTOPIA run, since the partials are already available and they only need to be mapped to the desired epoch if the arc definition is changed.

If just the PRARE data alone are used, a singularity arises when both the orbit elements and the station coordinates are adjusted simultaneously. Traditionally, this is overcome by fixing the coordinates for one or two stations or by providing a priori constraints on the station coordinates. In this case, the SLR data contributes to the orbit element corrections while the SLR stations themselves are not adjusted, thus anchoring the PRARE coordinate frame to the frame defined by the SLR station coordinates. This eliminates the singularity, without fixing or limiting any of the individual PRARE station coordinates.

4.2 EVALUATING THE STATION SOLUTIONS

Much like evaluating the orbits themselves, analyzing the accuracy of station solutions is very subjective. The true coordinates are unknown, making it difficult to tell how good the solutions really are. Traditionally station coordinates are evaluated by using survey ties from geodetic markers, for which the coordinates are known very precisely. The most useful survey ties are those that are referenced to an SLR station. These are advantageous because there is no need to worry about rotations or offsets between the coordinate systems being used, since the PRARE solutions are constrained to the SLR coordinate frame during the solution process. Unfortunately, these ties are not often available, since most of the PRARE stations are not collocated with SLR stations. In fact, often the stations are purposely put in locations where there is no SLR coverage available, in order to provide better global coverage of the satellite.

4.2.1 Station Solution Repeatability

The lack of trustworthy survey ties, means the station solutions need to be evaluated in other ways. The first method is to look at the repeatability of station solutions made by splitting the two years of data (20, 35-day repeat cycles) into 10 separate spans of 70 days each. The repeatability of these solutions is an indication of the accuracy of the solutions. Since there is no data overlap, each solution is independent of all the others. This analysis does not, however, account for systematic errors which could be biasing all of the solutions in the same way.

Nevertheless, it does provide a method of comparing different solution techniques, in an effort to decide which case is performing most consistently.

To compare the results for all the stations, obtained from different solution strategies, the weighted RMS of each of the coordinate estimates about the weighted mean is examined. Each coordinate estimate is given a weight based on the formal uncertainty of that particular solution. A local topocentric frame is used for this analysis, where the origin of coordinate frame is the PRARE reference point and the fundamental plane is the horizon. This coordinate system is defined so that the X-axis is in the local East direction, the Y-axis is in the local North direction, and the Z-axis points in the vertical direction. The RMS about the mean is calculated in the three coordinates (East, North, and vertical) for every station, and is then averaged across all the stations to give a measure of the repeatability in each of the directions for each solution method. Table 4.1 shows the scatter in the three directions along with the associated magnitude, in order to compare the impact of varying the arc length on the repeatability of the station solutions. The frequency of the range bias estimates applies to all of the stations except Neumayer, Tromsoe, and Syowa. For these stations the biases are always estimated every pass. For all cases, the zenith wet troposphere delay scale factors are estimated every pass. In a three dimensional sense, the 3-day arc length provides the best consistency, although the solution stability is not overly sensitive to the different arc lengths. In light of these results, the 3-day arc length in chosen as the standard from this point on.

Table 4.1: Arc length comparison of station solution repeatability (cm)

Arcs & Biases	East	North	Vertical	3-D
1/2 day	2.0	1.2	1.9	3.0
1 day	1.9	1.2	2.1	3.1
3 day	1.7	1.0	2.0	2.8
6 day	1.8	1.0	2.1	3.0

Table 4.1 implies that the solutions have the most stability in the Northward direction, where the scatter of the solutions is at the 1 cm level. Meanwhile, the repeatability in the Eastward and vertical directions is closer to 2 cm. One explanation for this is that both range and Doppler measurements are strong in the along-track direction, which correlates most closely to the Northward direction in the local topocentric coordinate frame (since the inclination of the satellite is 98.5 degrees). The Doppler data is weak in the cross-track direction, which is closely correlated to the Eastward station coordinate, making the Eastward adjustments mostly dependent on the range data. The range data should provide very strong radial information, which is tied to the vertical station adjustments. However, the need to estimate range biases and troposphere scale factors significantly weakens the certainty of the vertical adjustments.

These conclusions are clearly supported when the repeatability of the solutions is examined for the cases where the range and Doppler data are used in two separate solutions as depicted in Table 4.2. As expected, the main weakness of the Doppler-only solution is in the Eastward direction, while the range-only solution is weakest in the vertical direction. This table also indicates that the best solution is obtained when both the range and Doppler data are used, as expected.

Table 4.2: Station repeatability for different data types (cm)

Case	East	North	Vertical	3-D
Combined	1.7	1.0	2.0	2.8
Doppler	3.8	1.2	1.8	4.3
Range	1.9	1.1	2.7	3.5

Table 4.3 compares how variations in the frequency of both the range biases and the troposphere scale factor estimates impacts the stability of the station solutions. From the table, the best solution is the case where the troposphere scale factors are estimated every pass and the range biases are estimated every arc. When the troposphere scale factors are estimated once per arc, the solution suffers slightly in all three directions. As expected from Table 4.2 above, the station solutions are weakened significantly in the Eastward direction when the biases are estimated every pass, since this, in effect, weakens the range data. Lastly, the case where no troposphere scale factors are estimated is clearly deficient in the vertical direction. From these results, the biases are estimated every 3 days, and the troposphere scale factors are estimated every pass.

Table 4.3: Station solution repeatability for different parameter frequencies (cm)

Arc	Bias	Trop	East	North	Vertical	3-D
3 day	3 day	pass	1.7	1.0	2.0	2.8
	3 day	3 day	1.9	1.1	2.2	3.1
	pass	pass	3.9	1.0	1.8	4.4
	pass	none	3.0	1.0	4.8	5.8

The last comparison to be made using this repeatability test is between solutions made using the two troposphere mapping functions. The two mapping functions, Davis and Niell, were described in Chapter 2. In Chapter 3, it was shown that the orbits are not significantly affected by the choice of mapping function. The station coordinates however, are more sensitive to the mapping function employed. Table 4.4 compares the stability of the solutions, both when no troposphere scale factors are estimated, and when they are estimated every pass. Estimating scale factors tends to minimize the difference between the mapping functions (for both station solutions and orbit determination), so the comparison without scale factors gives a clearer indication of the relative performance. Using different troposphere mapping functions only significantly effects the vertical station adjustments, so these are the numbers that are most relevant in Table 4.4. For both situations, the use of the Niell mapping function performs better than the Davis model, at least in terms of stability of the station solutions. Since the improvement is marginal, both of these cases will be considered further in the following sections to see if changing the troposphere mapping function from the Davis model to the Niell model is warranted.

Table 4.4: Station solution repeatability for different troposphere mapping functions (cm)

Trop. mapping function	East	North	**Vertical**	3-D
Davis without scale factor	1.9	1.1	**4.9**	5.4
Niell without scale factor	1.9	1.0	**4.5**	5.0
Davis with scale factor	1.7	1.0	**2.0**	2.8
Niell with scale factor	1.7	0.9	**1.8**	2.6

4.2.2 Evaluating station solutions with survey ties

The previous section dealt solely with evaluating the station solution techniques by examining the repeatability of 10 solutions, spanning 70 days each. Obviously, this is not an ideal way to determine the accuracy of the solutions. Unfortunately, there is no exact set of true coordinates that we can use to evaluate the various computed solutions. The best we can hope for is a survey tie from a geodetic marker near the PRARE station to the station itself. For a survey tie to be useful, several conditions need to be met. First, the tie itself needs to be very accurate, since often the solutions will differ by only a few mm. Second, both of the reference points that the surveys are taken between need to be known precisely, otherwise the survey is useless. Third, accurate coordinates for the marker that the PRARE station is being surveyed from must be available. Last, the coordinates of the geodetic marker need to be in a known coordinate frame, so they can be rotated into the CSR SLR coordinate frame which is used for the PRARE solutions. Repeatability is an important indication of precision, since one never has an ideal comparison.

Currently, there are only a few survey ties available which meet all the criteria outlined above. The three most reliable ties are referenced to SLR stations at Matera, Greenbelt, and Potsdam. Surveys to SLR stations are ideal not only because the SLR coordinates are very well known, but additionally the PRARE coordinates are constrained to the same coordinate frame. The three survey ties are summarized in the top of Table 4.5, along with three of the less trusted survey ties. Additionally, preliminary ties have been obtained from GFZ [Jean-Claude

Raimondo, personal communication] for the stations at Tahiti, Kitab, Maracaibo, and La Plata. The exact delta's and references for these ties will not be reported, although the analysis will utilize them.

Table 4.5: Survey tie summary (Δ's in m)

PRARE station	Tied from	ΔEast	ΔNorth	ΔVertical
Matera	SLR 7739	-3.78	20.65	-0.67
Greenbelt	SLR 7105	272.08	219.13	-7.52
Potsdam	SLR 1181	-72.17	63.78	6.58
Fairbanks	GPS	70.55	-9.69	5.17
Kokee Park	VLBI	-15.41	-347.98	-4.67
Pasadena	GPS*	-2493529.24	-4655217.36	3565227.53

* GPS survey of PRARE site, XYZ coordinates transformed from ITRF96 to CSR95L01 frame (not tied to anything).

The bottom three ties in Table 4.5 are considered less trustworthy for several reasons. The tie at Fairbanks seems to be fairly reliable, but the station was in operation for less than two months at the end of the two year time span being considered (1996-1997). The tie at Kokee Park is offset by 15 to 20 cm in the vertical direction, probably a result of not correctly knowing the reference points used when the survey was taken. For Pasadena, the coordinates of the PRARE reference point are given in an unknown coordinate frame, which is approximated as ITRF96. Additionally, Pasadena has very poor tracking coverage since the station was installed at the bottom of a hill. The hill significantly obstructs the visibility of ERS-2 as the satellite approaches the horizon. This unbalanced pass geometry increases the correlations between the troposphere

scale factors, the range biases, and the station coordinate adjustments. Therefore, the Pasadena station solutions themselves are rather suspect. As preliminary, the unreported ties at Tahiti, Kitab, Maracaibo, and La Plata are also considered as a part of this less reliable category of surveys. These ties are all reported in either the ITRF94 [Boucher et al., 1996] or ITRF96 coordinate frames, making it necessary to transform the coordinates into the CSR SLR coordinate frame.

Table 4.7 shows the differences between the Matera, Greenbelt, and Potsdam solutions and the corresponding coordinates derived from the three most reliable survey ties. The table compares these differences for solutions computed using Doppler-only, range-only, and both. The table also provides the repeatability statistics for that particular station, in order to validate the repeatability analysis of the previous section. For most cases, the solution with the best agreement with the survey tie also has the lowest variability. For example, the Matera station has the best Eastward agreement with the survey tie for the combined solution at -1.7 cm. Likewise, the combined Matera solution has the lowest repeatability in the Eastward direction at 2.5 cm. The table indicates that the best solutions for the three stations are computed with both data types, which is the same conclusion drawn from Table 4.2, using the repeatability analysis.

Table 4.7: Comparison of differences between station solutions and the survey coordinates along with individual station repeatability statistics (cm)

Station	PRARE Data used	East	North	Vertical	3-D
		Δ's from survey tie (individual station repeatability)			
Matera	Doppler	-5.8 (4.3)	-4.3 (1.3)	-8.2 (2.1)	11.0 (5.0)
	Range	-2.1 (2.6)	-4.0 (1.3)	3.8 (2.6)	5.9 (3.9)
	Combined	-1.7 (2.5)	-4.2 (1.3)	-0.4 (1.7)	4.6 (3.3)
Greenbelt	Doppler	-4.2 (3.2)	-2.5 (1.5)	-5.8 (2.7)	7.6 (4.4)
	Range	2.6 (2.3)	-2.3 (1.0)	1.9 (4.0)	4.0 (4.7)
	Combined	2.7 (2.2)	-2.2 (0.8)	-1.1 (2.6)	3.6 (3.5)
Potsdam	Doppler	-8.8 (4.3)	-5.5 (0.8)	3.4 (1.7)	10.9 (4.7)
	Range	-2.5 (1.2)	-5.7 (1.3)	5.0 (2.4)	8.0 (3.0)
	Combined	-2.3 (1.0)	-5.4 (1.2)	4.5 (2.4)	7.4 (2.9)

In the last section, the Davis and Niell troposphere mapping functions were compared by examining the repeatability of the station solutions computed with each model. Table 4.5 indicated that the Niell mapping function provides better consistency, whether or not troposphere scale factors are estimated for each pass of tracking. Table 4.8 shows the differences between the station solutions computed using the two mapping functions and the surveyed station coordinates. Again, the vertical direction column is the most relevant, since the troposphere mapping function effects this component of the station position estimate the most.

Table 4.8: Differences between station solutions and the survey coordinates computed using the Davis and Niell mapping functions (cm)

Station	Troposphere model	East	North	**Vertical**	3-D
Matera	Davis	-1.7	-4.2	**-0.4**	4.6
	Niell	-1.6	-4.6	**-2.0**	5.3
Greenbelt	Davis	2.7	-2.2	**-1.1**	3.6
	Niell	2.6	-2.5	**-1.3**	3.8
Potsdam	Davis	-2.3	-5.4	**4.5**	7.4
	Niell	-2.4	-5.6	**2.5**	6.6
Fairbanks	Davis	0.3	-5.1	**-2.8**	5.9
	Niell	0.2	-5.2	**0.0**	5.2
Kokee Park	Davis	4.3	0.0	**20.3**	20.7
	Niell	2.1	0.0	**20.0**	20.1
Tahiti	Davis	0.0	1.2	**6.2**	6.1
	Niell	0.0	1.0	**-2.2**	2.4
Pasadena	Davis	6.9	-5.1	**4.3**	9.6
	Niell	6.9	-5.3	**2.3**	9.0
Kitab	Davis	-2.6	-2.6	**-4.9**	6.1
	Niell	-2.6	-2.7	**-4.8**	6.1
Maracaibo	Davis	1.1	-4.4	**2.2**	5.0
	Niell	0.6	-4.9	**-7.5**	8.7
La Plata	Davis	2.2	-0.6	**-0.3**	2.3
	Niell	2.2	-0.9	**0.4**	2.4

The Davis model provides better agreement for Matera and Maracaibo, while the Niell model compares better for Potsdam, Fairbanks, Tahiti, and Pasadena. The differences for Greenbelt, Kokee Park, Kitab, and La Plata are too small to tell which model is performing better. For most stations, the difference between the solutions computed using the different mapping functions is less than 2 cm in the vertical direction, and from Table 4.6, the repeatability of the solutions in the vertical direction is 2.0 cm. Therefore, the differences between the two mapping functions are within the approximate noise level of the solutions. It should be noted that the Niell mapping function has been found to be more

accurate by Stovers and Lanyi [1994] and Estefan and Stovers [1994], and thus the station solutions computed using this function are, at the very least, no less reliable than those obtained using the Davis mapping function. Since the Niell mapping function does seem to be slightly outperforming the Davis model, the Niell mapping function is used to compute the CSR PRARE coordinates.

From Table 4.8, a negative Northward bias is evident in the station solutions for all the stations, except Kokee Park and Tahiti. This is somewhat surprising because the accuracy inferred from the solution repeatability is strongest in the Northward direction. This shows the inherent weakness in basing the accuracy of the station coordinates solely on the consistency of the solutions. For most of the stations, a Northward bias is similar to a Z-shift, which can easily be caused by once per revolution signals in the data. These kinds of signals could be caused by errors in the once-per-revolution parameters estimated in UTOPIA, which are used to remove errors in radiation forces and gravity field model errors. To see if the Northward bias is in fact a Z-shift, the information from Table 4.8 is repeated in Table 4.9 in terms of the body fixed, XYZ coordinate frame. When looked at this way, the biases are not quite as apparent in the solutions. Discounting Kokee Park, the Davis Potsdam solution, and the Niell Tahiti solution, all the differences in the Z direction are less than zero.

Once again, the limited number of high quality survey ties makes it hard to determine with confidence the amount, if at all, the PRARE coordinates should be shifted in the Z-direction. This, and the fact that the observed errors in the Z-direction are not much more than the errors in either the X or Y-directions, lead to the decision not to offset the whole PRARE solution to accommodate the

observed Z-shift. Also, the objective of this research is to show the best results that can be obtained using the PRARE data, while artificially forcing the coordinates to match the survey ties does not demonstrate the capacity of the PRARE data. Additionally, the station coordinates are dependent on the gravity field used in calculating the orbits. As an example, the Northward comparison for the Greenbelt station changes from -2.2 cm to +3.3 cm when the JGM-3 gravity field is used, rather than TEG-3.

Table 4.9: Differences between station solutions and the survey coordinates in body fixed, XYZ coordinates (cm)

Station	Troposphere model	X	Y	Z	3-D
Matera	Davis	2.8	-0.9	-3.5	4.6
	Niell	1.9	-1.1	-4.8	5.3
Greenbelt	Davis	2.7	0.1	-2.4	3.6
	Niell	2.6	0.0	-2.8	3.8
Potsdam	Davis	7.4	-0.7	0.2	7.4
	Niell	6.3	-1.0	-1.4	6.6
Fairbanks	Davis	-2.8	-2.1	-4.7	5.9
	Niell	-3.8	-2.7	-2.2	5.2
Tahiti	Davis	-5.3	-3.1	-0.6	6.1
	Niell	1.6	0.9	1.6	2.4
Pasadena	Davis	3.0	-8.9	-1.8	9.6
	Niell	3.8	-7.6	-3.1	9.0
Kitab	Davis	1.6	-3.0	-5.1	6.1
	Niell	1.6	-2.9	-5.2	6.1
Maracaibo	Davis	2.0	-2.4	-3.9	5.0
	Niell	-1.5	6.4	-5.8	8.7
La Plata	Davis	1.6	1.7	-0.3	2.3
	Niell	1.8	1.3	-0.9	2.4

4.2.3 System transformation parameters and coordinate frame stability

A common way of comparing two networks of station solutions is by performing a Helmert transformation between the sets of coordinates [Boucher et al., 1998]. The 7-parameter transformation entails estimating 3 translation parameters, 3 small rotations, and a scale factor, which minimize the differences between the two sets of coordinates. The resulting transformation removes any systematic differences between the two coordinate frames defined by the station solutions. The transformation between the 15 common stations in a solution spanning 1996 and one spanning 1997 results in the parameters shown in Table 4.10.

Table 4.10: Transformation between 1996 and 1997 solutions

	X	Y	Z
Translation (cm)	-0.3	0.6	1.6
Rotation (mas)	0.1	0.1	0.0
Scale (ppb)	-1.2		

In reality, this is another measure of the repeatability of the station solutions. The small values for the parameters again indicate how consistent the solutions are. The scale factor of 1.2 parts per billion amounts to a difference of 7.6 mm. The procedure indicates that the most variation occurs in the Z-direction, which is not surprising, in light of the apparent Z-shift seen when comparing the coordinates to the survey ties.

The stability of the coordinate frame defined by the estimated coordinates can be determined by making a Helmert transformation between the PRARE solution and the surveyed coordinates. This tests how well the SLR data is constraining the PRARE reference frame. However, the limiting factor is once again the number of quality survey ties. The Kokee Park tie cannot be used for this analysis, since the large error in height would skew the statistics. That leaves nine surveys, of which only two are in the Southern hemisphere (Tahiti and La Plata). Without more Southern surveys, the translation parameters are highly correlated with the scale factor. Keeping this in mind, the parameters are given in Table 4.11 for both the Davis and Niell solutions versus the survey coordinates.

Table 4.11: Transformation between the PRARE solution and the SLR coordinate frame defined by the survey coordinates.

Davis	X	Y	Z
Translation (cm)	0.2	-1.7	-2.6
Rotation (mas)	-0.1	-0.6	-0.4
Scale (ppb)	2.0		
Niell			
Translation (cm)	0.7	-0.5	-1.7
Rotation (mas)	-0.5	-0.6	-0.3
Scale (ppb)	-1.6		

For both cases, the rotations are very small and indicate that the PRARE coordinates are being sufficiently constrained by the presence of the SLR data in the solution process. Even the translations and scale factors are small, although these values cannot really be trusted based on the inadequate amount of coverage provided by the surveyed coordinates. Again, the Niell solution agrees slightly

better with the survey coordinates, although the most significant differences are not in the rotations, which are the most reliable parameters in Table 4.11.

4.2.4 Comparison to externally computed coordinates

PRARE station solutions were obtained from both the Delft University of Technology (DUT) in The Netherlands [Pieter Visser, personal communication] and GFZ Potsdam [Jean-Claude Raimondo, personal communication]. These solutions cover roughly the same time span as the CSR solution and provide an additional means of evaluating the CSR solution.

Delft Comparison

The 7-parameter fit between the CSR and DUT solutions is based on 19 common stations, and yields the transformation outlined in the following table.

Table 4.12: Transformation between CSR and DUT solutions

	X	Y	Z
Translation (cm)	1.6	-3.0	-0.9
Rotation (mas)	-0.7	-1.8	-0.5
Scale (ppb)	3.4		

This transformation represents the systematic differences between the two sets of coordinates. These differences can be caused by using different SLR coordinates, different polar motion models, and different gravity field models. When these systematic differences are removed the resulting comparisons show the relative agreement between the two sets of coordinates. Table 4.13 displays

the RMS of the differences between all the station coordinates, before and after application of the Helmert transformation shown in Table 4.12. The agreement between the two sets of coordinates after removal of systematic errors is at the 2 to 3 cm level in each direction.

Table 4.13: RMS of the differences between CSR and DUT solutions (cm)

	ΔX	ΔY	ΔZ	3-D
Before Transformation	4.9	5.3	4.8	8.7
After Transformation	2.0	2.7	3.1	4.6

GFZ Potsdam Comparison

The 7-parameter fit between the CSR and GFZ solutions is based on 23 common stations, and yields the parameters shown in Table 4.14. The overall magnitude of this transformation is slightly larger than obtained in the DUT comparison, especially in scale.

Table 4.14: Transformation between CSR and DUT solutions

	X	Y	Z
Translation (cm)	-2.9	-0.6	-1.6
Rotation (mas)	-2.8	-1.8	-0.9
Scale (ppb)	-7.6		

The RMS of the differences between all the station coordinates, before and after, application of the Helmert transformation are given below, in Table 4.15.

The agreement between these two sets of coordinates after removal of systematic errors is at the 5 to 6 cm level in each direction.

Table 4.15: RMS of the differences between CSR and GFZ solutions (cm)

	ΔX	ΔY	ΔZ	3-D
Before Transformation	6.3	8.1	9.7	14.1
After Transformation	6.0	4.8	4.8	9.1

Survey tie analysis

The CSR solution compares more favorably to the survey ties than either of the external solutions. This is not really a fair comparison however, since the survey tie coordinates used are all in the CSR SLR coordinate frame, which was shown in the previous section to be almost the same as that defined by the CSR PRARE solution. Meanwhile, the external coordinates are not constrained to the same SLR coordinate system, as is witnessed by the significant Helmert parameters between the CSR and DUT/GFZ solutions. Nevertheless, large scale or translation differences are probably more an indication of real systematic solution differences than reference frame inconsistencies.

4.2.5 Station Solution Accuracy

The previous sections described methods of evaluating station solutions, first by examining solution repeatability, then by survey tie comparisons, and then by external solution comparisons. All of the methods have their shortcomings. Repeatability does not account for systematic errors, or biases, in the solutions.

Reliable survey tie analysis is subject to uncertainties in the ties, errors in the coordinates used for the reference markers, and the quantity of ties available. Comparison to externally computed solutions is dependent on the quality of the external solutions, which in this case are not really known.

The accuracy of the estimated station coordinates are not realistically represented by the formal uncertainties obtained during the solution process. For the two year solution the computed sigmas are usually less than 1/2 cm in each coordinate. The repeatability and survey tie analysis clearly indicates that the uncertainties of the station coordinates is at a higher level. The uncertainty of the solutions obtained from the repeatability statistics alone is also optimistic, since it does not account for systematic errors. To compensate for this, a more realistic estimate of the uncertainty for each solution is made by taking the root sum square (RSS) of the errors indicated by repeatability and the translations from the 7-parameter fit between the PRARE and survey solutions (from Table 4.10: ΔX of 0.7 cm, ΔY of 0.5 cm, and ΔZ of 1.7 cm). In effect, this will increase the sigmas in the Z-direction for each of the station solutions to account for some of the Z-shift seen in the survey tie comparisons. Table 4.16 presents the PRARE solution made using the Niell map**ping f**unction, since it seems to perform marginally better in all of the tests.

Table 4.16: Station coordinates and uncertainties (epoch 1997.0)

Station	ID	X (m)	σ cm	Y (m)	σ cm	Z (m)	σ cm
Tromsoe	7702	2102933.87	1.3	721613.72	1.8	5958195.26	1.8
Matera	7704	4641952.56	2.3	1393062.47	2.2	4133277.64	1.9
Hofn	7707	2679699.24	0.9	-727960.39	0.5	5722783.40	2.0
Fairbanks	7708	-2281592.73	2.1	-1453661.13	2.1	5756962.54	2.6
Tahiti	7709	-5246589.00	1.5	-3076956.67	1.9	-1913779.98	1.9
O'Higgins	7710	1525864.93	1.6	-2432477.83	2.2	-5676149.88	3.1
Syowa	7711	1766500.45	1.2	1460251.18	1.5	-5932214.37	2.0
Hartebeest.	7714	5084836.73	1.4	2670355.50	1.6	-2768104.71	1.9
LaPlata	7715	2780104.38	1.8	-4437421.11	1.1	-3629399.08	2.0
Maracaibo	7716	1976112.68	1.5	-5948897.95	1.4	1173586.33	1.8
Ascension	7717	6119375.06	2.5	-1571451.73	1.7	-871686.71	2.1
Bogor	7719	-1821137.84	2.1	6069822.12	2.1	-721148.58	2.6
UlaanBataar	7720	-1257396.49	2.3	4099417.24	1.7	4707988.89	2.9
Kitab	7721	1944950.73	3.8	4556652.90	1.7	4004323.48	2.0
Greenbelt	7722	1130951.73	2.1	-4831148.52	1.7	3994272.11	2.1
Kokee Park	7724	-5543970.08	1.3	-2054593.08	1.3	2387489.95	1.8
Bangalore	7725	1344099.46	1.8	6068608.92	1.4	1429291.39	1.8
NyAlesund	7728	1202421.64	1.7	252627.11	1.8	6237774.65	2.9
Potsdam	7730	3800592.20	1.0	881924.67	1.2	5028903.88	2.3
Shanghai	7734	-2831710.05	1.3	4675682.66	1.2	3275359.69	2.0
Oberpf'hofen	7736	4186558.94	1.5	835022.43	1.0	4723761.20	2.1
Greenbelt	7755	1130778.01	1.3	-4831241.63	1.2	3994212.06	2.2
Pasadena	7758	-2493529.37	1.7	-4655217.21	1.0	3565227.60	2.0

4.3 THE NEUMAYER STATION

The PRARE station installed in Neumayer, Antarctica presents a unique opportunity. The Neumayer research station is located on the Ekström ice shelf, which flows in the Northward direction at a rate of about 40 cm per day. Additionally, since the ice shelf is floating, the station moves with the ocean tides. The station is outside the hinge zone of 1 to 10 km [Vaughan, 1995], which

means the ice is floating freely on the ocean. This means the motion caused by the tides should be in the vertical direction alone. In fact, the vertical displacement caused by the tides should be the same as would be expected at this location if there was no ice sheet present. Without special treatment, the data from the Neumayer station must be given virtually no weight in the orbit determination process, since the position of the station will not be modeled correctly. If the position and motion of the station can be determined with confidence, then the data can be given some weight in the orbit determination procedure. This is significant because the station provides a very large amount of data from a geographical area that is not covered by SLR at all. The station provides so much data because the nearly polar orbit of ERS-2 results in the satellite being visible from high elevation stations for a large percentage of the revolutions of the satellite. Additionally, the Neumayer station has been one of the best performing stations; it has tracked consistently, without major problems, over the entire two year span being investigated.

Obviously, the Neumayer station position cannot be estimated using the same parameterization as the other stations. The strategy is to estimate a linear velocity to account for the ice flow, although this assumption may not be entirely accurate, since seasonal variations in the ice sheet velocity seem possible. To recover the linear velocity, the Eastward and Northward station positions are estimated once per three-day arc, while the vertical position is estimated for every satellite pass. Similar to the handling of the other stations, the troposphere scale factors are estimated every pass, while the range biases are estimated once per arc. Figure 4.1 shows the results over the two year span; in the East and North

directions the station position varies at a constant rate of -6.4 and 41.1 cm/day, respectively. In the vertical direction, the motion is less consistent, due both to the tidal motion of the station and the increased noise in the estimates caused by increasing the frequency of the estimates to every pass. The discontinuity, which is most visible in the upward direction, is a result of the station being elevated by about 1 m in early 1997. The station was raised to counter the sinking into the ice that had occurred up to that point. To account for the relocation, a discontinuity in the position and linear velocity is allowed in all three directions.

The position changes due to the linear velocities are removed from the estimated positions, resulting in the time series shown in Figure 4.2. The most distinct feature of these time series is that both the East and North plots show significant signals not accounted for by linear velocities alone. Both plots show short period signals of about 14 days which may be caused by aliasing of the vertical tidal variations into the horizontal station positions. Additionally, the two plots have longer period signals which could be caused by aliasing of the long period vertical motion of the station, or could be a result of real periodic horizontal movement of the ice sheet. The bottom plot, which shows the residuals in the vertical direction, has a much greater magnitude than either of the other directions. The large amount of data compressed along the horizontal axis prevents the signals from being clearly visible, but closer inspection reveals diurnal, semidiurnal, and 14 day period tidal signals in the time series.

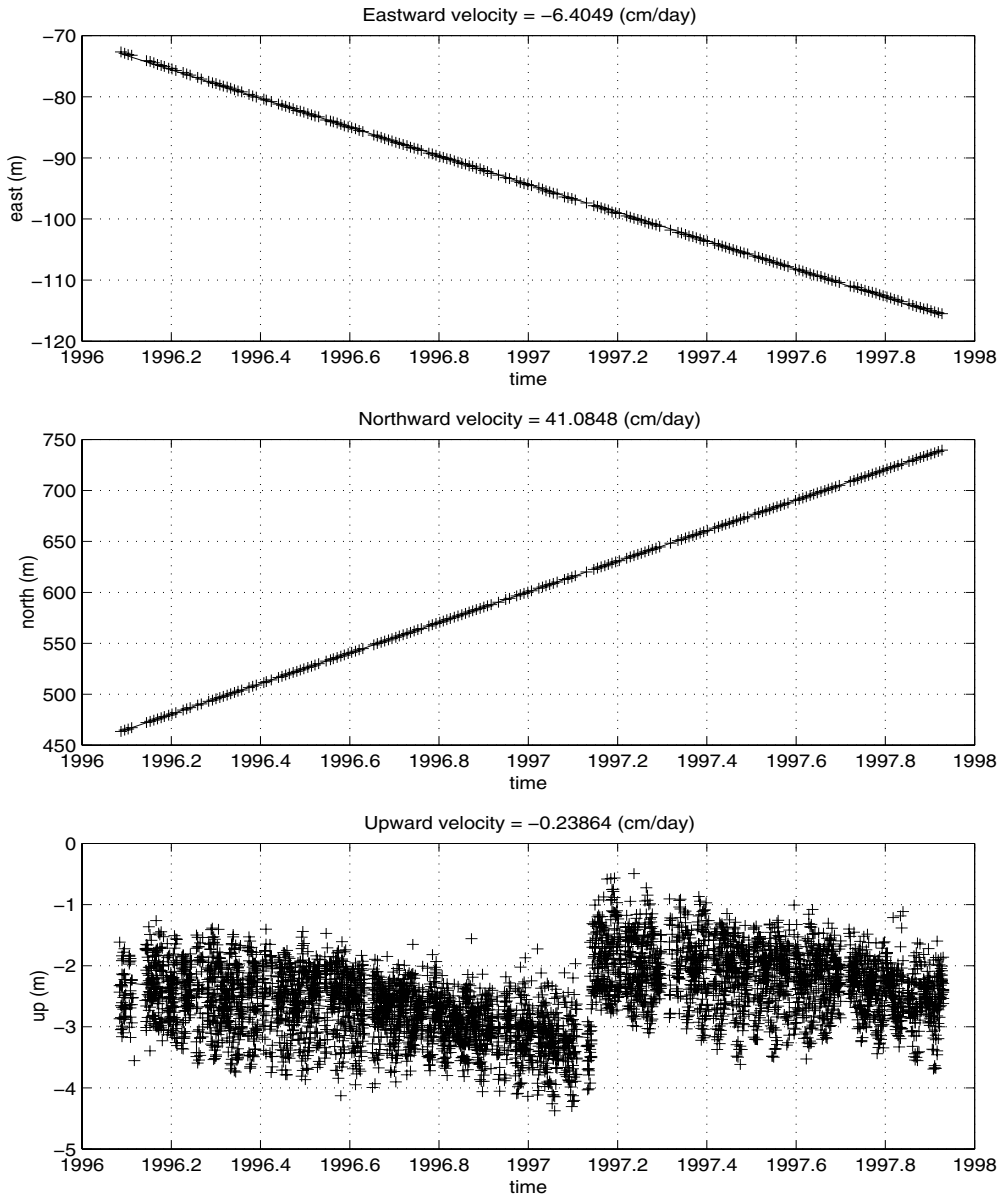

Figure 4.1: Estimates of the Neumayer station position (every 3 days in East and North, every pass in vertical)

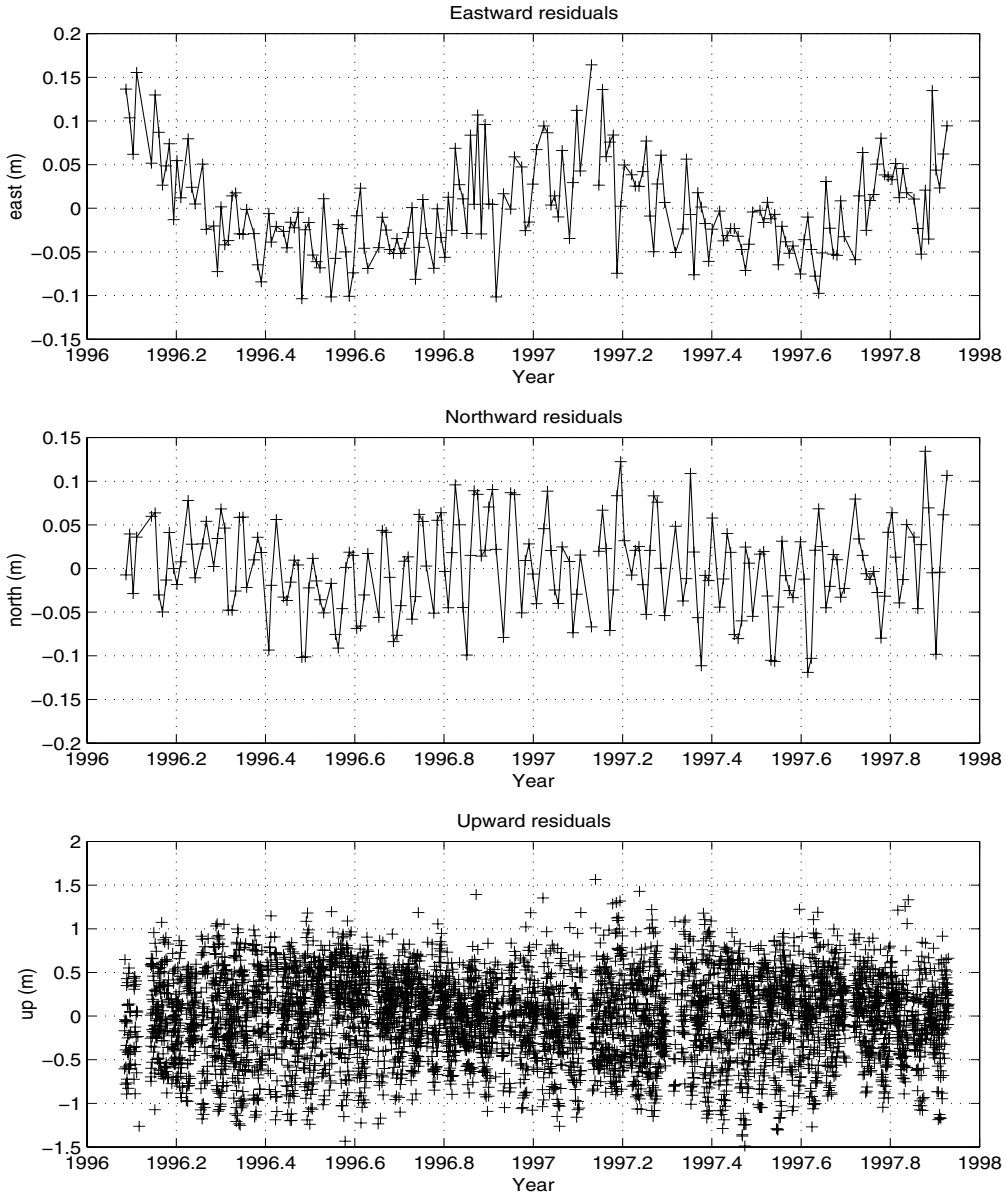

Figure 4.2: Residuals of the Neumayer position estimates after removal of the linear velocities depicted in Figure 4.1

4.3.1 Estimation of Ocean Tides at Neumayer

The vertical station position time series, after removal of the linear 87.2 cm/year downward velocity, is used to estimate the ocean tides using the response method [Munk and Cartwright, 1966] in terms of the orthotide functions of Groves and Reynolds [1975]. A concise description of this method of describing the ocean tide as a sum of orthogonal functions representing the real and imaginary parts of the time-dependent tide generating potential and the corresponding orthogonal response weights is given in Cartwright and Ray [1990].

The vertical residuals are shown before and after estimating the tides, in Figure 4.3. The top panel shows the residuals over a representative 20 day period, just to make the tidal signals more apparent. Keep in mind however, that the tides were estimated using the entire two year time series depicted in the bottom panel of Figure 4.2. The second panel in Figure 4.3 displays the power spectral density of the two year time series, which clearly shows that the station position estimates are picking up the tidal signals. The bottom panel shows the residuals after estimation of the 18 parameters used to describe the long period, diurnal, and semidiurnal tides. Removal of the observed tides results in a decrease in the RMS of the complete two year time series from 47.5 cm to 22.2 cm. The power spectral density of the residuals, after removal of the estimated tides, reveals that most of the semidiurnal and 14 day period tidal signals have been removed. However, a small amount of the diurnal signal remains in these adjusted residuals.

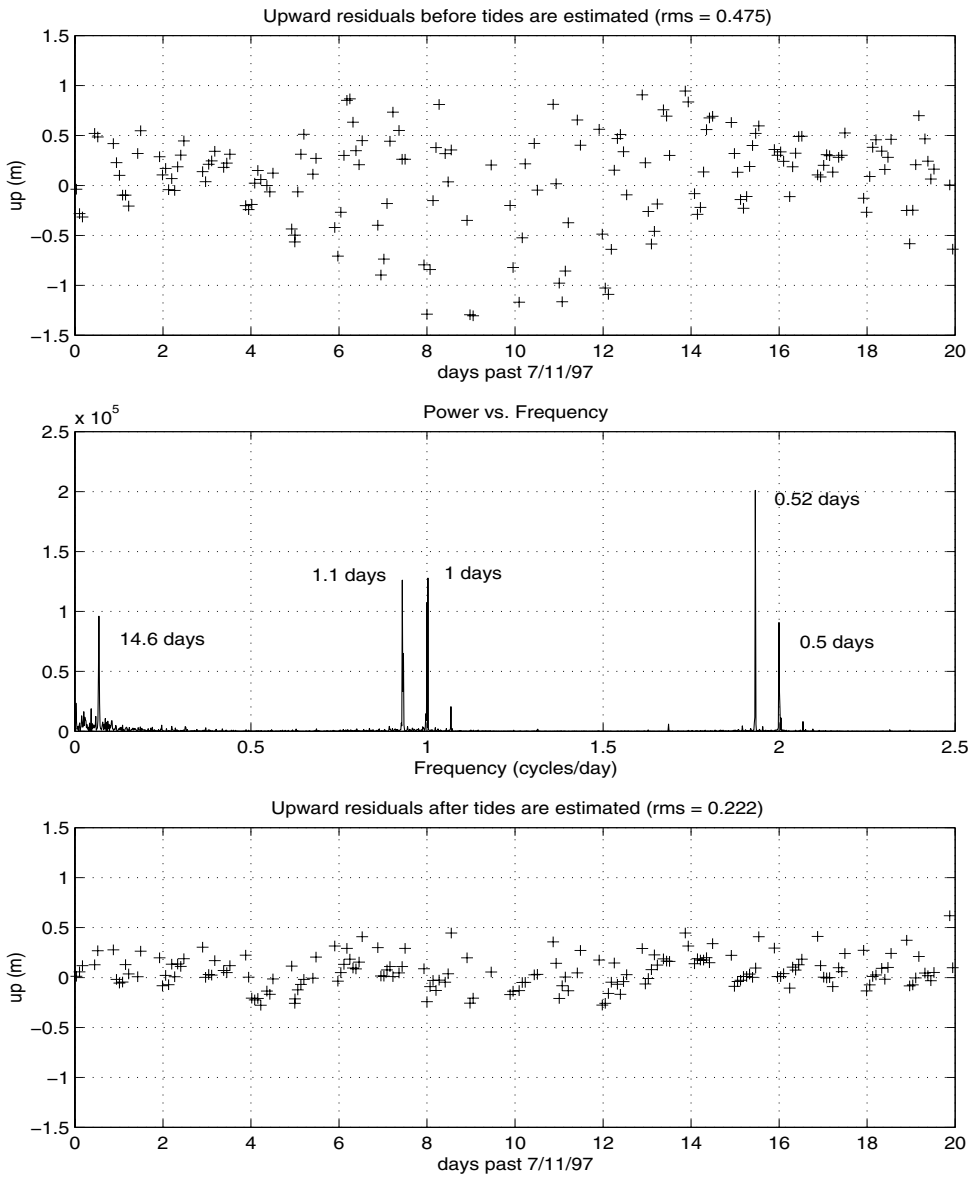

Figure 4.3: Top: Estimates of the periodic vertical motion of the Neumayer station, Middle: Power spectral density of the full vertical position time series, Bottom: The vertical residuals after removal of the estimated tides.

4.3.2 Evaluation of Estimated Tides

The Neumayer tides estimated from the observed vertical motion of the station are evaluated by comparing the results to the CSR3.0 tide model. It should be mentioned that the CSR3.0 tide model is heavily dependent on TOPEX/Poseidon altimetry and therefore loses accuracy above latitudes of ±66 degrees, and that Neumayer has a latitude of -70.7 degrees. In fact, the CSR3.0 tide model reduces to the hydrodynamic model of Le Provost et al. [1994] at latitudes higher than ±66 degrees. Nevertheless, a rough assessment of the estimated tide model can be made by comparing the two. Table 4.17 compares the amplitudes and phase lags for 22 of the larger tidal constituents at this location. The table indicates that the estimated tides are approximately correct, but a better way to compare the results is by examining the resulting displacements predicted by each tide model.

It is interesting to note that the aliasing of tidal signals that normally takes place when using altimetry from the ERS satellites is diminished, since the sampling is not restricted to the ground track repeat period. The Sun-synchronous orbits of the ERS satellites make the S_2 tide, which has a period of 12 hours, unobservable through the use of altimetry [Parke et al., 1987]. In this case, the PRARE data provide 5 to 10 vertical position estimates per day, thus eliminating the sampling problems associated with altimetry from ERS-2 alone. This is evident in how close the estimate for the S_2 tide from the PRARE data is to the value from the CSR3.0 model.

Table 4.17: Comparison of amplitudes and phase lags

Constituent		CSR 3.0		From Estimates	
		Amp. (mm)	Lag (deg.)	Amp. (mm)	Lag (deg.)
2Q1	125.755	10.46	342.26	7.78	351.23
Q1	135.655	62.85	341.50	59.42	349.25
O1	145.555	254.80	343.23	283.42	347.70
M1	155.655	16.58	348.97	18.27	346.59
P1	163.555	96.42	355.51	83.48	346.29
S1	164.555	2.31	356.04	1.93	346.31
K1	165.556	295.18	356.56	238.53	346.34
PHI1	167.555	4.31	357.53	3.23	346.43
J1	175.455	19.62	1.08	8.39	348.33
OO1	185.555	13.83	1.42	2.47	358.02
NU1	195.455	3.41	359.48	0.31	22.62
EPS2	227.655	2.78	185.70	1.92	173.82
2N2	235.755	9.46	177.65	7.46	171.26
MU2	237.555	11.47	177.18	9.18	171.74
N2	245.655	75.71	179.27	65.51	178.88
NU2	247.455	14.55	180.30	12.71	180.47
M2	255.555	442.48	190.24	403.83	192.22
L2	265.455	15.08	204.26	13.80	205.89
T2	272.556	17.19	213.75	15.29	214.91
S2	273.555	298.52	214.53	264.54	215.66
K2	275.555	83.84	216.02	73.73	217.13
ETA2	285.455	5.66	223.77	4.71	225.13

The tidal heights predicted by both the CSR3.0 tide model and the local, Neumayer tide model over a two day period are shown in Figure 4.4. The RMS of the differences between these two time series is 6.2 cm. From the figure, it appears that the ice sheet causes some damping of the tidal motion, resulting in smaller amplitudes, especially at the peaks. It is difficult to infer too much from this comparison, since the quality of the CSR3.0 tides are questionable at this

location, but it is comforting that the level of agreement between the two independent tide models is as good as it is.

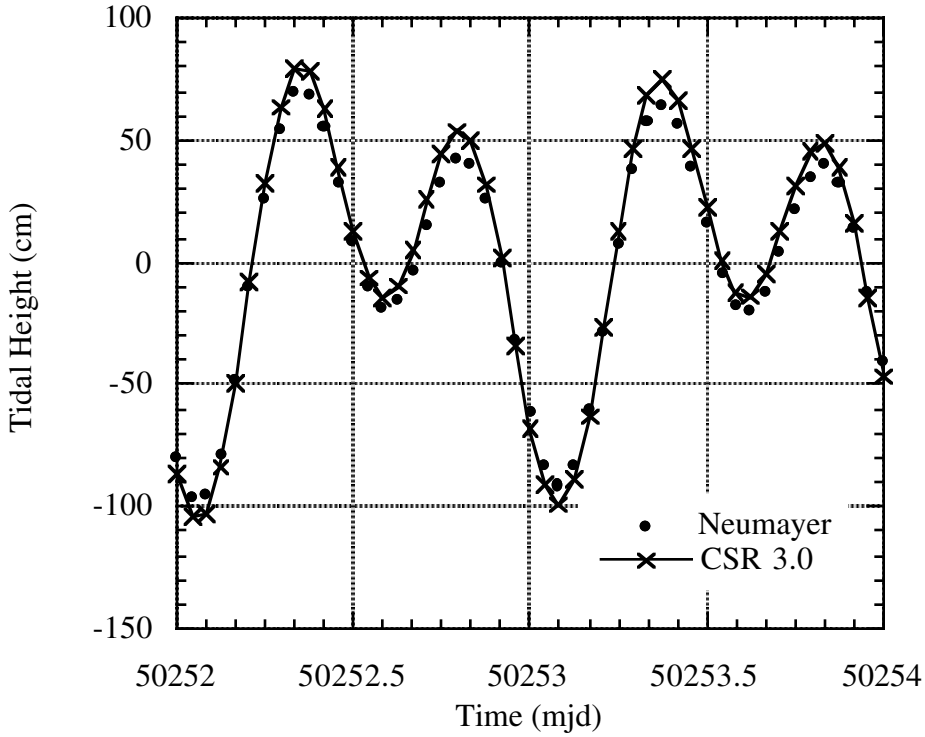

Figure 4.4: Predicted heights from the CSR 3.0 tide model and the Neumayer, site specific tide model

In reality, the motive for solving for the local Neumayer tides is to allow the periodic vertical motion of the station to be accounted for in the orbit determination process. If these tidal variations are not used to correct the PRARE station position in UTOPIA, they can be aliased into the orbit. To prevent this from happening, the data from Neumayer was assigned a very high a priori uncertainty, so the station made virtually no contribution to the orbits. When the local tide model and the estimated linear ice sheet velocities are both used to

determine the position of the station at every observation time, the data may be assigned a higher weight in UTOPIA.

4.3.3 Evaluating the Neumayer Data

To determine the amount of weight to give the Neumayer PRARE data in the orbit determination process, the first thing to examine are the fits of the data to the orbits. The RMS of the residuals for the Neumayer data are presented in Table 4.18. For all cases, the Neumayer range biases are estimated every arc. As expected, there is a dramatic improvement in the fits when the ocean tides are accounted for, even when the data is not given any weight in the solution.

Table 4.18: Neumayer data fits (cm, mm/s)

tide model applied	a priori sigma	Range	Doppler	SLR
no	∞	12.3	1.04	3.8
yes	∞	7.9	0.57	3.8
yes	50	7.7	0.55	3.8
yes	20	6.9	0.51	4.0

The fits improve marginally as the data is given more weight, but care must be taken to ensure that the station is not given so much weight that the orbit starts to degrade. In going from zero weight to an a priori uncertainty of 50 cm, the SLR and crossover fits remain virtually unchanged. In dropping the a priori uncertainty from 50 to 20 cm (the same weight assigned to the other PRARE stations), the SLR fits increase slightly. In light of this, and since there still remains more uncertainty in the position of this station as compared to other

PRARE stations, the Neumayer station is assigned an a priori sigma of 50 cm. This allows the data to make a significant contribution to the orbits only when the amount of tracking data available from other stations is less than normal, while it will not impact the orbits when there is adequate tracking data from the other sites.

Chapter 5

Gravity Field Analysis and Tuning

The geographic distribution and density of the PRARE tracking data make it a candidate for use in improving gravity field models. The fairly low altitude and high inclination of ERS-2 make it sensitive to some of the shorter wavelength gravity field perturbations. This, in combination with the precision of the PRARE observations, make it feasible to use the PRARE data set to improve the current gravity models.

The gravity field model used throughout this research is the most recent in the Texas Earth Gravitational Model series, TEG-3 [Tapley et al., 1997]. This model is complete through harmonic degree and order 70, and includes satellite tracking from Spot 2 (DORIS), Stella (SLR), and ERS-1 (SLR and altimetry). These satellites are all in Sun-synchronous orbits very similar to that of ERS-2, which results in the TEG-3 field already being somewhat tuned for ERS-2 POD. The other gravity model to be analyzed in this chapter is the Joint Gravity Model 3, referred to as JGM-3 [Tapley et al., 1996]. This model utilizes the same Spot 2 data that was used in TEG-3, but does not contain any tracking from ERS-1 and much less Stella tracking than used in generating TEG-3. This means that the PRARE data will have a larger impact on the JGM-3 model than the TEG-3 model. As an aside, the ERS-1 SLR and altimetry in TEG-3 should probably be replaced with similar data from ERS-2, since it has more accurate orbits and some of the altimeter corrections have been improved since the TEG-3 model was

created. Additionally, ERS-2 orbits are not corrupted by the aliasing of oceanographic signals, since the orbits are produced without altimetry. However the emphasis of this research is to show the impact of the PRARE data in tuning current gravity models, so the efforts herein will consist of adding new data to the information already in the existing models. It should also be noted that the JGM-3 gravity field model is used to compute the CSR TOPEX/Poseidon orbits rather than TEG-3, since the JGM-3 field appears to slightly outperform TEG-3 for TOPEX/Poseidon POD [Ries, personal communication].

The first section of this chapter briefly discusses the methods used to tune the gravity field models. The next section compares the TEG-3 and JGM-3 gravity fields in terms of ERS-2 orbit determination. Finally, the impact of the tuning efforts will be examined in terms of data fits, predicted geographically correlated orbit uncertainties, orbit differences, orbit endpoint consistency, and sea surface topographies.

5.1 GRAVITY TUNING METHODS

Current gravity field models are created by combining surface gravity measurements, satellite tracking, and satellite altimetry. All of these data types are sensitive to different geopotential parameters and provide different levels of geographical coverage. For satellite data, the sensitivity of the orbits to the geopotential depends on the altitude, inclination, and eccentricity of the satellite. The lower the satellite, the more sensitive it is to shorter wavelength parts of the gravity field. The amount of global coverage provided by the satellite is

dependent on the inclination of the satellite, while the locations of the tracking stations determines the geographic locations that the tracking data will be able to contribute to the geopotential model. The JGM-3 gravity model contains information from 34 satellites, with a wide spectrum of different inclinations and altitudes [Tapley et al., 1996; Nerem et al., 1994]. Meanwhile, the TEG-3 model contains tracking data from 18 different satellites along with altimetry from TOPEX/Poseidon and ERS-1. Although there are a large number of satellites contributing to these models, many of them provide very little information due to inaccurate or sparse tracking data. Additionally, the large amount of high accuracy TOPEX/Poseidon tracking data (SLR, DORIS, and GPS) and altimetry in the solutions tend to make the gravity fields perform the best for satellites in similar orbits to TOPEX, or satellites with high altitudes. As will be shown in the next section, both models need improvement for satellites in orbits similar to ERS-2.

Following Kaula [1966], the orbit perturbations due to the geopotential are classified in four basic frequency bands. The first type are secular variations of the orbit elements, which are due to the even parity zonal harmonics. The second type are long period and resonance perturbations; these have periods longer than one day. The long period terms are due to the odd parity zonal harmonics, while the resonance frequencies depend on the particular orbit of the satellite. For ERS-2 the primary resonances are at the harmonics with orders that are, roughly, multiples of 14. The third type are medium period or m-daily perturbations; these have periods such that there are an integer number (m) of cycles per day. The

fourth class of perturbations are short period perturbations, which have periods of less than one orbital revolution.

The first step in tuning an existing gravity field is to determine the parameters that the new data will contribute to in the solution. By using Kaula's linear perturbation theory, the sensitivity of ERS-2 to the geopotential coefficients up to degree and order 70 is determined. Coefficients which produce at least a 5 mm radial perturbation in the ERS-2 orbit are considered significant. From this analysis, the ERS-2 tracking data is allowed to contribute to coefficients up to degree and order 45. Additionally, partials are written for the coefficients up to degree 55 for the first order coefficients and to higher degree for the resonant orders as shown in Table 5.1.

Table 5.1: ERS-2 resonance coefficients to which the PRARE data contributes

Primary		Second		Third		Fourth	
order	degree	order	degree	order	degree	order	degree
12	50	27	55	40	55	56	60
13	60	28	60	41	55	57	65
14	65	29	65	42	60	58	65
15	60	30	60	43	70	59	60
16	50			44	60		
				45	55		
				46	55		
				47	50		

The gravity field models are calculated by simultaneously solving for the gravity field coefficients, secular variations in selected zonal harmonic coefficients, ocean tides, geocenter adjustments, selected tracking station coordinates, selected tracking station biases, as well as local parameters for each

of the data sets included in the solution. The local parameters include all the parameters normally estimated when computing the orbits in UTOPIA, such as the satellite's position and velocity, drag coefficients, empirical accelerations, troposphere scale factors, and any other parameters required for the satellite and its tracking data.

To include the PRARE data set, the ERS-2 reference orbits spanning 1997 are used (as computed in Chapter 3), since it is the best year in terms of the amount and distribution of PRARE tracking. The partials of all the satellite, geophysical, and measurement parameters are calculated for each PRARE observation in UTOPIA. Besides the list of geopotential coefficients given in Table 5.1 and all the parameters normally estimated in computing the orbits (Table 3.2), partials for some of the tidal constituents, GM, and the station positions are computed.

The linearized observations and the partials at each observation are rotated by orthogonal transformations [Hasan, 1988] using a square-root free decomposition [Gentleman, 1973]. This results in the information kept in the normal equations being compressed into the DUZ information format, which contains a diagonal matrix (D), an upper triangular matrix (U) with a unit diagonal, and a column vector (Z). Once this has been done, the PRARE DUZ is combined with the DUZ's from all the other data sets used to create the gravity field which is being tuned.

The DUZ's are combined and solved using the CSR Large Linear System Solver (LLISS) program [Yuan, 1991a]. In LLISS, the estimated parameters are designated as either global, common, or local. The global parameters are those

that all of the different data sets contribute to, which includes the geopotential coefficients. The common parameters are those to which only specified sets of data contribute to. The local parameters are those to which only one data set, or DUZ, contribute. For the PRARE data, the local parameters are estimated every arc, and include the satellite state, drag coefficients, and empirical accelerations. The PRARE-specific, global parameters are the station coordinates, range biases, and a PRARE system time bias. For both the range and time biases, LLISS estimates a single uniform update to the estimates made in UTOPIA. For both JGM-3 and TEG-3, the global parameters include the 70 X 70 geopotential coefficients, ocean tides, sea surface topography (SST) spherical harmonic coefficients up to degree and order 25, the gravitational constant, geocenter locations, and selected tracking station coordinates.

For the TEG-3 gravity field, the weight for each data type is determined in LLISS, via the optimal weighting technique described by Yuan [1991b]. This results in a formal covariance which can be too optimistic. To compensate for this the computed covariance is scaled by an external calibration factor (144 for TEG-3), which is determined by comparing the predicted errors for various satellites to the observed geographically correlated radial orbit errors. TOPEX/Poseidon is particularly useful, since the dynamic orbits can be compared to the GPS reduced dynamic orbits which are not as sensitive to errors in the geopotential, thus providing a measure of the orbit accuracy.

For JGM-3, the optimal weighting technique is not used, since the information equations used to create JGM-1, which are also used in JGM-3, were created using different software and procedures [Tapley et al., 1996]. The result is

that the weights of the JGM-1 information equations are held fixed, while the new data sets are given appropriate weights relative to the JGM-1 solution.

5.2 TEG-3 AND JGM-3 COMPARISONS FOR ERS-2

This section evaluates and compares the performance of both the TEG-3 and JGM-3 gravity models for ERS-2. Some of the information presented in regard to TEG-3 is repeated from Chapter 3 to make the comparisons with the JGM-3 results more convenient. The comparisons are made in order to show the relative performance as well as the room for improvement in both fields.

The tracking data fits for 1997 are shown in Table 5.2. As alluded to earlier, it is apparent that the TEG-3 field is much better suited than JGM-3 for POD of satellites in similar orbits to ERS-2. The improvement in the RMS of the SLR residuals from 6.7 to 3.6 cm implies a removal of 5.7 cm of orbit error in a root-sum-squared (RSS) sense. The PRARE range fits indicate the same amount of improvement. The crossovers indicate that the geographically correlated radial orbit error improvement is at the 4.4 cm level (assuming the mean and variable parts are roughly equal). These improvements emphasize the room for improvement in JGM-3 for the ERS satellites.

Table 5.2: TEG-3/JGM-3 tracking data fits in 1997

Gravity Field	SLR (cm)	PRARE Dopp (mm/s)	PRARE range (cm)	Xovers (cm)
JGM-3	6.7	0.59	8.3	8.8
TEG-3	3.6	0.46	6.1	7.6

The error covariances from both gravity field solutions are used to map uncertainties in the gravity models into predicted errors in the orbits, as a function of geographical location [Rosborough, 1986]. It is important to reduce this geographically correlated orbit error as much as possible, since it goes directly into sea surface heights computed from satellite altimetry. Figure 5.1 shows the predicted ERS-2 mean geographically correlated radial orbit error for both gravity fields. The features of the two plots are very similar, with the magnitude of the uncertainties increased for the JGM-3 case. The global RMS of the uncertainties in the predicted mean geographically correlated radial orbit error is 2.5 cm for JGM-3 and 2.0 cm for TEG-3. Figure 5.2 shows the predicted ERS-2 variable geographically correlated radial orbit error for both gravity fields, rather than the mean part. As Figures 5.1 and 5.2 indicate the mean and variable radial geographically correlated orbit errors are very similar in appearance. The global RMS of the variable errors are slightly less than the mean parts, at 2.4 cm and 1.9 cm for JGM-3 and TEG-3, respectively. The RMS of the total predicted geographically correlated radial orbit error for the two gravity models is 3.6 cm for JGM-3 and 2.8 cm for TEG-3.

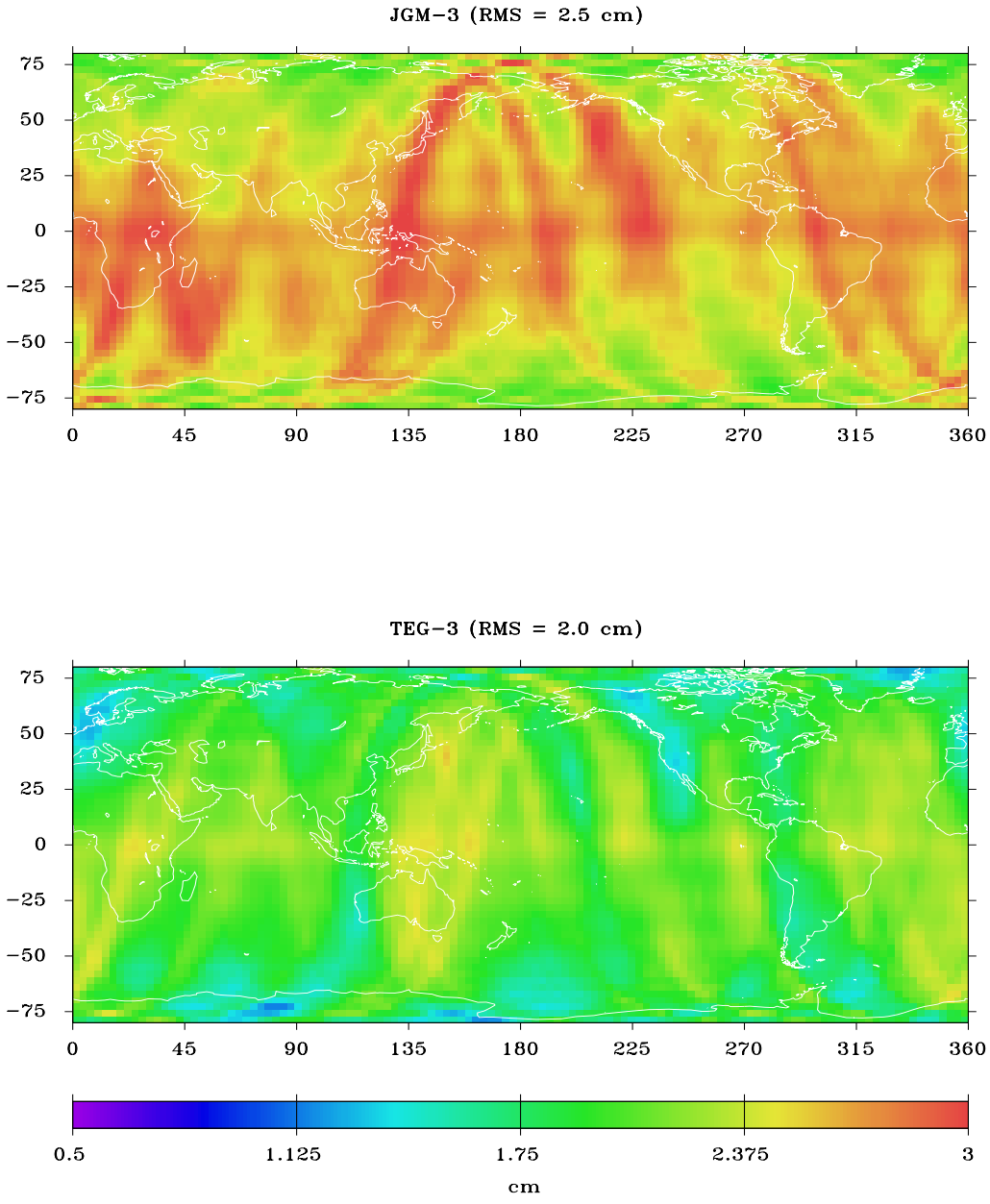

Figure 5.1: The predicted mean geographically correlated radial orbit error for ERS-2 using JGM-3 and TEG-3

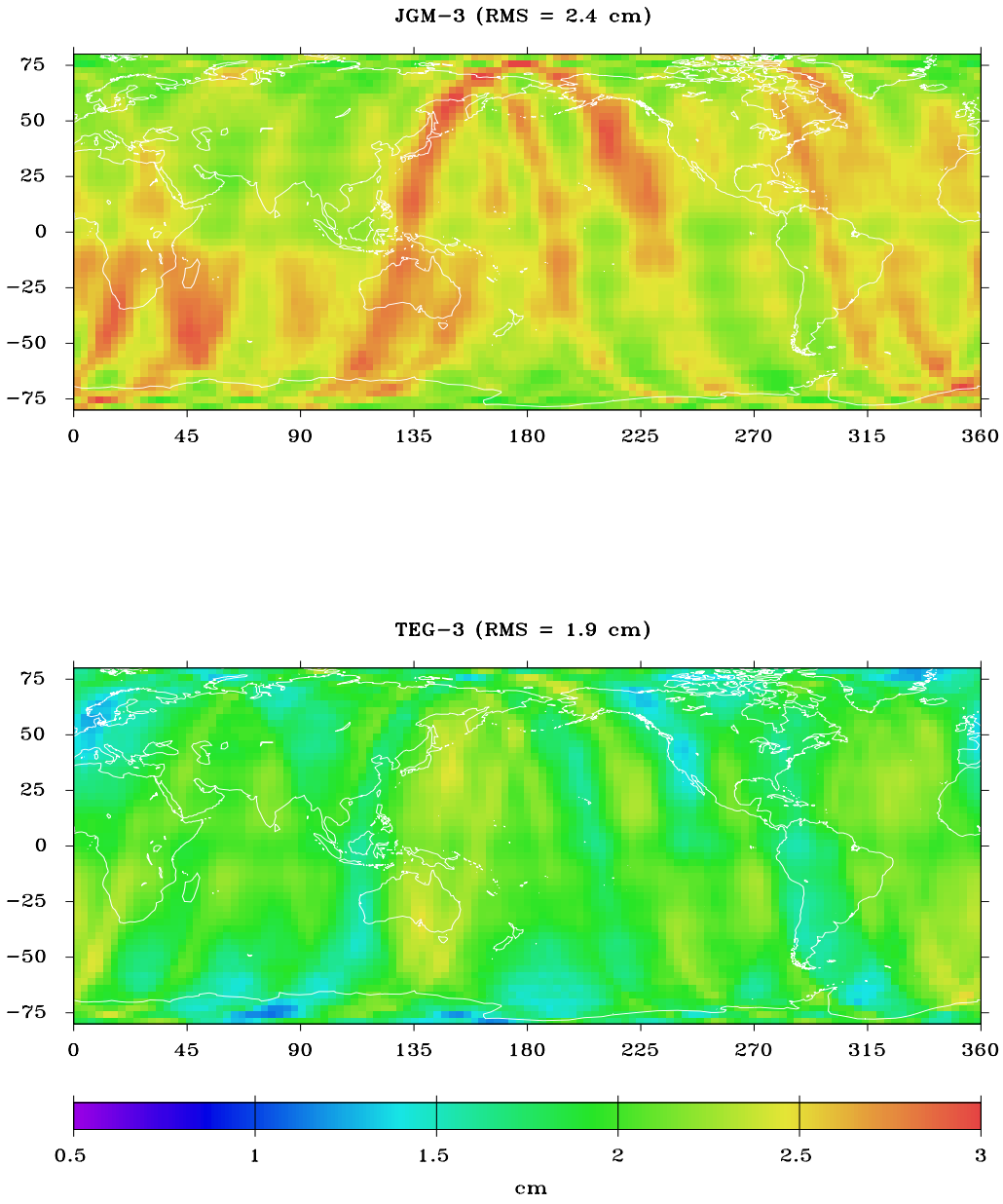

Figure 5.2: The predicted variable geographically correlated radial orbit error for ERS-2 using JGM-3 and TEG-3

The variable geographically correlated radial orbit error (Figure 5.2) represents half of the gravity induced orbit error that contributes to the crossover residuals. The variable RMS given in Figure 5.2 is a global value, whereas the altimeter crossovers only are made over the oceans. However, it turns out that the land areas are globally balanced enough so that the RMS of the predicted variable radial orbit errors do not significantly change from the global values (as given in Figure 5.2) when the land masses are eliminated. It is interesting to note that the difference, in an RSS sense, between the predicted crossover RMS for JGM-3 (4.8 cm) and for TEG-3 (3.8 cm) is only 2.9 cm. Meanwhile, the observed difference (in an RSS sense) between the observed crossover residual RMS is 4.4 cm. This suggests that either the TEG-3 covariance is too pessimistic or the JGM-3 covariance is too optimistic, illustrating the difficulty in precise calibration of any solution covariance.

In light of the reduction in both the predicted geographically correlated orbit error and the data fits when switching from JGM-3 to TEG-3, it is interesting to examine the differences between the orbits themselves. The RMS of the differences between the two sets of orbits computed over 1997 are 3.6 cm radially, 10.5 cm in transverse, and 6.5 cm in the normal direction. So, the RMS of the radial differences between the two orbits matches the predicted radial uncertainty in the JGM-3 orbit.

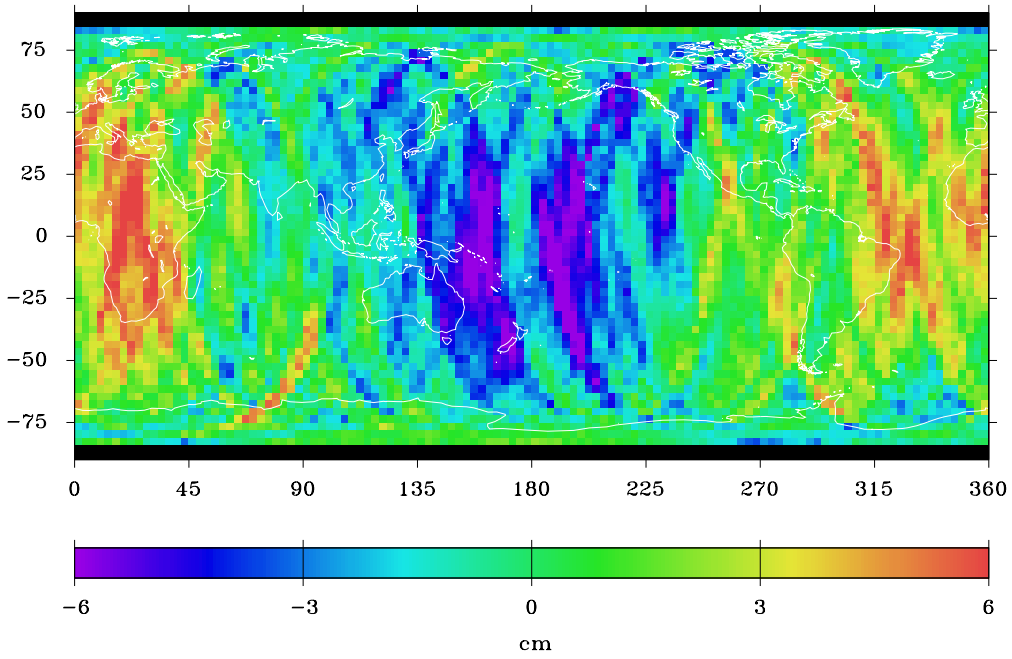

Figure 5.3: The mean radial differences between orbits computed with TEG-3 and JGM-3 during 1997 (RMS = 2.9 cm)

Figure 5.3 shows a plot of the radial differences of the two orbits averaged in 3 by 3 degree bins, which represents the mean geographically correlated radial orbit differences. The RMS of this plot is 2.9 cm, just a little higher than the predicted mean geographically correlated radial orbit error of 2.6 cm for JGM-3. The plot shows the largest orbit differences in areas with higher predicted uncertainties, as displayed previously in Figure 5.1. The pattern observed in the plot appears to be mainly attributable to differences in the odd parity first order coefficients between the two gravity models.

In general, errors in a harmonic coefficient pair ($\overline{C}_{lm}$ and $\overline{S}_{lm}$) result in errors in the geoid such that there are $(l-m)$ zeros between ±90 degrees latitude, and $2 \cdot m$ zeros along the equator. These errors cause mean geographically correlated radial orbit errors with the same longitude dependence as the geoid errors, while the latitudinal features of the geoid errors do not map directly into mean radial orbit errors [Rosborough, 1986]. Thus, errors in the first order coefficients result in mean geographically correlated radial orbit errors with a longitudinal wavelength of 360 degrees; i.e., there are two zeros along the parallels. The odd parity first order coefficient pairs result in mean geographically correlated orbit errors with no zeros along the meridians (much like the observed signal in Figure 5.3). On the other hand, errors in the even parity first order coefficient pairs contribute mainly to the variable geographically correlated radial orbit error, which cancels out when the orbit differences are averaged into a grid, as in Figure 5.3.

5.2.1 Dynamic Topography Comparisons

A way of utilizing the accuracy of the TOPEX/Poseidon orbits is to compare Sea Surface Topographies (SST's) computed from TOPEX altimetry to those computed from ERS-2. The SST represents the difference between the dynamic ocean surface calculated from satellite altimetry and the geoid. The advantage of this kind of comparison is that the orbit weaknesses can be viewed by geographic location, which can provide insight into the source of the errors. The sea surface height used to compute an SST is calculated using:

$$h_{ssh} = h_{sat} - \left(h_{alt} - h_{abias}\right) - h_{geoid}, \tag{5.1}$$

where h_{sat} is the height of the satellite above the reference ellipsoid, h_{alt} is the corrected altimeter measurement, h_{abias} is the estimated altimeter bias, and h_{geoid} represents the height of the geoid above the reference ellipsoid. These sea surface height measurements are accumulated and used to estimate spherical harmonics up to degree and order 25 which describe the surface that fits the data best in a least squares sense. The comparisons between ERS-2 and TOPEX are only meaningful for areas that are covered by both satellites, meaning latitudes between ±66 degrees.

Since the TOPEX orbits are still more accurate than the ERS-2 orbits, we can take the TOPEX SST to be an approximation of the actual SST. For reference, the mean geographically correlated radial orbit error for TOPEX orbits computed using JGM-3 has an estimated RMS of only 6 mm [Tapley et al., 1996]. Therefore, the SST differences mainly represent a relative measure of the ERS-2 mean geographically correlated radial orbit error, since only a small portion of the differences are due to errors in the TOPEX SST's. For these comparisons, the SST's are estimated using altimetry from 1997, for both ERS-2 and TOPEX/Poseidon.

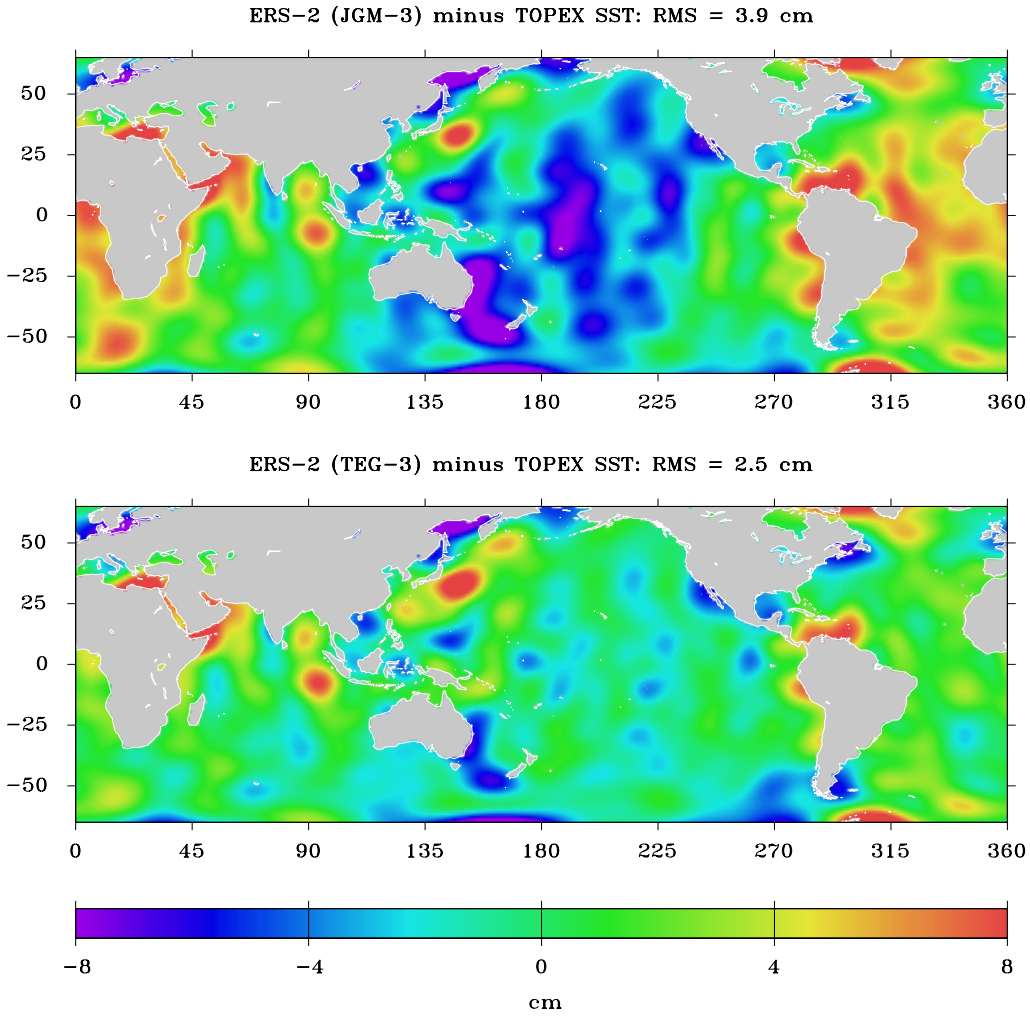

Figure 5.4: SST differences between TOPEX and ERS-2, using both JGM-3 and TEG-3 (SST's are computed using 1997 altimetry)

The top panel in Figure 5.4 shows the difference between SST's computed from ERS-2 using JGM-3 and TOPEX, where the RMS between the differences is 3.9 cm. The plot shows the presence of mean geographically correlated radial

orbit error similar to the signal observed in the radial orbit difference plot (Figure 5.3). The bottom panel shows the same comparison, except the ERS-2 orbit is computed using the TEG-3 gravity field. The gravity signal is significantly reduced in this plot, which is reflected in the reduction of the RMS from 3.9 to 2.5 cm, although a faint signal associated with the odd parity first order harmonic coefficients is still visible. Since the ERS-2 orbits are sensitive to errors in these coefficients, one of the objectives of this chapter is to try and utilize the PRARE data to tune the gravity models to reduce the geographically correlated orbit errors displayed in Figure 5.4 as much as possible.

To see why the JGM-3 and TEG-3 fields perform so differently for ERS-2, the spherical harmonic coefficients are compared. Figure 5.5 shows the absolute values of the differences in each of the coefficients, divided by the uncertainty in the JGM-3 coefficient. The left side of the plot shows the $\overline{S}_{lm}$ differences, while the right side of the plot shows the $\overline{C}_{lm}$ differences. For clarity, only those coefficients which differ by more than 1/2 sigma are shown. The coefficients are split into three categories: 1/2 to 1 sigma differences, 1 to 2 sigma differences, and greater than 2 sigma differences. The vertical grid lines represent the resonant orders for ERS-2. It is apparent that the largest differences between the two models are in the low order terms and in the ERS-2 resonant order bands. This helps to show why the JGM-3 and TEG-3 fields perform so differently for ERS-2, while for TOPEX the two perform very similarly.

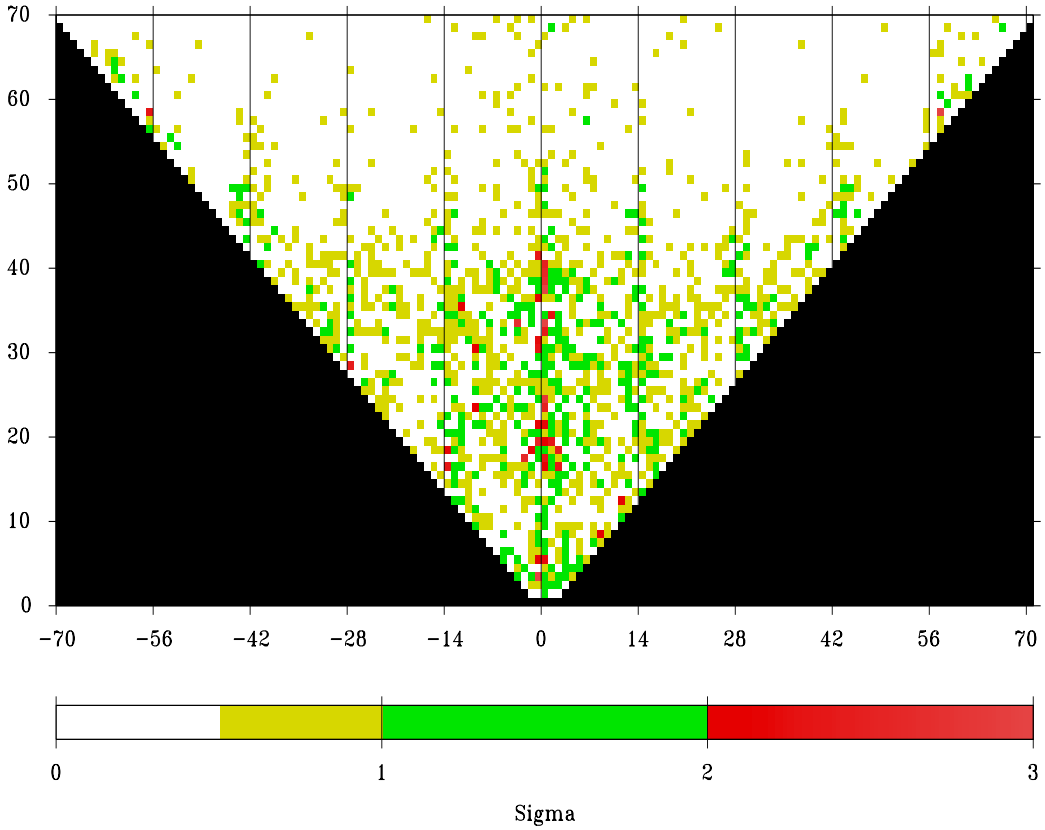

Figure 5.5: Ratio of differences in coefficients (JGM-3 minus TEG-3) and the coefficient uncertainties (JGM-3). Vertical axis is the degree, while the horizontal axis is the order of the harmonic coefficients (negative values correspond to the $\overline{S}_{lm}$ coefficients, positive values correspond to $\overline{C}_{lm}$ coefficients).

5.3 GRAVITY FIELD TUNING RESULTS

The effects of tuning both gravity fields are examined in several ways. The methods of evaluating the results include: examining the changes in the calculated geoids and the individual coefficients, evaluating the predicted orbit

errors from the solution covariances, comparing the residuals of the various data types, direct orbit and endpoint comparisons, high elevation SLR analysis, and SST comparisons. The tuned fields are also used for POD of other satellites, to ensure that the new fields are not degrading the overall model performance.

In tuning the JGM-3 field, the PRARE data is given an effective standard deviation of 50 cm and 5 mm/sec, for the range and Doppler data respectively. In comparison, the Lageos and Stella SLR data are given an effective standard deviation of 30 cm while for the TOPEX DORIS data the value is 6 mm/sec [Tapley et al., 1995].

In tuning the TEG-3 field, the optimal weighting algorithm assigned an effective standard deviation of 52 cm and 5.2 mm/sec, for the PRARE range and Doppler data respectively. In comparison, the optimal effective standard deviation for the TOPEX SLR data is 35 cm and for the Spot 2 DORIS data is 6.5 mm/sec. The effective standard deviations include a scale factor of 13, which is squared and applied to the solution covariance. Scaling the covariance by 169, rather than the 144 originally used for TEG-3, keeps the predicted radial orbit error for TOPEX the same as it is using the standard TEG-3 model. This increase in the scale factor is necessary, since the addition of new weighted data in the solution increases the optimism of the formal uncertainties in the estimated parameters. In the end, there is very little difference between the two weighting schemes used to tune both the JGM-3 and TEG-3 models, as we should expect.

5.3.1 Geoid and Coefficient Comparisons

The changes in the tuned gravity fields can be observed by plotting the differences in the geoid heights. This allows the changes to be viewed by geographical region. Figure 5.6 shows the geoid changes for both the JGM-3 and TEG-3 fields, while Figure 5.7 shows the uncertainties in both the JGM-3 and the TEG-3 geoid. From this point on, the tuned fields are denoted as JGM-3P and TEG-3P. As expected, the TEG-3 field is less impacted by the tuning effort than the JGM-3 field. The RMS of the geoid differences for the TEG-3 field is 13.4 cm, while for JGM-3 the RMS is 17.9 cm. For both cases, the largest differences are in the areas where the geoid is the most uncertain, such as over Antarctica, Asia, and Africa. Additionally, most of these large changes coincide with areas covered by PRARE tracking. Generally, however, the changes simply reflect changes in the spherical harmonic coefficients (particularly the less well determined higher degree and order terms) consistent with their uncertainties and are not necessarily an indication of geoid improvement. Meanwhile, the changes over the better determined parts of the geoid are much smaller, such as over the oceans, North America, and Europe. The RMS of the geoid differences between the original and the tuned gravity models over the oceans is 3.5 cm for TEG-3, and 6.3 cm for JGM-3. The geoid is better determined over the oceans because of the satellite altimetry used in computing the gravity models. The geoid is better determined over North America and Europe due to the larger amount of SLR tracking data and the higher quality surface gravity measurements available in these areas.

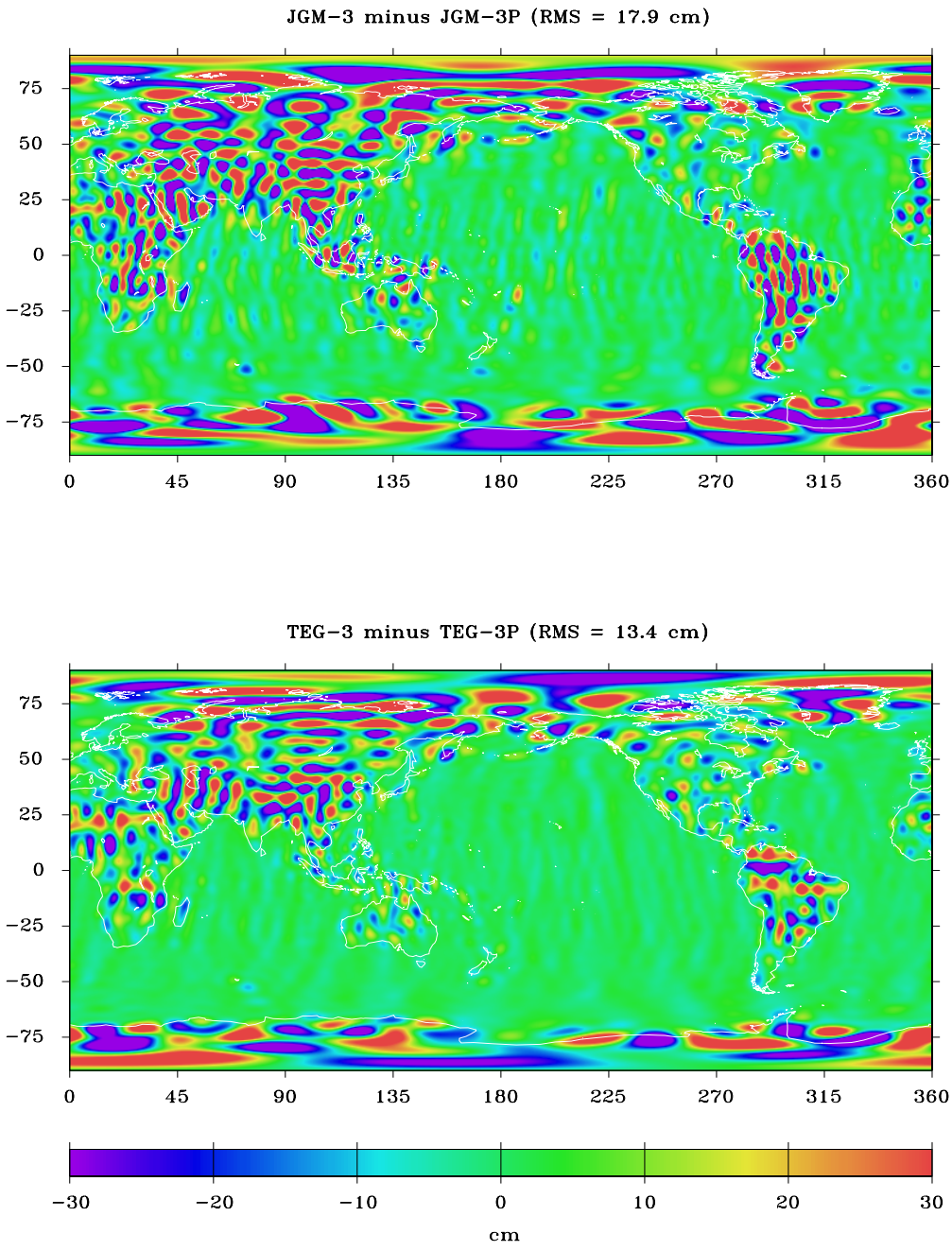

Figure 5.6: Geoid changes after tuning gravity fields

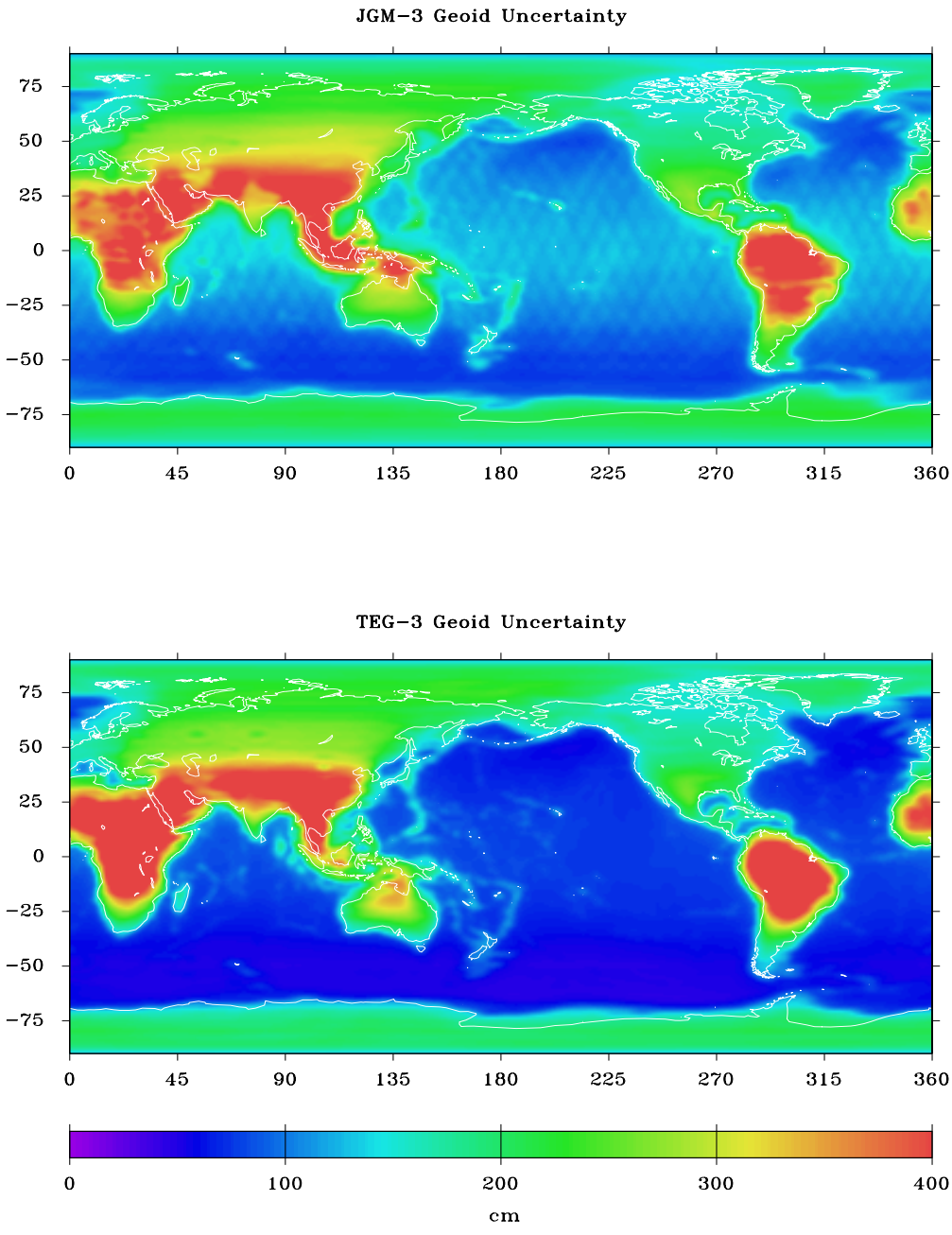

Figure 5.7: Geoid uncertainties

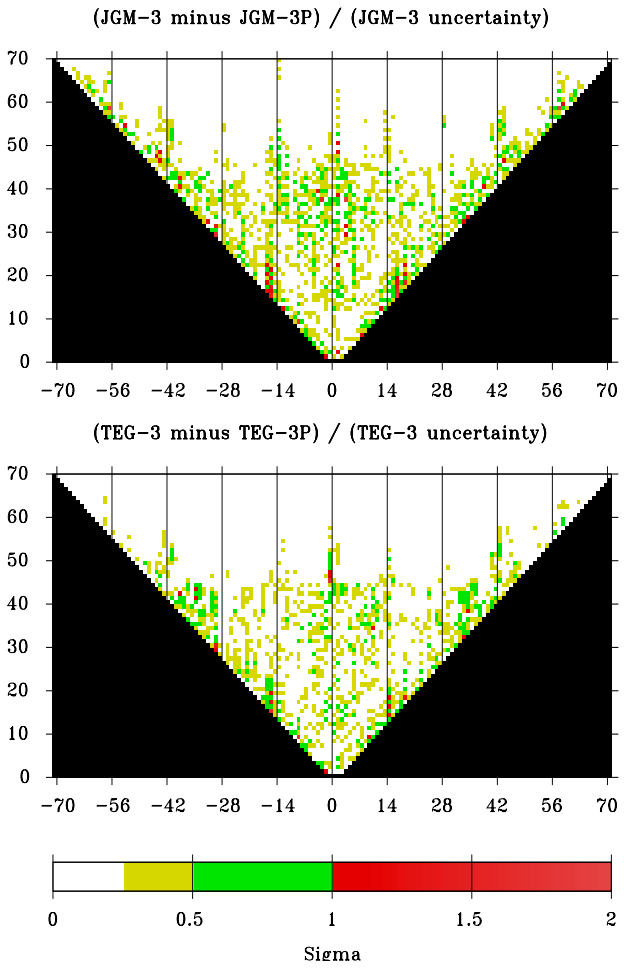

Figure 5.8: Ratio of differences in coefficients and coefficient uncertainties. Vertical axis is the degree, while the horizontal axis is the order of the harmonic coefficients.

The effects of tuning the gravity models are also shown by examining the magnitude of the changes in the coefficients, similar to the comparison made in Figure 5.5 between JGM-3 and TEG-3. Figure 5.8 shows the magnitude of the differences in individual coefficients divided by the uncertainty of the

coefficients, for both tuned gravity fields. The top panel compares the JGM-3 model, before and after tuning; similarly, the bottom panel compares effects of tuning the TEG-3 model. As expected, the PRARE tracking data has a larger impact on the JGM-3 field. The largest changes in the JGM-3 model occur at low orders, in the resonance order bands, and in the lowest degree terms for each order (including the sectorials). For the TEG-3 field, the changes do not seem to correlate as much with the resonant order bands, reflecting the fact that TEG-3 included ERS-1 tracking. For both cases, most of the changes are less than the uncertainty of the coefficients, which indicates that the PRARE data is not given too much weight in the solutions.

5.3.2 Predicted radial orbit errors

The covariance for the two new gravity solutions are used to predict radial orbit errors, as was previously done for JGM-3 and TEG-3 in Section 5.2. Figure 5.9 shows the predictions for both tuned gravity fields. The two plots are much more similar than the corresponding plots for JGM-3 and TEG-3, which indicates that the two models should perform similarly for ERS-2 POD. Both plots indicate zonal characteristics, exhibited by the faint horizontal banding. Additionally, there is a groundtrack region over the mid-Atlantic and the Western Pacific which has higher than average predicted radial orbit errors. These regions correspond to areas that are not covered well by either SLR or PRARE tracking.

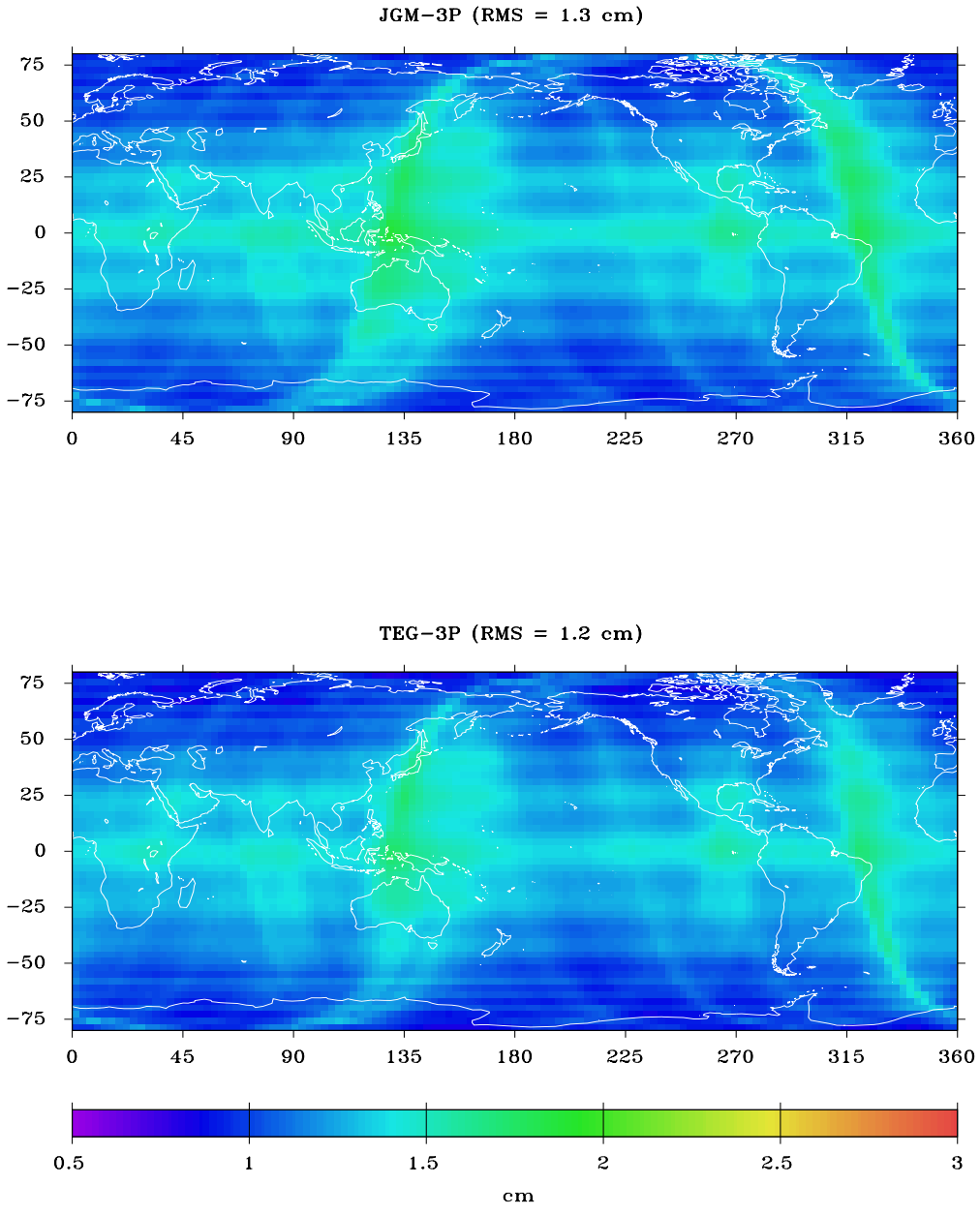

Figure 5.9: The predicted mean geographically correlated radial orbit error for ERS-2 using TEG-3P and JGM-3P

The RMS of the predicted mean geographically correlated orbit error is 1.3 cm for JGM-3P and 1.2 cm for TEG-3P, compared to 2.5 cm for JGM-3 and 2.0 cm for TEG-3. Not shown in Figure 5.9, the RMS of the predicted variable part is 1.2 cm for JGM-3P and 1.1 cm for TEG-3P, making the total predicted geographically correlated radial orbit error 1.7 cm for JGM-3P and 1.6 cm for TEG-3P.

The predicted orbit errors for both tuned gravity models reflect a significant amount of improvement over the original models. The next sections will examine if these predictions are valid, or if the tuned gravity solution covariances are too optimistic.

5.3.3 ERS-2 Data Fits

Each of the tuned gravity fields is used to compute orbits during 1996. This prevents the PRARE residuals from being artificially low, since the gravity solutions used only the 1997 PRARE data. Table 5.3 shows the resulting RMS of the residuals for PRARE/SLR orbits computed using the four different gravity models. The improvement in both the SLR and crossover residuals, as well as the PRARE residuals, clearly indicates that the orbits computed with the tuned fields perform better for ERS-2 POD. As predicted, the data fits for the orbits computed with both of the tuned fields are almost identical, making it hard to determine if the JGM-3P or TEG-3P model is outperforming the other.

Table 5.3: Tracking data fits before and after tuning for 1996

Gravity Field	SLR (cm)	PRARE Dopp (mm/s)	PRARE range (cm)	Xovers* (cm)
JGM-3	6.3	0.57	8.2	8.8
JGM-3P	3.5	0.41	5.0	6.8
TEG-3	3.5	0.44	5.9	7.7
TEG-3P	3.3	0.40	5.0	6.8

* crossovers given zero weight in solution

The reductions in the crossovers may be the most telling portion of Table 5.3, since this data is not used in either orbit determination or in tuning the gravity models. Using the 4.1 cm estimate for the ERS-2 crossover measurement noise (from the crossover error budget in Table 3.9) and the crossover analysis of Section 3.3.3, the 6.8 cm crossover residual RMS translates to a radial orbit accuracy of 2.6 cm. For JGM-3, this represents a very large improvement in the radial orbit accuracy, from 6.2 cm to 2.6 cm. Meanwhile, for TEG-3 the reduction in the crossovers improves the radial orbit accuracy from 4.3 cm to 2.6 cm.

The reductions in the SLR residuals for JGM-3 show similar levels of improvement. The drop from 6.3 to 3.5 cm reflects an improvement of 5.2 cm in an RSS sense. Keep in mind, the SLR residuals measure three dimensional orbit error, not just the radial component. Interestingly, the SLR residuals for the TEG-3 orbits do not reflect the same level of improvement as the crossover residuals. The reduction from 3.5 to 3.3 represents a 1.1 cm three dimensional improvement (in an RSS sense), which is much less than the 2.1 cm radial improvement

observed from the crossover RMS. This could mean the orbits do not improve as much over regions where the SLR tracking is most prevalent, mainly Europe and North America. This is supported to some degree by the previous geoid comparison, in which the largest differences occur in areas other than Europe and North America. It is also supported by the fact that the TEG-3 PRARE range residuals reflect a three dimensional improvement of 3.1 cm in an RSS sense, which is more consistent with the amount of reduction observed by the crossover residuals.

5.3.4 Orbit Comparisons

The orbits, computed before and after tuning the gravity models, are compared to determine the amount of change and the characteristics of the differences. Table 5.4 displays the RMS of the differences between orbits computed using the various gravity models. Of the three orbits compared, the two that have the best agreement are the TEG-3P and JGM-3P cases, which agree in the radial direction at the 9 mm level. This again shows how similarly the two tuned fields perform for ERS-2 POD, even though the untuned models produce quite different results.

Table 5.4: RMS of the orbit differences between different gravity models (cm)

Comparison	Radial	Transverse	Normal	3-D
JGM-3 / JGM-3P	4.2	13.9	7.3	16.3
TEG-3 / TEG-3P	2.4	7.7	4.5	9.2
JGM-3P / TEG-3P	0.9	2.2	1.9	3.0

The radial results are presented geographically in Figure 5.10, where the radial differences are averaged in bins that are 3 by 3 degrees in latitude and longitude. The plots represent the differences in the mean geographically correlated orbit errors, since the variable differences cancel out during the averaging of ascending and descending passes in each bin. For the two top panels, the differences represent the mean geographically correlated orbit error that is removed by tuning the respective gravity models. For both cases, the new gravity models have removed orbit errors associated with errors in the odd parity first order coefficients, as discussed in Section 5.2.

The improvement in the TEG-3 case agrees quite well with the predicted improvement from the computed geopotential covariance. From Figures 5.1 and 5.9, the predicted mean geographically correlated radial orbit error is 2.0 cm for TEG-3 and 1.2 cm for TEG-3P. This implies a removal of 1.6 cm of mean radial orbit error from the TEG-3 orbit. The second panel in Figure 5.10 shows a mean radial orbit difference of 1.7 cm between TEG-3 and TEG-3P orbits, which is close to the predicted improvement. For JGM-3, the predicted mean radial orbit error is reduced from 2.5 to 1.3 cm, which implies a 2.1 cm improvement in accuracy with the JGM-3P gravity model. But, from the top panel in Figure 5.10, the mean orbit difference is significantly larger at 3.5 cm. Again, this could be the result of the JGM-3 covariance being too optimistic.

The bottom panel of Figure 5.10 shows the mean radial orbit differences between orbits computed using the two tuned gravity models. It shows that there is no strong pattern associated with the mean differences, which is also reflected in the 0.6 cm RMS of the mean geographical differences.

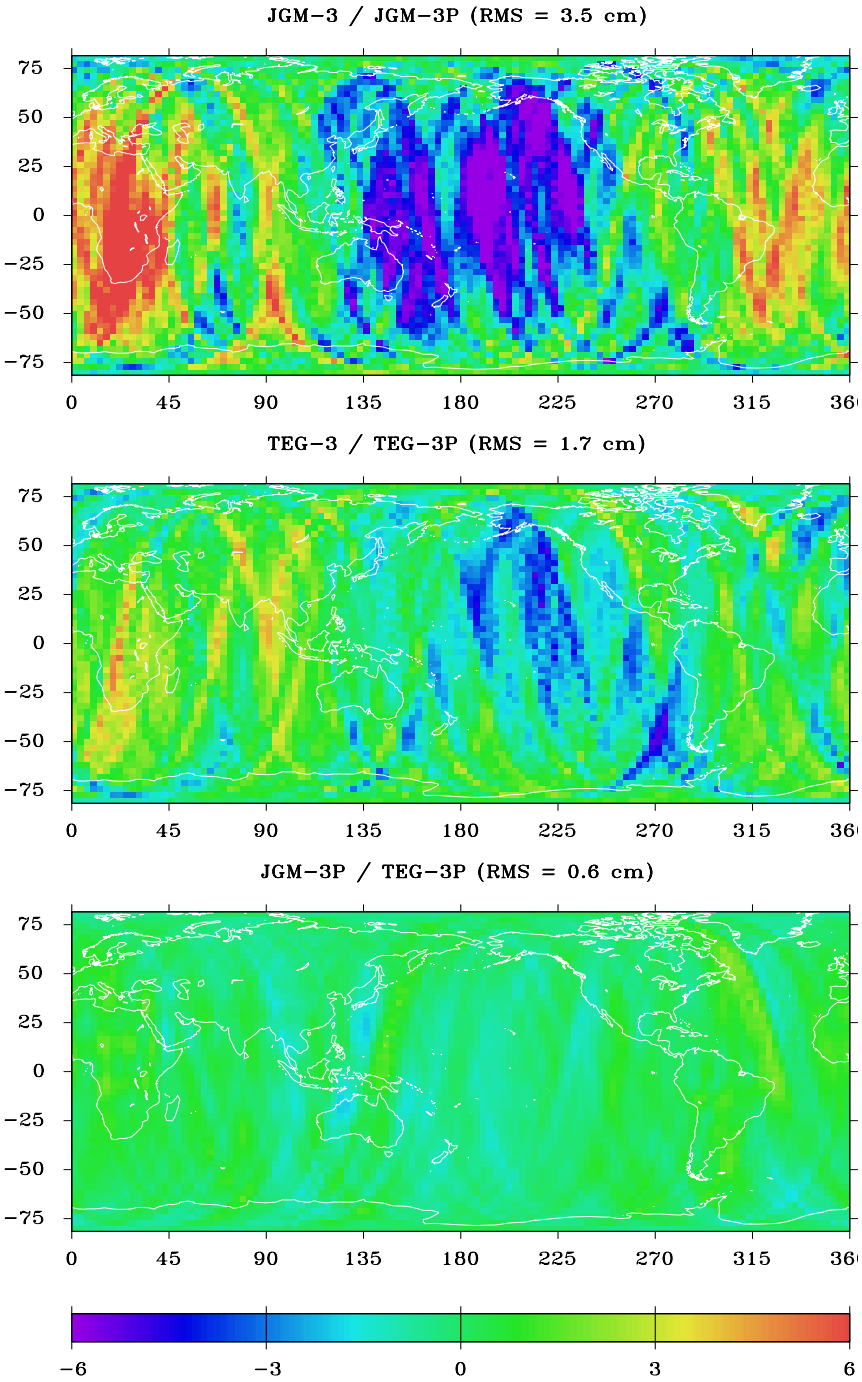

Figure 5.10: The mean radial differences between orbits computed with different gravity models during 1997

5.3.5 Orbit Endpoint Analysis

Comparing the orbit arc endpoints, as described in Section 3.2.2, provides a good measure of the orbit performance. The statistics for the 49 endpoints during 1997 that do not coincide with burns are given in Table 5.5. This comparison shows that the two tuned fields not only improve the radial performance, but also the transverse and normal directions become more consistent. Of the two tuned fields, TEG-3P performs a little better than JGM-3P, except in the transverse direction. However, as the direct orbit comparisons revealed, the two tuned orbits are very close in all aspects.

Table 5.5: RMS of the differences between orbit arc endpoints (cm)

Gravity Model	Radial	Transverse	Normal	3-D
JGM-3	6.2	43.9	7.9	45.0
JGM-3P	2.4	11.9	4.9	13.1
TEG-3	2.7	16.8	5.7	17.9
TEG-3P	2.2	12.4	4.6	13.4

5.3.6 Sea Surface Topography Comparisons

The new orbits computed with the tuned gravity fields are used to produce SST's which are compared to TOPEX generated SST's, as discussed in Section 5.2.1. The differences between the tuned ERS-2, and TOPEX SST's are shown in Figure 5.11. The RMS of the differences between both the JGM-3P and TEG-3P SST's and the TOPEX SST is 2.3 cm. In an RSS sense, this implies an improvement of 3.1 cm and 1.0 cm for JGM-3 and TEG-3, respectively (from

Figure 5.1). Since some of the mean radial orbit errors for ERS-2 and TOPEX can be expected to be correlated, the reduction in power for the tuned orbits is not as large as the observed mean radial difference between the untuned and tuned ERS-2 orbits (Figure 5.10).

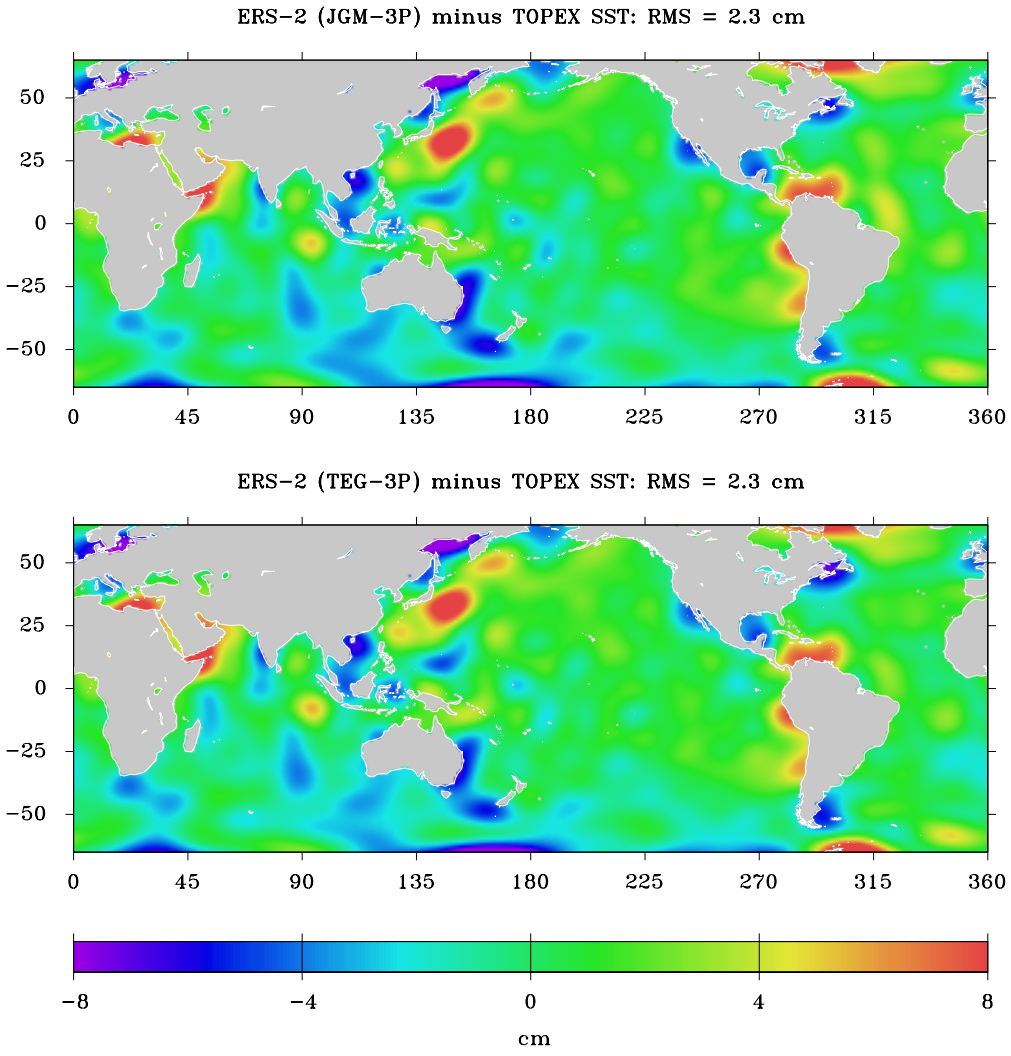

Figure 5.11: SST differences between TOPEX and ERS-2, using both JGM-3P and TEG-3P

Some of the larger spots, seen in both cases, occur in areas of high ocean variability and where the ocean tides are not well determined. This, in combination with the different sampling rates of the ERS-2 and TOPEX altimeters can explain most of these large differences, which have the effect of inflating the RMS of the differences to some extent. Some of the differences could also be attributed to errors in the corrections applied to the altimeter data. The small, well defined nature of these features make it unlikely that they are caused by orbit error. If these isolated areas are removed, the statistics provide more insight into the accuracy of the orbits used to generate the SST's. The mask shown in Figure 5.12 is used to edit the SST differences shown in Figures 5.1 and 5.11. The RMS of the differences between the masked SST's are given in Table 5.6, also the predicted mean geographically correlated radial orbit errors are repeated for convenience.

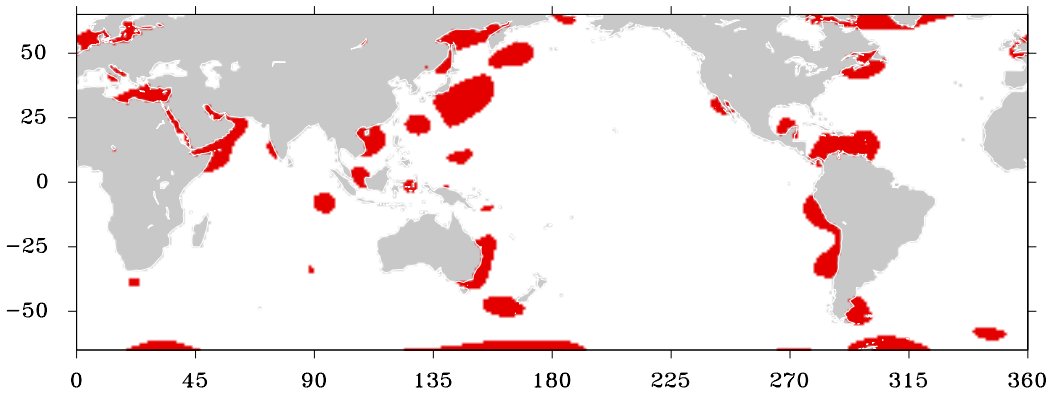

Figure 5.12: Mask used for editing SST's

The level of agreement between the TOPEX SST and the ERS-2 SST's are close to the predicted mean geographically correlated radial orbit errors. The SST differences include more than just the mean radial orbit errors from ERS-2. They also contain TOPEX errors and any geographically correlated altimeter correction errors. Therefore, the ERS-2 mean radial orbit error should be less than the RMS of the differences in the SST's. This holds true for all of the predicted mean radial orbit errors except TEG-3, which points to the TEG-3 covariance being on the pessimistic side. The opposite is true for JGM-3, where the predicted mean radial orbit error is much less than the RMS of the differences in the SST's. In any case, the predicted mean radial orbit errors for the two tuned gravity models seem realistic in comparison to the observed SST differences.

Table 5.6: Differences between masked ERS-2 and TOPEX SST's (cm)

Gravity Model	RMS of difference	Predicted mean radial orbit error
JGM-3	3.6	2.5
JGM-3P	1.6	1.3
TEG-3	1.8	2.0
TEG-3P	1.5	1.2

5.3.7 PRARE-only orbit analysis using High Elevation SLR data

PRARE-only orbits are computed during 1996. The resulting data fits are shown in Table 5.7 for each of the gravity models. All of the residuals show similar levels of improvement, with the tuned gravity fields, to the reductions

obtained in the PRARE/SLR orbits (Table 5.3). Following Section 3.3.3, the high elevation SLR passes are used to evaluate radial accuracy of the PRARE-only orbits. The last column in Table 5.7 shows the estimated radial orbit errors using this method, labeled as the radial accuracy over SLR stations. Since these orbits span only 1996, the results are not as good as 1997, due to less active PRARE stations. Regardless, the PRARE-only orbits computed using the tuned gravity fields provide about 3.5 cm radial accuracy, at least over areas that provide coverage by SLR stations.

Table 5.7: Tracking data fits for PRARE-only orbits and radial orbit accuracy estimates

Gravity Field	SLR* (cm)	PRARE Dopp (mm/s)	PRARE range (cm)	Xovers* (cm)	Radial Accuracy over SLR stations
JGM-3	8.7	0.59	8.3	8.8	4.8
JGM-3P	5.0	0.42	5.1	6.9	3.5
TEG-3	5.5	0.46	6.1	7.6	4.4
TEG-3P	5.0	0.41	5.2	6.9	3.4

* SLR and crossovers given zero weight in solution

5.3.8 Orbit Accuracy Conclusions

The PRARE/SLR orbits computed with TEG-3 have a radial orbit accuracy in the range of 3.5 to 4.5 cm, based on the analysis of Chapter 3. The orbits computed with the tuned gravity fields are more accurate, especially over areas where there is no SLR tracking. The two tuned fields, JGM-3P and TEG-3P, both perform very similarly for ERS-2 POD, with TEG-3P providing slightly

more accurate orbits. This is a testament to the power of the PRARE data, considering the large amount of data from satellites in similar orbits to ERS-2 that is included in the TEG-3 model, but not in the JGM-3 model.

The SST comparisons and the crossover residuals have validated the predicted radial orbit errors from the gravity solution covariances for the tuned fields. The same analysis has indicated that the JGM-3 covariance may be slightly optimistic and the TEG-3 field may be a little pessimistic, at least for ERS-2. Nevertheless, the total predicted geographically correlated radial orbit errors are combined, in an RSS sense, with the RMS of the radial orbit endpoint differences (to capture the variable component of the orbit error) to provide an estimate for the total radial orbit accuracy. This method should provide a conservative estimate of radial orbit error, since the endpoint differences are not completely independent of gravity induced orbit errors.

Table 5.8 presents the radial orbit errors predicted from the crossover residuals, the total predicted geographically correlated orbit errors (from Sections 5.2 and 5.3.2), the RMS of the radial orbit endpoint differences (from Table 5.5), along with the estimated radial orbit errors from the combination of the predicted radial orbit errors and the radial orbit endpoint differences (RSS of the second and third columns). This test indicates that the global radial accuracy of the PRARE/SLR orbits computed using either the JGM-3P or TEG-3P models is approaching the 3 cm level.

Table 5.8: Radial orbit accuracy estimates (cm)

Gravity Model	**Predicted from crossovers**	Predicted (Gravity induced)	Radial Endpoint RMS	**Total (RSS of gravity and non-gravity induced errors)**
JGM-3	**6.2**	3.6	6.2	**7.2**
JGM-3P	**2.6**	1.7	2.4	**2.9**
TEG-3	**4.3**	2.8	2.7	**3.9**
TEG-3P	**2.6**	1.6	2.2	**2.7**

As shown in Table 5.8, this test indicates that the radial accuracy of the PRARE/SLR orbits computed with the TEG-3 gravity model is about 3.9 cm, which is within the 3.5 to 4.5 cm accuracy predicted for these orbits in Chapter 3. This test can also be applied to orbits computed using SLR data and the altimeter crossovers, which is how the ERS-1 orbits are estimated. The predicted level of radial orbit error for the orbits computed in this manner is 4.3 cm when the TEG-3 gravity model is used, and 3.3 cm when the TEG-3P gravity model is used.

In summary, the radial accuracy of the PRARE/SLR ERS-2 orbits computed with either of the tuned gravity fields is between the 3.0 and 3.5 cm level. This conclusion is supported by the high elevation SLR analysis, the crossover analysis, and the combination of estimates for gravity and non-gravity induced orbit errors.

5.4 IMPACT ON OTHER SATELLITES

The tuned gravity fields have been shown to improve the orbits for ERS-2, but an important aspect of the new models is how the tuning effects POD for

satellites with different orbit characteristics. If the resulting gravity models are an improvement, there should be no degradation of the orbit quality for other satellites. On the other hand, the gravity field adjustments are not expected to improve the orbits for other satellites, outside of those in orbits very similar to ERS-2. The majority of the changes in these fields were small in magnitude. Most of the coefficients changed by an amount less than their uncertainty, as displayed in Figure 5.8. This, coupled with the fact that different satellites are not sensitive to the same combinations of coefficients that ERS-2 is most sensitive to, makes it unreasonable to expect significant orbit improvement from the tuned gravity fields for other satellites. Table 5.10 gives the RMS of the tracking data residuals computed from orbits calculated using the four different gravity fields, for several satellites with varying orbit elements (shown in Table 5.9).

Table 5.9: Approximate satellite altitude, inclination, and eccentricity

Satellite	Altitude (km)	Inclination (deg)	Eccentricity
Lageos-1	5900	110	0.005
Lageos-2	5800	53	0.013
Ajisai	1480	50	0.0004
Starlette	960	50	0.02
Stella	800	99	0.0015
ERS-1/2	780	99	0.001
NOVA	1170	90	0.0015
GEOS-3	840	115	0.001
SPOT-2	810	99	0.003
Geosat	780	108	0.001
TOPEX	1300	66	0.001

The data fits are not the optimal way to compare the orbits, since for some of the cases the orbits are flexible enough to fit the data used in the POD process. For instance, the SPOT-2 satellite is fitting the DORIS data at the approximate noise level of the observations. Therefore, the residuals do not reflect any relative accuracy between the different orbits. To overcome this, some of the orbits are calculated without estimating the empirical accelerations (Lageos 1 & 2, Ajisai, Starlette, Stella). This prevents the orbit from being flexible enough to overcome errors in the gravity model. This technique is only possible when the once per revolution perturbations caused by force mismodeling are small; otherwise the orbit fits become so poor as to be meaningless.

Table 5.10: Data Fits for different satellites (cm, mm/sec)

Satellite	Tracking	JGM-3	JGM-3P	TEG-3	TEG-3P
Lageos-1 (1)	SLR	2.58	2.53	2.53	2.53
Lageos-2 (1)	SLR	2.44	2.44	2.37	2.38
Ajisai (1)	SLR	5.13	5.10	5.55	5.54
Ajisai		3.40	3.40	3.38	3.38
Starlette (1)	SLR	4.86	4.84	4.86	4.85
Starlette		4.21	4.18	4.04	4.03
Stella (1)	SLR	9.36	5.30	5.61	5.50
Stella		6.40	3.25	2.99	2.76
ERS-1	SLR	5.53	3.12	3.16	2.95
	Xover	9.22	6.79	7.25	6.73
GEOS-1	SLR	30.52	30.57	32.91	33.31
SPOT-2	DORIS	0.547	0.541	0.540	0.542
NOVA	TRANET	3.32	3.30	3.06	3.06
Geosat	TRANET	7.59	7.59	7.59	7.59
	Xover	20.07	20.08	19.94	19.96
TOPEX	SLR	2.47	2.47	2.45	2.47
	DORIS	0.550	0.550	0.550	0.550
	Xover	6.13	6.11	6.15	6.16
(1) Orbits estimated without 1/rev accelerations					

Chapter 6

Conclusions

6.1 SUMMARY

The PRARE satellite tracking system is described in the first part of Chapter 2. This description includes details on how the measurements are made and modeled. The measurement corrections applied to the PRARE observations are also reviewed. The troposphere corrections supplied with the PRARE data are improved through the use of the ECMWF atmosphere model and the Niell mapping function. Later in the chapter, the Guier editing technique used to edit the PRARE data is discussed. This analysis indicated that the noise level of the PRARE data is at the 2.5 cm and 0.25 mm/sec level, for range and Doppler respectively. Thus, the range measurements have roughly three times the noise level of the SLR range measurements, while the Doppler measurements have about half the noise level of the DORIS Doppler measurements.

The PRARE data allows the ERS-2 orbits to be estimated with a higher degree of accuracy than possible for ERS-1. Additionally, the orbits are computed without reliance on satellite altimetry, so there is no chance of ocean signals being aliased into the orbits. In comparison to SLR, the strength of the PRARE system is in the quantity and distribution of the tracking data, as displayed in Figures 3.1 and 3.2. In comparison with the DORIS system, the strengths of the PRARE system are in its ability to provide both range and more precise Doppler measurements. Additionally, the two-way Doppler measurements made by

PRARE eliminate the clock offsets experienced by the DORIS Doppler measurements, which are handled by estimating frequency offsets. On the other hand, the DORIS system provides even better global coverage than PRARE.

A problem with the PRARE system, in comparison to both the SLR and DORIS systems, is the less than reliable nature of the tracking stations. Due partially to their complexity, the ground stations often break down or malfunction. The problem is exacerbated by the long lead time required to repair the stations and the lack of spare parts available. Some of these problems are related to the production of most of the stations being complete for the ERS-1 mission, which was launched four years prior to ERS-2, and the limited design life of the stations.

Chapter 3 begins with a brief description of the orbit determination problem, including information on the various models used to compute the orbits. The next section details the PRARE-dependent parameters which need to be estimated. This includes discussions on the characteristics of these estimated parameters and rationale for the frequency that they are estimated. Next, the accuracy of the ERS-2 orbits are evaluated by analyzing: the tracking data residuals, direct orbit comparisons, the consistency between adjacent orbit arc endpoints, high elevation SLR residuals, and altimeter crossovers. Using the TEG-3 gravity field, the radial orbit accuracy for the orbits computed with PRARE and SLR is estimated to be 3.5 to 4.5 cm. This is better than the best ERS-1 orbits, which are estimated to be accurate at the 5 cm level. Additionally, the PRARE data eliminates the need to rely on the altimetry in POD.

The effectiveness PRARE network is further assessed by analyzing the accuracy of the station solutions computed from the tracking data. The first part of

Chapter 4 explains the procedure used to compute the PRARE station solutions. Next, the solutions are evaluated by examining the solution repeatability, comparing the solutions to surveyed coordinates, and by making external comparisons. The resulting accuracy of the PRARE station solutions is determined to be between 3 and 5 cm, depending on the particular station. Additionally, it is shown that the SLR data provides an anchor that effectively maintains the reference frame in the CSR95L01 coordinate frame, for both the orbits and the station coordinates.

The last part of Chapter 4 deals with the station installed at the Neumayer Ice Station. Since this station is located on an ice sheet, it provides the challenge of estimating the station position for a moving target. The ice sheet flows Northward with a steady velocity of about 40 cm/day. Additionally, the station's vertical position changes with the Ocean tides, since the ice sheet is floating. The motion of the station due to the ice flow is estimated and modeled as a linear velocity. The vertical positions are estimated for every pass of the satellite, and the resulting time series is used to estimate ocean tides. The estimated tide model provides agreement with the CSR3.0 tide model at the uncertainty level of both models, considering the geographic location of the station. Properly handling this station allows a significant amount of otherwise useless PRARE data to be given some weight in the POD process.

The PRARE data proves to be a valuable tool in tuning the gravity field for satellites in similar orbits to ERS-2, as discussed in Chapter 5. The chapter starts with a general description of the technique used to tune both the JGM-3 and the TEG-3 gravity fields. The effectiveness of the PRARE data is due to the

location of the stations and the quantity of data. The PRARE stations in areas not covered by SLR impact the gravity solutions the most. The results of the tuning effort are seen by examining changes in the geoid, changes in the individual coefficients, as well as the predicted radial orbit errors from the gravity solution covariances. The orbits computed with the tuned gravity fields are analyzed using the same methods described in Chapter 3. Additionally, the orbits are assessed by comparing SST's estimated from ERS-2 altimetry to those estimated from TOPEX/Poseidon altimetry. This test also allows the scaling of the gravity solution covariances to be verified, by comparing the SST differences to the predicted mean radial orbit errors. This analysis shows that the addition of the PRARE data to the JGM-3 field results in a gravity model that performs at virtually the same level as the tuned TEG-3 model. This indicates the strength of the PRARE data, since the TEG-3 model contains a significant amount of tracking not in JGM-3, from two satellites in similar orbits to ERS-2 (ERS-1 and Stella).

The combination of all the tests performed in Chapter 5 indicates that the ERS-2 orbits computed with either tuned gravity field, and both the PRARE and SLR data, have radial accuracies between 3.0 and 3.5 cm. This is a significant improvement over the estimated radial accuracy of 3.5 to 4.5 cm, determined for the TEG-3 orbits in Chapter 3. Additionally, this makes the ERS-2 orbits significantly more accurate than the 5 cm level orbits produced for ERS-1, which are computed using SLR and altimetry.

6.2 FUTURE WORK

Although there are currently no plans to fly PRARE on any future satellites, the contribution of PRARE to ERS-2 POD is valuable. Also, the tuned gravity models can be used to improve the accuracy of the ERS-1 orbits. This is important because ERS-1 provided a significant amount of satellite altimetry before TOPEX/Poseidon was launched and covers more of the oceans than TOPEX, with denser coverage due to the longer duration of the repeat cycle. This makes it important to the oceanographic community that the ERS orbits are precise as possible. The altimeter data is also an important tool used to analyze the polar ice sheets, which are not covered by the TOPEX orbit. SAR users also rely on having the orbits as accurate as possible. In fact, to realize the full potential of the SAR measurements, more stringent requirements are put on the three-dimensional orbit accuracy than for altimetry.

Further down the road, the CHAMP and GRACE gravity recovery missions will provide a significant improvement in the gravity models. This will allow the ERS orbits to be computed at even higher levels of accuracy.

Appendix A

PRARE Data Preprocessing

The preprocessing program, PDRP, converts the raw PRARE observations from the GFZ format to the CSR UTOPIA format. The following subsections describe how both the range and range-rate measurements are converted.

A.1 PRARE RANGE MEASUREMENTS

The PRARE range measurements are converted from the GFZ format (Revision 5) to the CSR UTOPIA observation format. In particular, the measurements are converted from two-way travel time to one-way range. During this conversion, all of the corrections are applied to the range measurements, with the exception of the supplied troposphere delay. Before delivery, the raw two-way travel time observations have been corrected for the internal calibration of both the space segment and the ground station, along with the 91 value range correction. The following explains how the raw range measurements are converted to CSR format.

- The epoch of the raw observation is given as the satellite transmission time. This is converted to satellite received time by adding the raw two-way time of flight measurement to the observation epoch.

• The raw two-way travel time is corrected with the supplied values for the ionosphere delay estimate, the satellite center of mass offset, the onboard PRARE antenna phase center correction, the ground station antenna rotation correction, and the external calibration correction. All of these corrections are added to the raw time-of-flight measurement, except for the ionosphere correction, which is subtracted.

• The corrected two-way travel time is converted to a one-way range measurement. This conversion is made by multiplying the two-way travel time by one half the speed of light (see Equation 2.1).

A.1 PRARE RANGE-RATE MEASUREMENTS

The PRARE range-rate measurements are converted from the GFZ format (Revision 5) to the CSR UTOPIA observation format. The raw observations are formatted as two-way Doppler cycle counts. During the conversion, all of the corrections are applied to the measurements, with the exception of the supplied troposphere delay. Before delivery, the raw cycle count measurements are corrected for the internal calibration of both the space segment and the ground station. The following explains how the raw range-rate measurements are converted to CSR format.

• The raw two-way Doppler cycle count is corrected with the supplied values for the ionosphere delay estimate, the satellite center of mass offset, the onboard PRARE antenna phase center correction, the ground station antenna

rotation correction, and the external calibration correction. All of these corrections are added to the raw measurement, including the ionosphere correction.

- The corrected two-way Doppler cycle count ($N + N_{corr}$ in the top line of Equation 2.9) is converted to a one-way range-rate measurement. This conversion is made by multiplying the two-way Doppler cycle count by half the speed of light and then dividing this by the product of the constant factor of frequency transposure (K), the transmitted frequency (f_{t_s}), and the Doppler count interval (Δt). The transmitted frequency is determined by adding the nominal frequency (8.489 GHz) to the amount of frequency offset.

Appendix B

The Niell troposphere mapping function

The mapping factors for both the dry and wet part of the troposphere delay (M_{dry} and M_{wet}) are defined in the Niell troposphere mapping function, unlike the Davis mapping function. These terms are used in Equation 2.12 to map the zenith troposphere delay to the proper elevation. The dry part of the mapping function is defined as:

$$M_{NMF_{dry}}(E) = m_{dry} + \Delta m_{dry}(E) \tag{B.1}$$

where m_{dry} is the mapping factor, similar to Equation 2.13 for the Davis function, and $\Delta m_{dry}(E)$ is a corrective term which accounts for the station height above mean sea level. The mapping factor is defined as:

$$m_{dry} = \frac{1 + \dfrac{a}{1 + \dfrac{b}{1 + c}}}{sin(E) + \dfrac{a}{sin(E) + \dfrac{b}{sin(E) + c}}} \tag{B.2}$$

The mapping coefficients (*a*, *b*, and *c*) are computed using:

$$a(\varphi_i, t) = a_{avg} - a_{amp}(\varphi_i) \cdot cos\left(2\pi \frac{t - T_o}{365.25}\right) \tag{B.3}$$

This equation is also applied to the *b* and *c* mapping coefficients. In Equation B.3, *t* is the time past January 0.0 (in days), T_o is the phase of 28.0 days, and φ is the tabular latitude. The coefficient averages and amplitudes (a_{avg} and a_{amp}) are given in Table B.1 for specific latitudes. Mapping coefficients are computed for the two latitudes closest to the station latitude. Finally, the mapping coefficients at the station latitude are linearly interpolated from these two coefficients.

The height correction term in Equation B.1 is defined as:

$$\Delta m_{dry}(E) = \left(\frac{1}{sin(E)} - f\left(E, a_{ht}, b_{ht}, c_{ht}\right) \right) \cdot H \qquad \text{(B.4)}$$

where f is the three-term continued fraction (Equation B.2), and the mapping coefficients given as:

$$a_{ht} = 2.53 \times 10^{-5}$$
$$b_{ht} = 5.49 \times 10^{-3}$$
$$c_{ht} = 1.14 \times 10^{-3}$$

The wet part of the mapping function ($M_{NMF_{wet}}$) is determined by using the same continued fraction as the dry mapping factor (Equation B.2). The wet mapping coefficients are given in Table B.1.

Table B.1: Niell Mapping Function coefficients

Coefficient	Latitude (degrees)				
	15	30	45	60	75
	Dry coefficients ($\times 10^{-3}$)				
a_{avg}	1.2769934	1.2683230	1.2465397	1.2196049	1.2045996
b_{avg}	2.9153695	2.9152299	2.9288445	2.9022565	2.9024912
c_{avg}	62.610505	62.837393	63.721774	63.824265	64.258455
			($\times 10^{-5}$)		
a_{amp}	0.0	1.2709626	2.6523662	3.4000452	4.1202191
b_{amp}	0.0	2.1414979	3.0160779	7.2562722	11.723375
c_{amp}	0.0	9.0128400	4.3497037	84.795348	170.37206
	Wet coefficients				
a ($\times 10^{-4}$)	5.8021897	5.6794847	5.8118019	5.9727542	6.1641693
b ($\times 10^{-3}$)	1.4275268	1.5138625	1.4572752	1.5007428	1.7599082
c ($\times 10^{-2}$)	4.3472961	4.6729510	4.3908931	4.4626982	5.4736038

Bibliography

Anderson, P.H., K. Asknes, H. Skonnord, Precise ERS-2 orbit determination using SLR, PRARE, and RA observations, *Journal of Geodesy*, Vol. 72, pp 421-429, 1998.

Anderson, P.H., K Aksnes, and H. Skonnord, ERS-2 Orbit Determination, EGS XXII General Assembly, Vienna, Austria, April 24, 1997.

Barlier, F., C. Berger, J. Falin, G. Kockarts, and G. Thuillier, Atmospheric Model based on Satellite drag data, *Ann. Geophysics*, Vol. 34, pp 9-24, 1978.

Bordi, J.J., J.C. Ries, B.D. Tapley, Precise orbit Determination and PRARE data analysis for ERS-2, *American Geophysical Union Fall Meeting*, December, 1997.

Boucher, C., Z. Altamimi, and P. Sillard, Results and Analysis of the ITRF96, *IERS Technical Note 24*, Observatoire de Paris, May 1998.

Boucher, C., Z. Altamimi, M. Feissel, and P. Sillard, Results and Analysis of the ITRF94, *IERS Technical Note 20*, Observatoire de Paris, March 1996.

Cartwright, D.E., and R.D. Ray, Oceanic Tides from Geosat Altimetry, *Journal of Geophysical Research*, Vol. 95, No. C3, pp 3069-3090, March 15, 1990.

Center for Space Research, CONAN the Program, *Users Manual*, Version 8704, pp 1-14, 1987.

Davis, G.W., J.C. Ries, and B.D. Tapley, The Accuracy Assessment of Precise Orbits Computed from Doppler Tracking Data, *The Journal of the Astronautical Sciences*, Vol. 45, No. 4, pp. 451-469, October-December 1997.

Davis, G.W., J.C. Ries, and B.D. Tapley, Preliminary Accuracy Assessment of the DORIS Tracking System on TOPEX/Poseidon, *AAS/AIAA Astrodynamics Specialist Conference AAS 93-574*, August 16-19, 1993.

Davis, J.L., T.A. Herring, I.I. Shapiro, A.E. Rogers, and G. Elgered, Geodesy by Radio Interferometry: Effects of Atmospheric Modeling Errors on

Estimated Baseline Length, *Radio Science*, Vol. 20, No. 6, pp 1593-1607, 1985.

DeMets, C., R.G. Gordon, D.F. Argus, and S. Stein, Effects of recent revisions to the geomagnetic reversal time scale on estimates of current plate motions, *Geophysical Research Letters*, Vol. 21, pp. 2191-2194, 1994.

Eanes, R.J., A Study of Temporal Variations in Earth's Gravitational Field using Lageos-1 Laser Range Observation, *Doctoral Dissertation*, The University of Texas at Austin, December 1995.

Eanes, R.J., B.E. Schutz, and B.D. Tapley, Earth and Ocean Tide effects on Lageos and Starlette, *Proc. of the 9th International Symposium on Earth Tides*, 1983.

Estefan, J.A., and O.J. Stovers, A Comparative Survey of Current and Proposed Tropospheric Refraction-Delay Models for DSN Radio Metric Data Calibration, *JPL Publication 94-24*, October 1994.

Enninghorst, K., F.H. Massmann, K.H. Neumayer, J.C. Raimondo, ERS-2 precise orbit determination with PRARE, *European Geophysical Society XXII General Assembly*, Vienna, Austria, April 21-25, 1997.

Flechtner, F., Calibration of the PRARE Ionospheric data, *GFZ Handouts of 2nd PRARE Splinter Meeting*, GFZ Potsdam, Germany, September 29, 1998.

Flechtner, F., and A. Teubel, PRARE ERS-2 Activities for Week 07, 1997, GeoforschungsZentrum Potsdam, Germany, February 1997.

Flechtner, F., S. Bedrich, A. Teubel, Modeling the Ionosphere with PRARE, *Proceedings from the third ERS Symposium*, Flolence, Italy, March 17-20, 1997.

Francis, R., G. Graf, P.G. Edwards, M. McCraig, C. McCarthy, A. Lefebvre, B. Pieper, P.Y. Pouvreau, R. Wall, F. Wechsler, J. Louet, W. Schumann, and R.Zobl, The ERS-2 Spacecraft and its Payload, *ESA Bulletin*, No. 83, pp 12-31, August 1995.

Francis, R., G. Graf, P.G. Edwards, M. McCraig, C. McCarthy, P. Dubock, A. Lefebvre, B. Pieper, P.Y. Pouvreau, R. Wall, F. Wechsler, J. Louet, and R.Zobl, The ERS-1 Spacecraft and its Payload, *ESA Bulletin*, No. 65, pp 27-48, February 1991.

Gentleman, W.M., Least Squares Computations by Givens Transformations without Square Roots, *Journal Inst. Mathematical Applications*, Vol. 12, 1973.

Groves, G.W., and R.W. Reynolds, An orthogonalized Convolution Method of Tide Prediction, *Journal of Geophysical Research*, 80, pp 4131-4138, 1975.

Hahne, A., A. Lefebvre, J. Callies, and B. Christensen, GOME - The Developement of a New Instrument, *ESA Bulletin*, No. 83, pp 41-46, August 1995.

Hasan, D.A., Analysis of Least Squares Orbit Determination Accumulation Algorithms, *M.S. Thesis*, The University of Texas at Austin, December 1988.

Kaula, W.M., *Theory of Satellite Geodesy, Applications of satellites to geodesy*, Blaisdell Publishing Company, 1966.

Kozel, B.J., Dual-Satelllite Altimeter Crossover measurements for Precise Orbit Determination, *Doctoral Dissertation*, August 1995.

Kruizinga, Gerhard L.H., Validations and Applications of Satellite Altimetry, *Doctoral Dissertation*., The University of Texas at Austin, 1997.

Lambeck, K., *The Earth's variable rotation: Geophysical causes and consequences*, Cambridge University Press, 1980.

Le Provost, C., M.L. Genco, F. Lyard, P. Vincent, and P. Canceil, Spectroscopy of the world ocean tides from a finite element hydrodynamic model, *Journal of Geophysical Research*, Vol. 99, No. C12, pp 24,777-24,797, 1994.

Massmann, F.-H., K.H. Neumayer, J.C. Raimando, K. Enninghorst, and H. Li, Quality of the D-PAF ERS orbits before and after inclusion of PRARE data, *Proc. 3rd ERS Scientific Symposium*, ESA SP-414, Florence, Italy, March 1997.

McKay, M. and S.J. Bosma, ERS-1: Four Years of Operational Experience, *ESA Bulletin*, No. 83, pp 47-52, August 1995.

Mendes, V.B., and R.B. Langley, A Comprehensive Analysis of Mapping Functions Used in Modeling Tropospheric Delay in Space Geodetic Data,

International Symposium on Kinematic Systems in Geodesy, Geomatics and Navigation, August 30 - September 2, 1994.

Minster, J.B., and T.H. Jordan, Present Day Plate Motions, *Journal of Geophysical Research*, Vol. 83, No. B11, pp 5331-5354, 1978.

Munk, W.H., and D.E. Cartwright, Tidal Spectroscopy and prediction, *Philos. Trans. R. Soc. London*, Ser. A.259, pp 533-589, 1966.

Nerem, R.S., F.J. Lerch, J.A. Marshall, E.C. Pavlis, B.H. Putney, B.D. Tapley, R.J. Eanes, J.C. Ries, B.E. Schutz, C.K. Shum, M.M. Watkins, S.M. Klosko, J.C. Chan, S.B. Luthcke, G.B. Patel, N.K. Pavlis, R.G. Williamson, R.H. Rapp, R. Biancale, and F. Nouel, Gravity model development for TOPEX/Poseidon: Joint Gravity Model 1 and 2, *Journal of Geophysical Research*, Vol. 99, No. C12, pp 24,421-24,447, 1994.

Niell, A.E., Global mapping functions for the atmosphere delay at radio wavelengths, *Journal of Geophysical Research*, Vol. 101, No. B2, pp 3227-3246, February 10, 1996.

Nortel Dasa Networks Systems, PRARE Ground Stations training course version 1, August 1995.

Parke, M.E., G. Born, R. Leden, C. McLaughlin, and C. Tierney, Altimeter sampling characteristics using a single satellite, *Journal of Geophysical Research*, Vol. 103, No. C5, pp 10,513-10,526, May, 1998.

Ries, J.C., and B.D. Tapley, Centimeter Level Orbit Determination for the Topex/Poseidon Altimeter Satellite, *AAS/AIAA Space Flight Mechanics Meeting AAS 99-142*, Breckenridge, Colorado, February 1999.

Ries, J.C., J.J. Bordi, C.K. Shum, and B.D. Tapley, Assessment of Precision Orbit Accuracy for ERS-1 and ERS-2, American Geophysical Union Spinrg Meeting, Batlimore, Maryland, May 1996.

Ries, J.C., C.K. Shum, and B.D. Tapley, Surface Force Modeling for Precision Orbit Determination, *Geophysical Monograph 73*, IUGG Vol. 13, pp 111-124, 1993.

Ries, J.C., Simulation of an Experiment to measure the Lense-Thirring precession using a second Lageos Satellite, *Doctoral Dissertation*, The University of Texas at Austin, 1989.

Rosborough, G.W., Satellite Orbit Perturbations due to the Geopotential, *Doctoral Dissertation*, The University of Texas at Austin, January, 1986.

Saastamoinen, J., Atmospheric Correction for the Troposphere and Stratosphere in Radio Ranging of Satellites, *The Use of Artificial Satellites for Geodesy*, Geophysics Monograph Series, Vol. 15, American Geophysical Union, Washington D.C., 1972.

Schafer, W., W. Schumann, PRARE-2 - Building on the Lessons Learnt from ERS-1, *ESA Bulletin*, No 83, pp 38-40, August, 1995.

Scharoo, R., and P.N.A.M. Visser, Precise orbit determination and gravity field improvement for the ERS satellites, *Journal of Geophysical Research*, Vol. 103, No. C4, pp 8113-8127, April 15, 1998.

Scharoo, R., and P.N.A.M. Visser, ERS Tandem Mission Orbits: Is 5 cm still a challenge?, *Publication of the 3rd ERS-symposium*, Florence, Italy, March 18-21, 1997.

Shum, C.K., B.H. Zhang, B.E. Schutz, and B.D. Tapley, Altimeter crossover methods for precsion orbit determination and the mapping of Geophysical Parameters, *The Journal of Astronautical Sciences*, Vol. 38, No. 3, pp 355-368, 1990.

Schutz, B.E., and B.D. Tapley, UTOPIA: University of Texas Orbit Processor, TR 80-1, Center for Space Research, The University of Texas at Austin, 1980.

Smith, J.C., Precision Orbit Determination for the Geosat Exact Repeat Mission, *Masters Thesis*, The University of Texas at Austin, August, 1988.

Standish, E.M., Orientation of the JPL ephemerides, DE200/LE200, to the dynamic equinox of J2000, *Astronomical Astrophysics*, Vol. 114, June 1982.

Stovers, O.J., and G.E. Lanyi, Evaluation of Current Tropospheric Mapping Functions by Deep Space Network Very Long Baseline Interferometry, *TDA Progress Report 42-119*, pp 1-11, November 15, 1994.

Stum, J., A comparison between TOPEX microwave radiometer, ERS-1 microwave radiometer, and European Centre for Medium-Range Weahter Forecasting derived wet tropospheric corrections, *Journal of Geophysical Research*, Vol. 99, No. C12, pp 24,927-24,939, December 15, 1994.

Tapley, B.D., C.K. Shum, J.C. Ries, S.R. Poole, P.A.M. Abusali, S.V. Bettadpur, R.J. Eanes, M.C. Kim, H.J. Rim, and B.E. Schutz, The TEG-3 Geopotential Model, *Gravity, Geoid and Marine Geodesy*, pp 453-460, J. Seagwa, H. Fujimoto, and S. Okubo (Ed.), Springer-Verlag, 1997.

Tapley, B.D., M.M. Watkins, J.C. Ries, G.W. Davis, R.J. Eanes, S.R. Poole, H.J. Rim, B.E. Schutz, C.K. Shum, R.S. Nerem, F.J. Lerch, J.A. Marshall, S.M. Klosko, N.K. Pavlis, and R.G. Williamson, The Joint Gravity Model 3, *Journal of Geophysical Research*, Vol. 101, No. B12, pp 28,029-28,049, December 10, 1996.

Tapley, B.D., J.C. Ries, G.W. Davis, R.J. Eanes, B.E. Schutz, C.K. Shum, M.M. Watkins, J.A. Marshall, R.S. Nerem, B.H.Putney, S.M. Klosko, S.B. Luthcke, D. Pavlis, R.G. Williamson, and N.P. Zelensky, Precision Orbit Determination for TOPEX/POSEIDON, *Journal of Geophysical Research*, Vol. 99, No. C12, pp 24,383-24,404, 1994.

Tapley, B.D., Satellite Orbit Determination: Fundamentals and Applications, *Class Notes*, The University of Texas at Austin, January 1994.

Tapley, B.D., B.E. Schutz, R.J. Eanes, J.C. Ries, and M.M. Watkins, Lageos Laser Ranging Contributions to Geodynamics, Geodesy, and Orbital Dynamics, *Contributions of Space Geodesy to Geodynamics: Earth Dynamics*, Geodynamics 24, 1993.

Tapley, B.D., Statistical Orbit Determination Theory, In B.D. Tapley and V. Szebehely (Eds.), *Recent Advances in Dynamical Astronomy*, D. Reidel Publishing, pp 396-425, 1973.

Vaughan, D.G., Tidal fexure at Ice Shelf Margins, *Journal of Geophysical Research*, Vol. 100, No. B4, pp 6213-6224, April 10, 1995.

Visser, P.N.A.M., R. Scharroo, R. Floberghagen, B. Ambrosius, Impact of PRARE on ERS-2 Orbit Determination, *Proceedings of 12th International Symposium on Space Flight Dynamics, ESOC, Darmstadt, 2-6 June 1997*, SP-403, pp 115-120, August 1997.

Watkins, M.M., Tracking Station Coordinates and their Temporal Evolution as Determined from Laser Ranging to th Lageos Satellite, *Doctoral Dissertation*, The University of Texas at Austin, May 1990.

Wilmes, H., Ch. Reigber, W. Schafer, Ph. Hartl, Precise Range And Range Rate Equipment, PRARE, On Board ERS-1 - Orbitography in Support of Radar Altimetry and Tool for Precise Relative Geodetic Positioning, *XIX*

I.U.G.G. General Assembly International Association of Geodesy, August 9-22, 1987.

Wells, D.E., Doppler Satellite Control, *Doctoral Dissertation*, University of New Brunswick, September, 1974.

Yuan, D.N., Large Linear System Solver (LLISS) Program Document, Center for Space Research, The University of Texas at Austin, 1991a.

Yuan, D.N., The Determination and Error Assessment of the Earth's Gravity Field Model, *Doctoral Dissertation*, The University of Texas at Austin, May 1991b.